Faculty of Engineering and Science
Aalborg University

Numerical and Experimental Study of Partially Concrete-Filled Circular Steel Sections

Master's Thesis

by

Søren Hansen

M.Sc. in Civil and Structural Engineering

June 2011

Preface

This project was initiated by Rambøll Oil & Gas and their wish to investigate the behaviour of partially concrete-filled steel tubes. In this context I would like to thank Ulf T. Tygesen and Michael Jepsen for the exchange of experience and knowledge on the subject.

Furthermore I want to thank Lars Damkilde and Ronnie R. Pedersen for their supervision and support during the semester.

This research is financially supported by grants from the SUC Fund Esbjerg # 2010-5745.

A thank to Elo Yde, BASF Construction Chemicals Denmark A/S, for the donation of Masterflow® 9500 used for grouting the high strength concrete test specimens. Also thanks to Trine Staanum for introducing how to mix and handle the Masterflow® 9500.

This report is based on the study of concrete filled steel tubes made by the author on the 3rd semester of the MSc. Program in the autumn of 2010. The previous report (in Danish) is found on the attached CD-ROM.

Abaqus 6-9.3 and 6-10.2 are used for the finite element analysis.

Data processing and calculations are performed in MATLAB.

Dimensions of tubes are written as outer diameter (OD)/thickness of the tube e.g. Ø139.7/4.0 mm has an OD=139.7 mm and a thickness of 4.0 mm. The dimensions of cylinders are written as OD/height of the cylinder e.g. a cylinder Ø139.7/200 mm has an OD of 139.7 mm and a height of 200 mm.

The attached CD-ROM contains:

- The report (PDF),
- Papers referred to in the report named by reference listed by reference number and title.
- Data-files from the experimental tests.

Esbjerg 17th of June 2011

S. Hansen

Summary

An experimental and numerical study of the partially concrete filled steel tube is conducted in order to investigate their mechanical behaviour.

Initially a hypothesis of the mechanical behaviour is developed. It is believed that the main parameters to dominate the mechanical behaviour of the PCFT besides the length of the grout core and the slenderness of the element (L/D) is the diameter- thickness ratio (D/t), the material strength and the bonding between steel and grout.
This thesis focus on the influence of the grout strength and the bonding by testing 6 steel tubes partially filled with high strength grout (f_c = 115 MPa) and 6 filled with low strength grout (f_c = 7.7 MPa) in 3-point bending. Half the test specimens are greased inside in order to remove the bonding between grout and steel.

An experimental test is carried out on an empty steel tube as a reference for the setup of a numeric model and the results of the experimental testing of the partially concrete filled steel tubes.

The Plastic-damage model in Abaqus is chosen as material model for the grout. The material model is described and a sensitivity study shows that the model is mesh-dependent when the viscoplastic regularization is activated.

Material testing on the grout determines the compressive and tensile strength. The modulus of elasticity and Poisson's ration is found for the high strength grout.

A simplified numerical model for the steel tube is fitted to the reference tube and the numeric model of the partially concrete filled steel tube is based on this simplified model.

The test results shows that the grout extend the linear elastic range of the load-deflection relation for the partially concrete filled steel tubes with 57-112 % depending on the grout strength and the contact relations.

The numeric results correspond to the experimental tests initially but underestimate the peak load due to the simplified model of the steel tube.

The failure mechanism is depending of the grout strength and the bonding between grout and steel. The cracks in the grout in the greased tubes are wider and the number of cracks reduced. In the low strength grout the crack width is so small that the invisible by the naked eye. The crushing is significant in the low strength grout contrary to the test specimens with high strength grout.

The failure in the steel differs due to the crushing in the grout. Outward buckling develops in the steel tubes partially filled with high strength grout and the inward deformation of the steel where the load is applied occurs.

Resumé

Delvist betonfyldte stålrør undersøges numerisk og eksperimentelt med henblik på at klarlægge deres mekaniske virkemåde.

Indledningsvis opstilles en hypotese på baggrund af kendskabet til det betonfyldte stålrør. Det forventes at de dominerende faktorer for den mekaniske virkemåde af det delvist betonfyldte stålrør foruden længden af betonkernen og elementets slankheds forhold (L/D) er forholdet mellem diameteren og godstykkelsen (D/t), materiale styrkerne og kontakt forholdet mellem stål og beton.
Denne rapport behandler betonstyrkens kontakt forholdenes indflydelse på 12 delvist beton-fyldte cirkulære stålprofiler belastet i 3-punkts bøjning. 6 prøveemnere udstøbes med højstyrke beton (f_c = 115 MPa) og 6 med lavstyrke beton (f_c = 7.7 MPa). Halvdelen af stålrørene for disse betonstyrker smøres indvendigt med fedt med henblik på at ophæve bindingen mellem materia-lerne.

Et tomt stålrør undersøges eksperimentelt med henblik på at danne reference grundlag dels for resultaterne af den eksperimentelle undersøgelse af de delvist betonfyldte stålrør og dels for kalibreringen af en numerisk model.

En materiale model for beton baseret på en plastic-damage model udvikles i Abaqus. Materiale modellen beskrives og et parameterstudie viser, at modellen er mesh-afhængig når viskoplasti-citeten, der er nødvendig for at give et realistisk billede af skaden i materialet, anvendes.

Eksperimentelt bestemmes betonens tryk- og trækstyrke for begge beton kvaliteter og elastici-tetsmodulet og Poisson's forhold for højstyrke betonen. Disse anvendes til kalibrering af materi-ale modellen for beton.

En forenklet numerisk model af de tomme stål rør tunes til resultaterne for referenceemnet og anvendes i den numeriske model for det delvist betonfyldte stålrør.

Test resultaterne viser at et revnet beton tværsnit ikke giver bidrager til bøjningsstivheden for det delvist beton fyldte stålrør. Betonen resulterer dog i en forøgelse af det lineært elastiske om-råde for det tomme stålrør med 57-112 % afhængigt af beton styrken og kontakt forholdende. Højere betonstyrke og bedre kontakt mellem stål og beton giver den største forlængelse.

De numeriske resultater harmonerer indledningsvist med de eksperimentelle men den numeri-ske model undervurder den ultimale bæreevne.

Brudmekanismerne afhænger også af beton styrken og kontaktforholdene. Revnevidden i be-tonkernen i stålrørene smurt med fedt er større og antallet af revner er reduceret. Revnerne i betonkernen i lavstyrke betonen er ikke synlige.

Stålrøret med højstyke beton udvikler ring buler ved store deformationer, hvor stålrøret med lav styrke beton buler indad hvor lasten påføres som følge af knusning i betonen.

Abbreviations and symbols

Abbreviations

CFT	Concrete Filled Steel-Tube
HSC	High strength Concrete
LSC	Low strength Concrete
NLGEOM	Non linear geometry
PCFT	Partially Concrete Filled Steel-Tube

Symbols

E_c	Modulus of elasticity for concrete or grout
E_s	Modulus of elasticity for steel
I_s	2nd moment of inertia for steel
I_c	2nd moment of inertia for concrete or grout
L	Length
Ø	Diameter or outer diameter
f_c	Compressive strength of concrete or grout
f_{sp}	Splitting tensile strength
f_t	Tensile strength of concrete or grout
t	Thickness
Ψ	Angle of dilatation
ν_c	Poisson's ration for concrete
ν_s	Poisson's ration for steel
μ	Viscosity parameter
μ_s	Static coefficient of friction
μ_k	Kinematic coefficient of friction
ω	Damage
ω_c	Tensile damage
ω_t	Compressive damage

Table of Contents

1. Introduction

1.1. Background

Since the first production platform was brought into service in the Danish sector of the North Sea in the early 1970's the oil and gas production has been increasing. Today more than 50 operative platforms are located in the North Sea. A large number of these platforms are designed in the 1980's and 1990's with a structural life time of 25 years and the platforms will have to be replaced or upgraded in the near future according to a report from the Danish Parliament's committee of energy policy [1.1]. The Petrol Safety Authority Norway concludes, that half of the platforms in the North Sea has already expired their designed life.

The utility rate of the oilfields has been increased, which means that the oil platforms must remain in service for a longer time or be substituted.

The design basis may have changes since the platforms were taken into service due to modifications of the structure, changes in the design loads and safety factors. Changes in the loading and the mass may lead to a changed structural dynamic response.

Because of the combination of degraded structures and the wish for longer service life, the industry and the structural design engineers develop new solutions to extend the life time. An obvious solution is to increase the stiffness of the jacket structure. An example of the jacket of an oil platform is shown in figure 1-1, where steel tubes are used as legs.

Figure 1-1: The production platform, Siri, and a rig (to the right) to drill the wells. The platform is founded on three legs (steel tubes) entering the caisson (the red box) on the seabed. The legs were partially grouted in 2003 as reinforcement of the legs due to change in the design loads.

Filling grout into a hollow section element can be a rather easy way to reinforce the structure, which can be relevant if requalification of the structural element is needed or extra modules on

the top site because of changed design loads. Grouting of the legs on an existing offshore platform has been used to reinforce the structure due to enlargement of the top site.

1.2. The Mechanical Behaviour of the Concrete-Filled Steel Tube

The starting point for understanding the mechanical behaviour of the partially concrete-filled steel tube (PCFT) is to look at the mechanical behaviour of the concrete-filled steel tube (CFT).

For visualization of mechanism in the CFT numerical tests have been conducted in the 3rd semester thesis. Details are found in the report file on the attached CD-ROM. The numerical used for the tests are described in chapter 4 and 5.

1.2.1. General

Steel and concrete are well known construction materials with different mechanical properties. The combination of the two materials in structural composite elements has been used increasingly in the last decades. The combination of steel and concrete in the structural composite element results in an increased strength and high ductility. Those properties are demanded in the design for structures in earthquake zones or where flexibility of the interior design leads to the need for larger spans and more slender columns [1.2].

Structural composite element will in the following include composite beam elements, which also governs composite beam-column. This report deals with the circular concrete-filled steel tubes, see figure 1-2
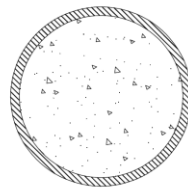

Figure 1-2: The section of a circular concrete-filled steel tube.

1.2.2. Special characteristic of CFT

In a mechanical perspective the behaviour of CFT depends on the interaction of the materials, which mainly is affected by three relations:

- The interaction between steel and grout.
- The difference in the Poisson's ratio of steel and concrete.
- Failure mechanisms in the materials.

Furthermore the load conditions play an important role in its mechanical behaviour, see figure 1-3, where the force vs. axial strain in the CFT is shown for a numerical test made on a axially loaded CFT with D/t = 50 and L/D = 6 (further details according to appendix E.1).
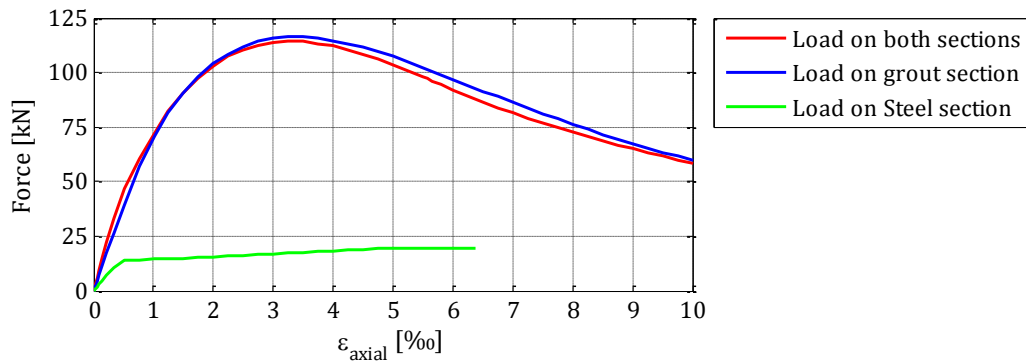
Figure 1-3: The influence of the loading. Force as function of axial strain. [1.17]

Interaction between steel and grout

In order to work as a structural composite element, the load has to be transferred across the contact surface. The load will be transferred as shear stresses, see figure 1-4.
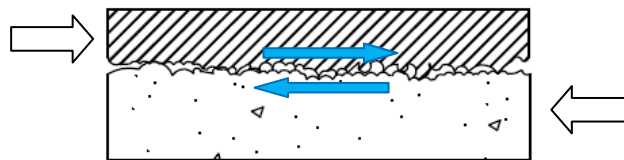

Figure 1-4: The shear transfer in the contact surface.

Four mechanisms are mainly involved in transferring the shear stresses at the contact surface:

- Adhesion.
- Micro interlocking.
- Friction.
- Binding.

Adhesion: Suction of the contact surfaces, where vacuum in the capillaries due to the chemical process in the concrete is generated. This mechanism is only active when the vacuum is maintained. At a slip of 0.01 mm in the contact surface the adhesion force are zero [1.3]. The adhesion is assumed to be neglected

Micro interlocking: surface irregularities in the steel tube, see figure 1-5, will assist to the shear transfer until local strain causes a crushing in the grout [1.3].
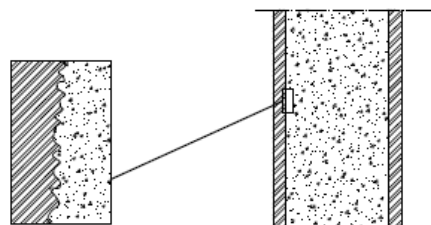

Figure 1-5: Micro interlocking due to surface irregularities.

Friction: When two surfaces are compressed, the friction expresses the resistance of their internal tangential slip. The radial tensile stresses in the contact surfaces due to the transverse contraction are of great importance of the size of the friction. The coefficient of friction is another

important factor when the friction is determined. In his study of axially loaded CFT, Johansson [1.3] has found a mean value of 0.6 regarding the normal forces, rugosity of the interior surface and the slip rate of the contact surfaces.

Binding or curvature mechanism: A geometric effect when the steel tube due to deformation "clamps" the grout core, see figure 1-6. The binding mechanism is the dominant shear transfer mechanism for CFT subjected to pure bending and inactive in pure axial compressive loading [1.4].
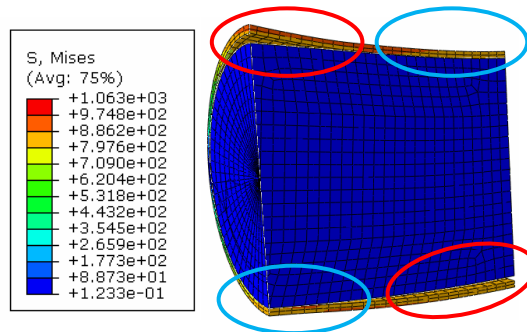

Figure 1-6: The binding mechanism for a CFT exposed to pure bending. Red circles in-dicate areas with slip between the contact surfaces and blue circles area where the contact surfaces are pressed together. The deformation is up-scaled by a factor100.

Difference in the Poisson's Ratio of Steel and Concrete

Poisson's ratio, ν, for concrete is 0.15-0.20, and 0.30 for steel. Depending on how the load is ap-plied to the CFT cross section, this difference will cause either a separation of the grout and steel or a compression in the contact surface (confinement). If an axial load is applied on the top of the concrete core alone, the radial deformation of the concrete will be confined by the steel tube, and a state of triaxial compressive stress will develop.

If the load is applied to the steel tube alone, the grout core and the steel tube will separate due to the transverse contraction in the steel.
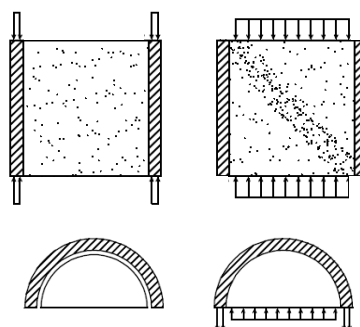
1.1.1.1. Axial loading

Figure 1-7: On top: Load applied to the steel section (left) and the grout section (right). Below: The consequences a) separation b) passive confinement of the grout core.

When the load is applied to the entire composite section a mix of the two before mentioned situations happens. In this case, the axial strains in the steel, ε_s^{al}, equals the axial strain in the grout, ε_c^a , see figure 1-8 [1.5].
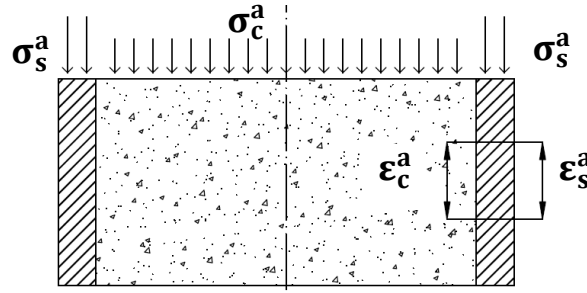
Figure 1-8: The axial strains in steel and grout are of equal size, when the load is applied to the entire CFT section.

Initially a gap is build-up due to the difference in Poisson ratios. Typically, the steel tube yields before the concrete core, depending on the material properties and thickness, see figure 1-9 .
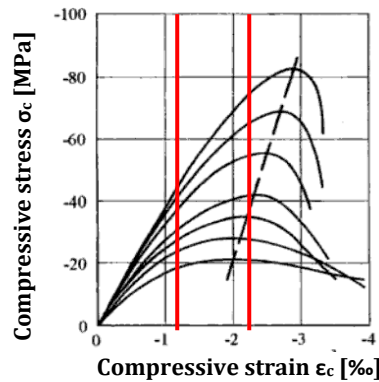

Figure 1-9: The compressive stress-strain relation. The evolution of the uniaxial compressive strength as a function of the ultimate strain, $f_{c0}(\varepsilon_u)$, is visualized with the dashed line. The red lines marks the yield strain for normal structural steel S235-S460 [1.6].

When the load is about 80 % of the capacity of the concrete core, the micro cracking in cement paste starts and the Poisson ratio increases, see figure 1-10.
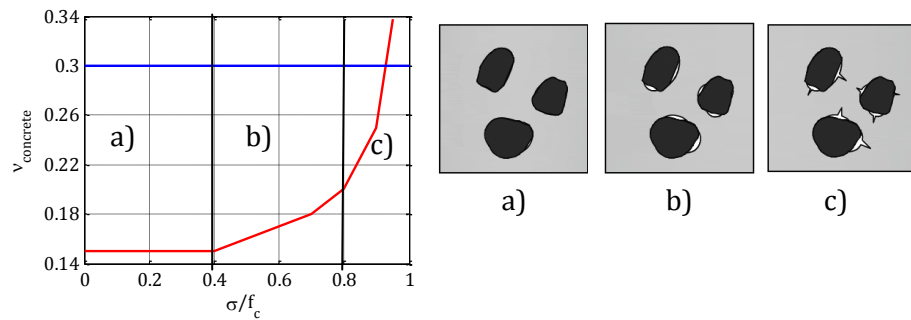

Figure 1-10: The development of Poisson's ratio for concrete vs. the normalized compressive stress and the micro-cracking: zone a) the initial pore volume, zone b) micro-cracking around the aggregates and zone c) micro-cracking in the cement paste. Source: figure 3.2-23 in [1.7]

The gap between the surfaces is then closed and the confinement of the concrete established.

The confinement of the concrete increases the compressive strength of the concrete significantly. Xiaobin and Cheng-Tzu [1.8] studied high strength concrete in a triaxial stress state by applying a transverse load. A confining pressure of 10 % of the uniaxial concrete strength increases the capacity with 50 %, see figure 1-11.
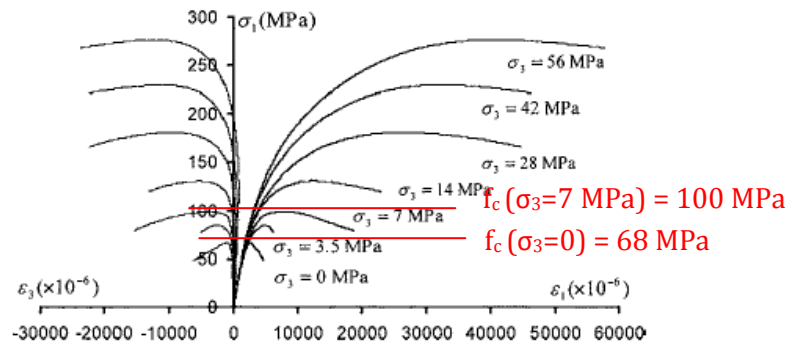
Figure 1-11: The axial stress vs. axial strain (positive part of the axis) and hoop strain (left part of the axis) for various confining stresses on a concrete cylinder. The results are from experimental tests. The concrete used has a uniaxial compressive strength, f_{c0}, = 68 MPa. [1.8]

Johansson [1.3] concluded that the passive confinement from the steel tube increases with the axial strain if contact between steel and concrete is re-established before yielding in the steel. After this point the confinement will be approximately constant until the strain hardening of the steel.

The radial pressure on the contact surface of the steel tube from the transverse contraction in the concrete generates hoop stresses in the steel tube, see figure 1-12.
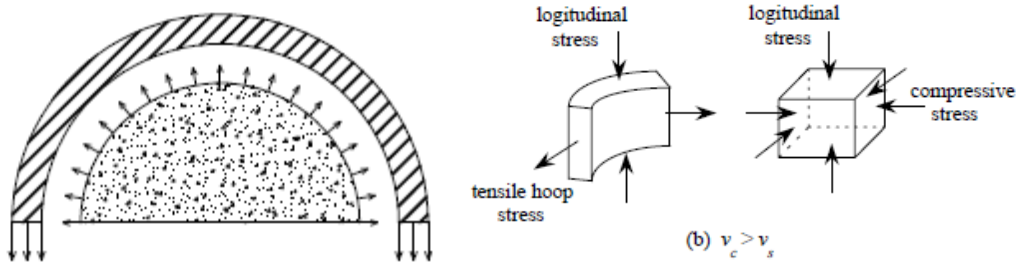

Figure 1-12: Hoop stresses in the steel tube caused by the transverse contraction for an axial load on the grout section (left). This situation occurs if no shear stress can be transferred in the contact surface (frictionless) or if Poisson's ratio for the grout exceeds the one for steel (right). The source for the figure to the right: [1.9].

The influence of the friction on the hoop stress and the axial stress in the steel tube for various coefficients of friction, when the load is applied to the grout section alone is seen in figure 1-13.
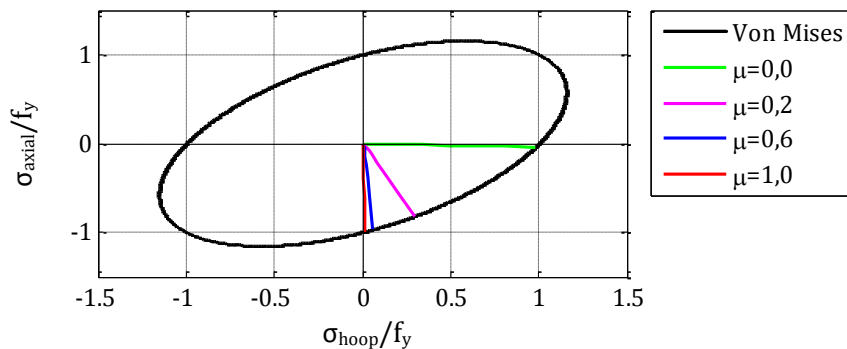

Figure 1-13: The distribution of normalized hoop - and axial stress for various coefficients of friction. Load applied to the grout section [1.17].

1.1.1.2. Bending

The mechanisms in the CFT subjected to pure bending are the same as for the axially loaded CFT. They will though differ in some way because the triaxial stress state in the grout cannot be reached. In the compressive zone of the CFT section, confinement will occur and increase the strength of the grout. In order to visualize this, the numerical model is modified according to appendix E.2.
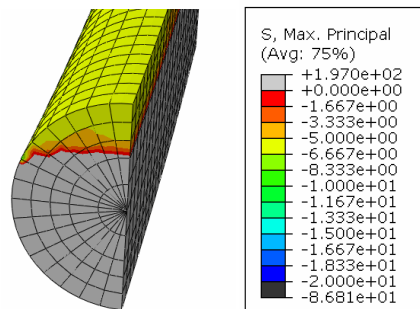

Figure 1-14: The maximal principal stress visualizes the zone of confinement in the grout core subjected to pure bending.

In the tensile zone the axial tensile stress leads to a radial compressive stress in the grout and tensile hoop stress in the steel tube, see figure 1-15. This opposite directed stress state is a disadvantage for the grout, but the steel tube benefits from the biaxial tensile stress state caused by the reversed confinement.
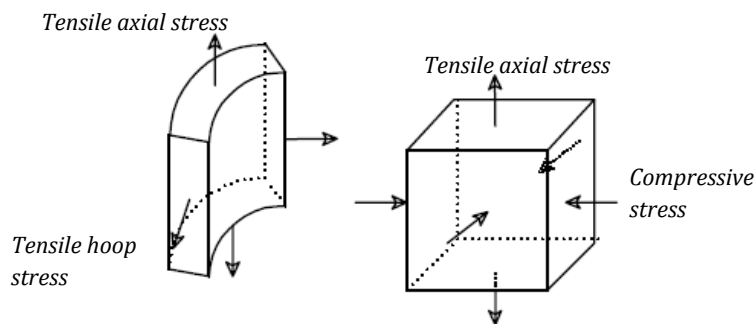

Figure 1-15: Stress distribution in the steel tube and the grout core in the CFT axially loaded in tension.

When cracks in the grout evolve, the efficient height of the grout section is reduced, see figure 1-16 and I_{grout} is reduced, and the flexural stiffness of the CFT is reduced. The principle progress of the flexural stiffness in the CFT section is shown in figure 1-17, where the strain – stress distribution in the CFT section and the upward movement of the neutral axis are visualized.
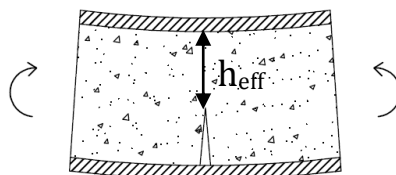

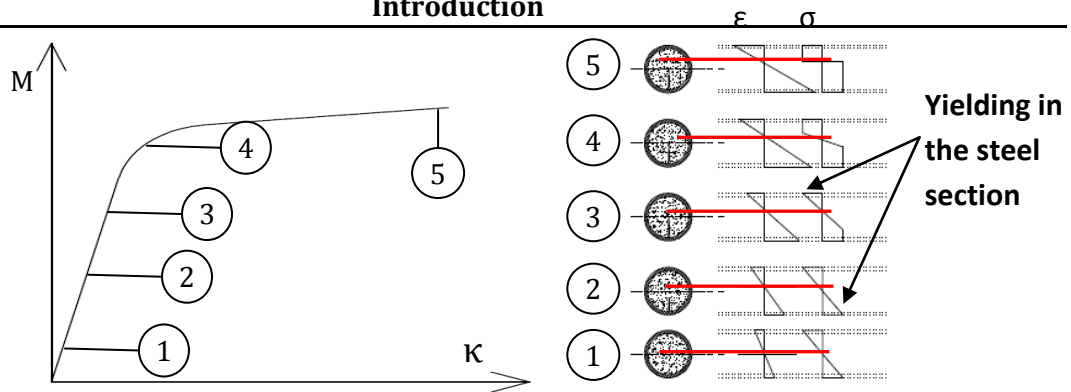**Figure 1-16: Cracking in the grout reduces the effective height of the grout section.**

Figure 1-17: The principle progress of the bending moment, M, as a function of the curvature, κ, for the load situation in figure 1-16. To the right the strain- stress distribution in the section is shown at the numbered spots. The neutral axis is marked with the red lines [1.17].

1) The tensile strain has reached the level, where the grout starts cracking and $\sigma < \sigma_y$.
2) The yield strain has been reached in the tensile zone of the steel tube. No yielding in the compressive zone because of the upward moment of the neutral line.
3) The yield strain is reached in the compressive zone of the steel tube. The yielding spreads through the steel section in the tensile zone.
4) The deformation of the CFT is accelerated and the yielding spreads in the entire steel tube.
5) Yielding in the entire cross section. The failure mode depends on the diameter- thickness ratio, to be discussed in section 1.1.1.4.

The stress distribution of a numerical model is according to figure 1-17. The positive and negative axial stresses in the grout core are also plotted in order to see the neutral line in the grout core. The principal stresses are plotted in both materials as vector plots, see figure 1-18.
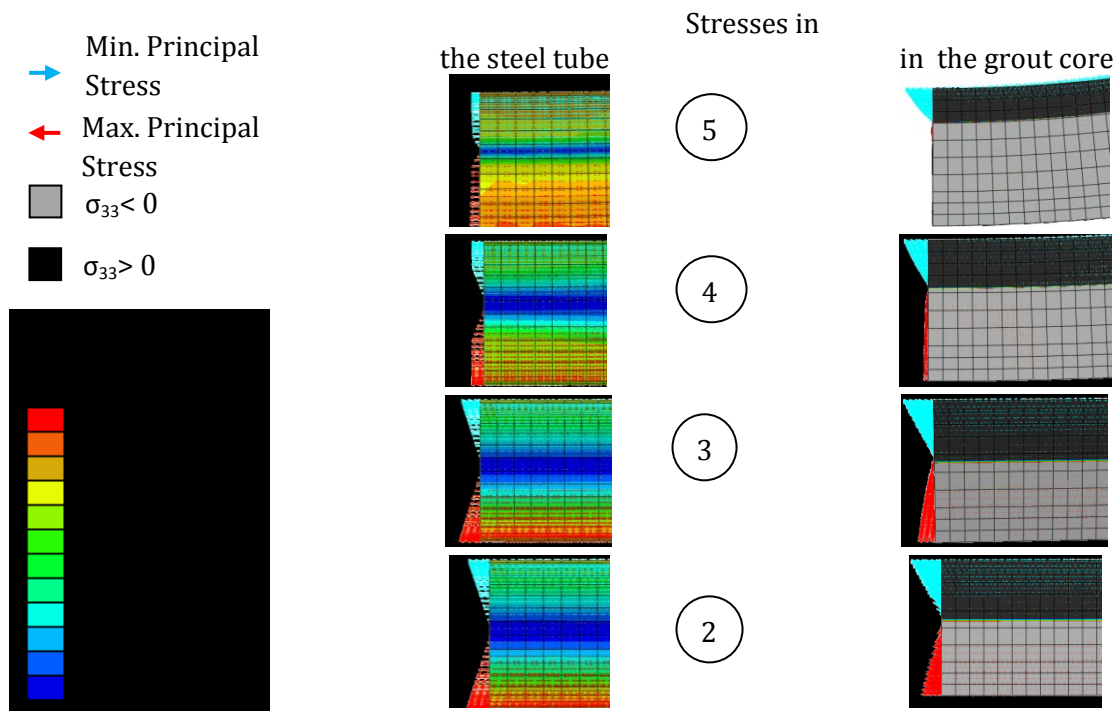

Figure 1-18: The Von Mises stresses in the steel tube (middle) and the axial stress, σ_{33}, in the grout core (right). The vectors= max and min principal stress. Legends are to the left. Numbers refers to figure 1-17.

The way to apply the load also influence the mechanical behaviour of the CFT subjected to pure bending. According to figure 1-19 the bending moment capacity and the ductility decreases significantly, when the load is applied to the steel section instead of to the entire CFT section.
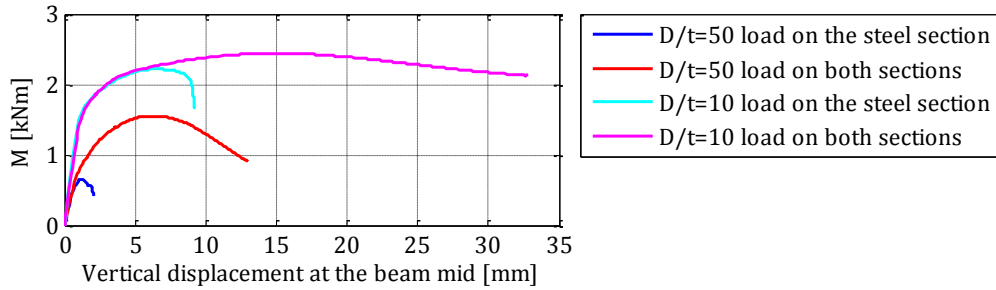

Figure 1-19: The bending moment as a function of the vertical deflection at the middle of the CFT.

This matter is due to the buckling in the steel tube, see figure 1-20, and becomes less significant, when D/t is decreased.
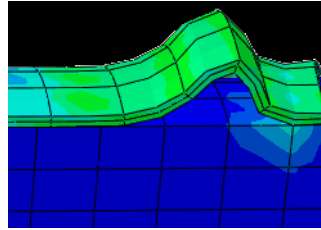
Figure 1-20: Zoom of the CFT subjected to pure bending. The steel buckles in the compressive zone.

1.1.1.3. Transverse loading

If the CFT is subjected to transverse loading, the mechanical behaviour depends on the shear span, see figure 1-21.

Figure 1-21: The shear span for a cantilever CFT beam subjected to a transverse loading.

The stresses are transferred through the CFT as shear stresses. The numerical model used to analyse the shear loading is described in appendix E.3. The hoop stresses is seen in figure 1-22, and the maximal and minimal principal stresses are shown in figure 1-23.

Figure 1-22: The hoop stress in the steel tube over the shear span.

The diagonal stress distribution is clear, tension in one diagonal and compression in the other, see figure 1-23.

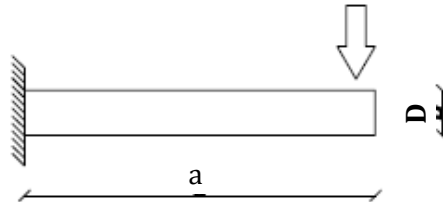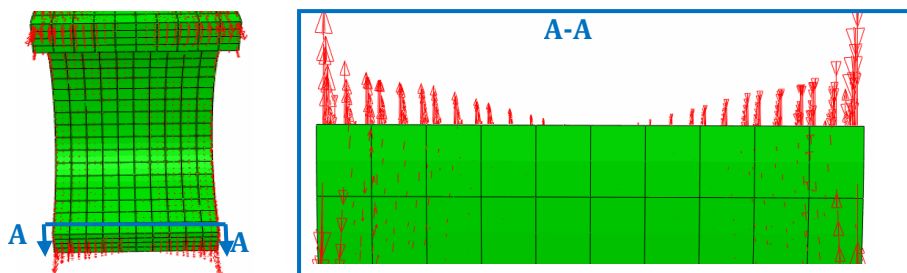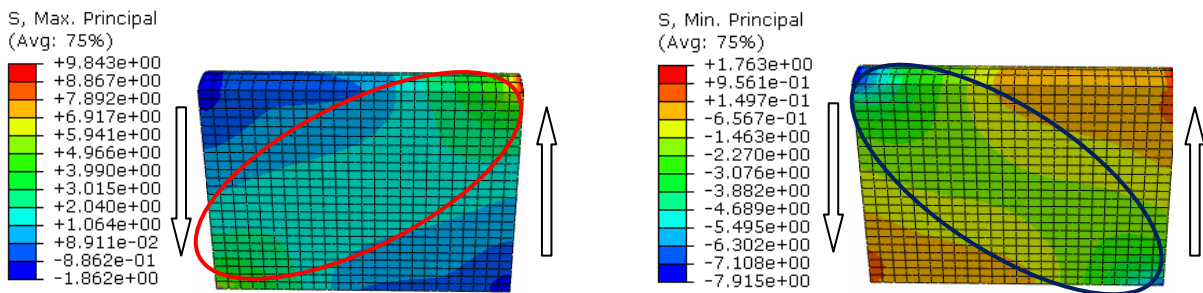**Figure 1-23: The maximal principal stresses (left) and the minimal principal stresses (right) in the grout core of a CFT with a shear span ratio of 1. The red marking shows the tensile stresses and the blue marking highlights the compressive stresses.**

1.1.1.4.   Failure Mechanisms

The failure mechanism in the CFTs occurs as buckling and/or a plastic hinge. The mechanism is in particular affected by:

- The way the load is applied.
- The diameter- thickness ratio, D/t.
- The material strength.

The failure in the CFT subjected to axial loading

If the load is applied to the steel section alone, the concrete core does not carry any stress, and the steel tube will fail in buckling. The grout prevents inward buckling of the steel tube. The first eigen buckling mode for the grouted steel tube is a ring buckling, see figure 1-24, where Johansson and Gylltoft tested circular CFTs in axial loading applied to the different cross sections.
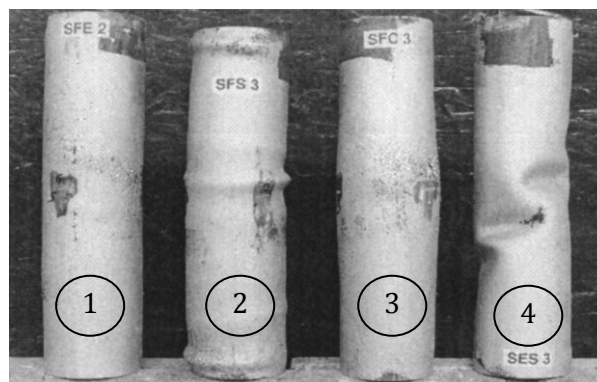
Figure 1-24: Failure mode in CFT's exposed to an axial concentric compressive load. The load has been applied to (1) the entire composite cross section, (2) the steel section and (3) the grout section. An empty reference tube (4) is seen to the right in the figure [1.10].

The failure mechanism in the grout section is either crushing or shear failure. Yielding in the steel tube starts before the grout fails. When the steel yields, the passive confinement is constant until the strain hardening takes place. The grout will be carrying the extra load by itself, and when the grout fails, the steel will buckle, see figure 1-25.
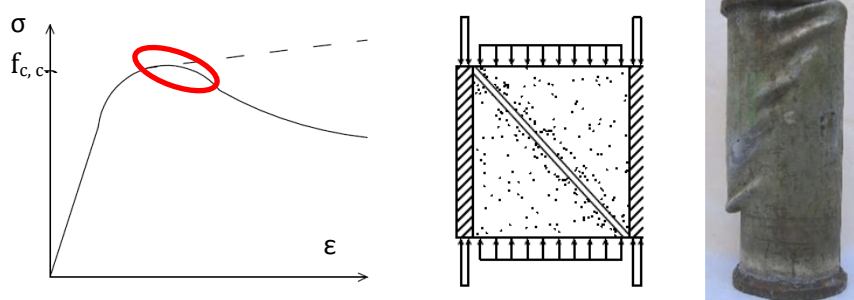
Figure 1-25: The shear failure in the grout core. When the confined compressive strength $f_{c\,c}$, has been reached– the red area on the stress-strain relation (left) and the steel is yielding, the shear failure evolves as visualized in the principle sketch (middle). The shear failure is obvious in the CFT (right).

The failure of the CFT subjected to pure bending

Cracking starts in the grout core followed by yielding in the tensile zone of the steel tube. The following step depends on the compressive strength of the grout, f_c, and the D/t. When f_c is high, the steel starts yielding before the grout crushes. If f_c is low crushing in the grout may occur before yielding, and the steel tube is not constrained in an inward buckling.

If D/t is low, the yielding spreads to the entire steel section before buckling starts. When the steel tube buckles in the compressive zone, the confining pressure is neutralized, and the grout starts crushing. If the crack width in the grout is big, an inward buckling of the steel can occur.

The failure of the CFT subjected to shear force

Lin Hai et al. [1.11] made an experimental and numerical study on 19 circular CFTs and concluded that for a shear span-diameter ratio, a/D, have influence on the failure:

- a/D<0.2 the failure is dominated by shear failure
- 0.2<a/D<4 the failure mode is a mix of shear failure and
- > 4 the failure is dominated by the bending moment due to the

The failure in the grout of a CFT subjected to a transverse force with a shear span of 1 is shown in figure 1-26 and the inclined cracks are due to the tensile stress diagonal according to figure 1-23 are visible.

Figure 1-26: The shear failure of a CFT Ø88/4 with high strength concrete (masterflow® 9500; f_c=115 MPa). The test is made by the author in autum/2010. The steel tube was cut open (left) and the inclined cracks of the shear failure in the grout was made visible (right).

1.3. Problem Statement

In the process of updating the stiffness or strength of the structure, reanalyses may result in a need for reinforcing specific parts of the structure. Grouting is due to the weight and the curing most suitable for reinforcing vertical structural elements such as legs of an offshore structure. The highest stresses are not necessarily observed in the lowest part of a leg, see figure 1-27. The height of the grout core will be dictated by the utility rate of the steel section, and the grouting leads to a partially concrete-filled steel tube (PCFT).
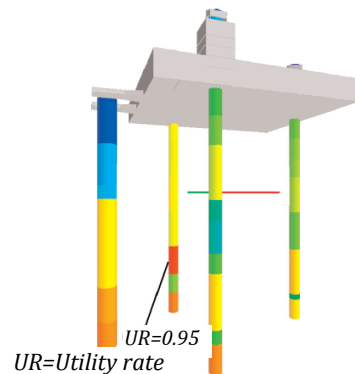

UR=0.95
UR=Utility rate

Figure 1-27: Model of a platform. The colours indicate the utility rate of the elements, red is high and blue is low [1.12].

If e.g. an existing leg is grouted, the steel tube has been surrounded by seawater for several years and the inside of the steel tube will be fouled with marine growths such as algae and barnacles. Furthermore the steel surface will be corroded. In order to establish full contact between steel and grout, the steel tube has to be remediated before grouting.

When grouting an existing structure, the structure is already exposed to the environmental loads. During the curing of the grout, the dynamic loading of the structure will affect the bonding between the steel and the grout. In the upper parts of the grout core, the small displacements reduce the contact between steel and grout, and the stress transfer between the materials will be reduced.

In case of reinforcement due to extra modules on the top site, the grouting will most likely be executed before the extra modules are sited on the structure. The load of the extra modules is transferred through the steel tube and lead to separation of steel and grout.

When the PCFT is implemented as reinforcement of a structure, the initial loading is applied to the steel tube. The stresses will only be transferred to the grout when contact is established caused by the bending moment due to vertical loading and imperfections in the structure. In figure 1-28 a simple model of a partially grouted steel tube shows this. The PCFT is fixed in one end and loaded in the other. Initially the grout is filled in the tube. Then the extra load (axial) is applied to the steel section and due to the Poisson ratio of the materials the materials separate. When transverse load is applied contact will be re-established in areas exposed to the tensile stresses and load will be transferred to the grout.
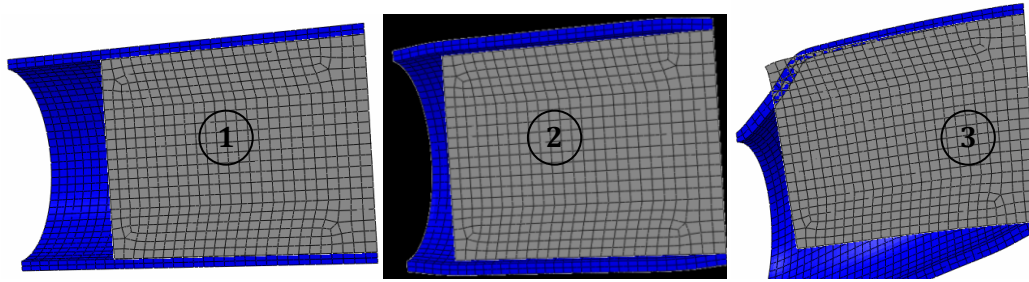
Figure 1-28: A composite element fixed in the end with the grout and the load applied to the steel tube in the other end. The element is subjected to (1) no load, (2) axial load on the steel section and (3) the axial load from (2)combined with a transverse load on the steel section. Contact is re-established due to transverse the loading. The deformations are scaled with a factor 25 in order to visualize the effect. The contact surface is modelled as Coulomb friction.

The bending moment results in cracks in the grout and the dynamic transverse load affects the structure 360 degrees so the entire grout section can be considered as cracked.

Rambøll Oil&Gas has conducted a numerical analysis of a cyclic transverse loaded grouted leg of a platform [1.16]. The geometry of the leg is shown in figure 1-29.
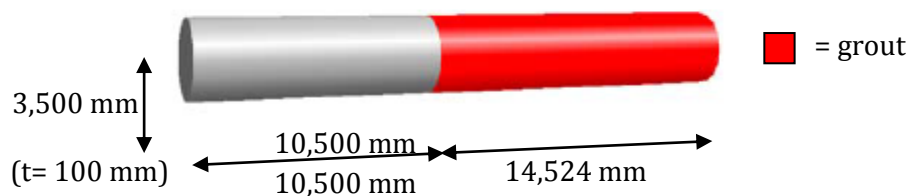

3,500 mm

(t= 100 mm)

10,500 mm

10,500 mm

14,524 mm

= grout

Figure 1-29: The geometry of the grouted leg in the Rambøll analysis. [1.16]

The conclusion was that no significant increase of the bending stiffness due to the grout was found.

According to [1.1] the flexural stiffness for a composite beam can be determined for the un-cracked grout section as in eq. 1-1:

$$EI_{CFT} = E_{steel}I_{steel} + E_{grout}I_{grout}$$

Eq. 1-1

Where
E= modulus of elasticity
I = 2nd moment of initia – I_{grout} is for the un-cracked grout section.

When the grout is cracked through the entire grout section, the contribution of the grout will be insignificant, and the bending stiffness of the CFT will equal the empty steel tube. The normal stresses will not be transferred to the grout core

High strength grout products from Densit® have been used to reinforce the legs at several off-shore structures according to [1.12] and [1.13]. High strength mortars are often used in other offshore relations e.g. the grout connection of transitions piece and mono pile of offshore wind turbines, so it is likely that a similar product will be used to grout the legs of the platforms.

The shear span for a grouted leg of a platform is higher than 4, which means that the failure caused by the transverse load is dominated by the bending failure. In figure 1-30 the directions

of the cracks in the grout of a PCFT with a shear span of 3.7 exposed to three point bending are perpendicular to the beam axis like in the pure bending.

Figure 1-30: Failure mechanism in the steel section (left) anf the grout section (right) of a PCFT test specimen.

In order to study the behaviour of the PCFT, a hypothesis is developed.

1.4. Hypothesis for the PCFT

Due to the knowledge of the mechanical behaviour of the CFT a hypothesis of the mechanical behaviour of the PCFT is developed.

The loading of a PCFT will always be applied to the steel section resulting in:

- The axially load case: no axial stress is transferred to the concrete core. The grout only constrains the inward buckling of the steel tube.
- The flexural load case: the axial stresses are transferred as shear stresses, in zones of contact primarily due to the binding mechanism and friction.
- The shear load case: the shear stresses are transferred as shear stresses to the grout core. If the shear span is higher than 4, the normal stresses due to the bending, will be dominating.

The main parameters to be domination the mechanical behaviour of the PCFT is assessed to be:

- The diameter- thickness ratio (D/t)
- The material strength
- Contact properties

The D/t is important to the failure mode and the load carrying capacity. D/t determine the class of cross section, and thereby the ability to develop the plastic resistance before buckling or forming a plastic hinge. This is particularly important in the zones, where the passive confinement of the grout happens. If the steel buckles the confining pressure disappears and the compressive strength of the grout decreases to the uniaxial compressive strength. For Class 3 or 4 cross sections the failure due to buckling in the empty part of the PCFT is assumed to be likely. This depends of course on the grout-ratio (length of grout core /length of PCFT), L_{grout}/L.

Like for the CFTs, the material strength will affect the mechanical behaviour. The load capacity and the failure mechanism in the PCFT are depending on the yield strength of the steel and the compressive and tensile strength of the grout. The yield strength primarily affects the load carrying capacity

The tensile strength of the concrete is assumed to influence the initial flexural stiffness of the PCFT. When the grout starts cracking the flexural stiffness of the PCFT will decrease and in a cyclic load case the entire grout section is assessed to be cracked, why the flexural stiffness is expected to be closed to the stiffness of the empty tube.

The compressive strength influences the buckling mode. A low strength grout will crush due to the radial compressive stress and the buckling in the steel tube will be inward. The crushing in the high strength grout will be small, and the buckling in the steel tube will be outward. The energy for this buckling state is higher than for the inward buckling, and the load-carrying capacity is expected to increase. The low strength grout will delay the buckling and therefore an increase in load-carrying capacity compared to the empty steel tube is expected.

The contact relation is assumed to influence the failure in the grout. A good bond between steel and grout is expected to decrease the crack width in the grout and increase the number of cracks. It takes more energy to initiate a new crack than to prolong an existing and therefore the crack pattern is expected to influence the load carrying capacity. A good bond will increase the load carrying capacity of the PCFT, but not as much as the material strength.

Also the length-diameter ratio (L/D) will influence the mechanical behaviour. The L/D due to the slenderness of the PCFT as a column - an increasing slenderness will decrease the load carrying capacity. The L/D ratio is directly linked to the shear span for a transverse loading in the top of the PCFT.

1.5. Scope of the Report

The purpose of this thesis is to study the mechanical behaviour of the partially concrete-filled steel tube numerically and experientially. The focus will be on the influence of the concrete strength and the contact properties.

The experimental study is based on the situation of a grouted leg of an offshore platform and the study will cover the transverse loaded PCFT. The geometry of the leg in figure 1-29 will be down scaled so the D/t and L_{grout}/L ratios are equal. The leg is fixed in the grouted end and free in the other.

The experimental setup will be a 3-point bending of PCFT's with a high/low strength grout. Half of the test specimens will be coated inside in order to neutralize the contact between steel and grout.

A numerical model of the PCFT is developed in Abaqus.

References Chapter 1

1.1   Afsnit 4: Sikkerhed og sundhed. Det Energipolitiske Udvalg 2009-2010 EPU alm. del
       http://www.ft.dk/dokumenter/tingdok.aspx?/samling/20091/almdel/epu/bilag/303/862176/index.htm

1.2   Shanmugam, N.E.; Lakshmi, B. (2001), "State of the art report on steel–concrete composite columns",   Journal of Constructional Steel Research nr. 57

1.3   Johansson, M. (2000) "Structural Behaviour of Circular Steel-Concrete Composite Columns", Chalmers University of Technology.

1.4   Mittelstäadt, J. (2008) "Numerische Untersuchungen zur Verbundwirkung bei betongefüllten Hohlprofilstützen", Technische Universität Hamburg-Harburg

1.5   Choi, K. K.; Xiao, Y. (2010) "Analytical Studies of Concrete-Filled Circular Steel Tubes under Axial Compression", Journal of Structural Engineering © ASCE, 5/2010 565-573

1.6   "Structural Concrete – textbook on Behaviour, Design and Performance, Vol.1" Fédération internationale du béton (FIB) (1999)

1.7   "Betonbogen" 2nd edition. Aalborg Portland - Cementfabrikkernes teknisk oplysningskontor (1985). ISBN 87-980916-0-8

1.8   Xiaobin, L.; Cheng-Tzu, T. H. (2007), "Stress-Strain Relations of High-Strength Concrete under Triaxial Compression", Journal of Materials in Civil Engineering 3/2007 261-268.

1.9   Lu, Z.H.; Zhao, Y.G. (2008) "Mechanical Behaviour and Ultimate Strength of Circular CFT Columns Subjected to Axial Compression Loads", The 14th World Conference on Earthquake Engineering, October 12-17, 2008, Beijing, China

1.10   Eurocode 4:" Design of composite steel and concrete structures – Part 1-1: General rules and rules for buildings" DS/EN 1994-1-1:2004, 2nd edition 2007

1.11   Lin-Hai Han et al. (2008), "Behaviour of CFT Members Subjected to Shear and Constant Axial Compression", Thin-Walled Structures 46   3/2008

1.12   Johansson, M.; Gylltoft, K. (2002), "Mechanical Behaviour of Circular Steel–Concrete Composite Stub Columns", Journal Of Structural Engineering / August 2002 / 1073-1081

1.13   Lam, D. ; Giakoumelis, G. (2004), "Axial Capacity of Circular Concrete Filled Tube Column", Journal of Constructional Steel Research 60 2004 1049–1068

1.14   http://densit.net.dynamicweb.dk/Files/Filer/pdf_files/Documentation/doc-siri-uk.pdf

1.15   http://densit.net.dynamicweb.dk/Files/Filer/pdf_files/platform/Documentation/South_Furious_2006.pdf

1.16   "Grouted legs" numerical study (LS-DYNA), Rambøll Oil&Gas (*not attached)*

1.17   Hansen, S. (2010) "Eksperimentel og numerisk analyse af delvist betonfyldte cirkulære stålprofiler". 3rd semester report.

2. Material Testing

2.1. General

The material tests are made in order to determine some of the important physical material properties. These parameters are used to calibrate the numerical model to be discussed in chapter 4. This is important because the numerical and the experimental results are to be compared.

The most important physical properties are the material strength, Poisson's ratio and the modulus of elasticity of the grout and the yield- and ultimate strength of the steel. Furthermore the contact properties of steel on grout are tested in order to find a way to eliminate the bond.

The material properties to be determined experimentally:

Grout (Details of the properties of the grout material can be found in appendix A):
- Compressive strength (f_c)
- Tensile strength (f_t)
- Modulus of elasticity (E_c)
- Poisson's ratio (ν_c)

Steel (Details of the steel can be found in appendix C):
- Yield strength (f_y) and yield strain (ε_y)
- Ultimate strength (f_y) and strain (ε_y)
- Modulus of elasticity (E_s)

Contact properties (Details can be found in appendix B):
- The force-displacement relation

2.2. Grout Tests

Two types of grout are used in the experimental tests in order to examine the influence from the concrete strength. A high strength mortar (HSC) and a low strength concrete (LSC) are used in the main test program.

The HSC from Masterflow (Masterflow® 9500) is characterized by a maximum aggregate, d_{max}, of 4 mm. The water-cement ratio, W/C, is 0.07. The characteristic value (10%-fractile) for the compressive strength for cylinders Ø150/300 mm is 116 MPa [2.1].

The LSC is a standard Portland concrete. In order to compare the strength of the grout materials, d_{max} is chosen to 4 mm. The w/c is 1.10 which according to Bolomey's adjusted formula leads to an expected compressive strength about [2.2].

Eq. 2-1

$$f_c = K\left(\frac{1}{w/c} - 0.5\right)(1 - 0.04(a - a_0)) = 8 \text{ MPa}$$

where

K=27 for basic cement
w/c is the water-cement ratio (in this case 1.10)
a is the air content in the concrete (in this case 8 %), and

a_0 is the natural air content (1.5 %)

2.2.1. Compressive Strength

The Amsler compression testing machine used in the experiments has a compressive capacity of 1000 kN. Two types of test specimens are used, cylinders Ø100/200 and Ø60/120, see figure 2-1. The smaller specimens are for the HSC because of the limited compression capacity of the testing machine.

Figure 2-1: The sizes of the cylinders for testing the compressive strength (right) and the test setup (left)

In total 13 cylinders of HSC and 5 cylinders of LSC have been tested according to DS/EN 12390-3, see appendix A3 for details. The mean compressive strengths, $f_{c, mean}$, found are shown in table 2-1. They are close to the expected values and used to calibrate the numerical material models.

Grout	$f_{c, mean}$ [MPa]	SD [MPa]	$f_{c, Expected}$ [MPa]	deviation $f_{c, mean}$ - $f_{c, Expected}$
HSC	115.4	7.2	116 MPa	0.5 %
LSC	7.7	0.7	8,0 MPa	3,8 %

Table 2-1: Mean strength of the grouts and the expected values according to [2.1] and [2.2]. SD = standard deviation.

2.2.2. Tensile Strength

The tensile strength of concrete, f_t, is determined indirectly as splitting tensile strength by using the Brazilian test setup, see figure 2-2.
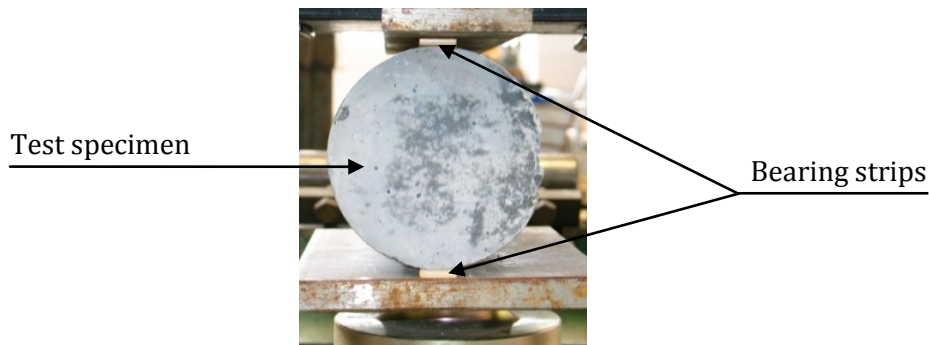

Figure 2-2: The setup for the Brazilian test.

According to [2.2] the splitting tensile strength, f_{sp}, is determined by the ultimate load, P_u, the length, L and the diameter, D, as in eq. 2-2

$$f_{sp} = 2 \cdot \frac{P_u}{\pi \cdot L \cdot D}$$

Eq. 2-2

The results of the split tests appear from table 2-2.

Test specimen		h [mm]	D [mm]	$P_{ultimate}$ [kN	f_{sp} [MPa]	
	CYL 1	200.0	100.1	29.2	0.9	
	CYL 2	199.5	100.3	26.2	0.8	
	CYL 3	197.8	100.2	29.1	0.9	
LSC	CYL 4	197.4	100.1	25.2	0.8	
	CYL 5	199.9	100.2	27.9	0.9	
	CYL 6	200.0	99.7	30.1	1.0	
	Mean value				0.9	
	Standard deviation				0.1	(11 %)
	cyl 1	121.5	59.98	82.78	7.2	
	cyl 2	121.3	60.03	113.9	10.0	
HSC	cyl 3	121.4	60.01	83.0	7.3	
	cyl 4	121.6	60.05	110.6	9.7	
	Mean value				8.5	
	Standard deviation				1.5	(18 %)

Table 2-2: Test results for the Brazilian tests. Uppercase =cylinders Ø100 mm, lowercase =cylinders Ø 60 mm.

Aalborg University has carried out tests to determine the mechanical properties of Masterflow® 9500 for BASF Construction Chemicals Denmark A/S [2.3]. Here the splitting tensile strength was determined as 8.5 MPa. This confirms the mean value of f_{sp} for the HSC and f_{sp} = 8.5 MPa will despite a standard deviation of 18 % of the mean value be accepted.

The correlation of f_{sp} and f_t is according to Eurocode 2 [2.4] based on the proposal of CEB-90 [2.5] (a model code to compute/describe concrete)

$$f_t = 0.9 \cdot f_{sp}$$

Eq. 2-3

Rocco et al. [2.6] have studied the influence of the compressive strength and maximum size of the aggregates in the concrete on the f_t/f_{sp}, see figure 2-3.
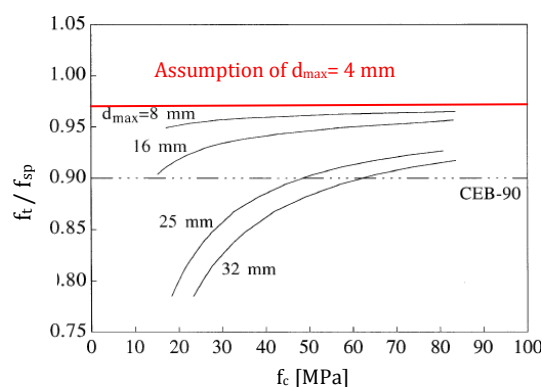

Figure 2-3: Ratio of the tensile strength to the splitting tensile strength compared to the proposal of [2.5] (the line CEB-90) for different maximum aggregate size, d_{max} [2.6]. The red line is an assumption for d_{max}=4 mm.

An increase in the size of the aggregates reduces the f_t/f_{sp}-ratio in general, and the tendency is more significant for low compressive strength.

Smaller aggregates (d < 8 mm) show a minor sensitivity on the f_t/f_{sp}-ratio due to the compressive strength. For d_{max}=4 mm the f_t/f_{sp}-0.97 is assumed. The dependency on the compressive strength is ignored, so the value can be used for both grout materials.

The dimensions of the cylinder and the bearing strips also influence the f_t/f_{sp}-ratio according to figure 2-4.
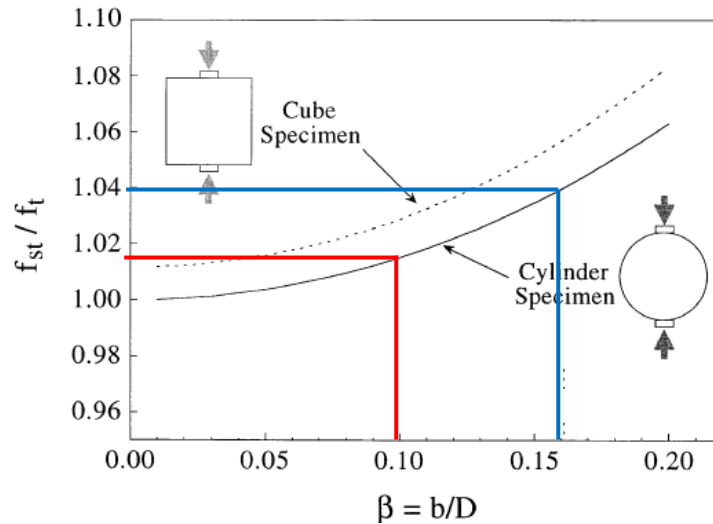

Figure 2-4: Variation of the splitting tensile strength with the relative width of the load bearing strips, b. [Rocco] The red line is β for the Ø100 cylinders (LSC), the blue line for Ø60 cylinders (HSC).

The f_{sp}/f_t ratios are 1.015 and 1.041 respectively. This leads to

$$f_t = \begin{cases} \dfrac{0.97}{1.015} \cdot f_{sp\,(\text{Ø100 mm})} \\ \dfrac{0.97}{1.041} \cdot f_{sp\,(\text{Ø60 mm})} \end{cases} = \begin{cases} 0.96 \cdot 0{,}9 \text{ MPa} = 0.9 \text{ MPa (LSC)} \\ 0.93 \cdot 8{,}5 \text{ MPa} = 7.9 \text{ MPa (HSC)} \end{cases}$$

Eq. 2-4

2.2.3. Modulus of Elasticity and Poisson's ratio

The modulus of elasticity, E_c, and Poisson's ratio, ν_c, for the grout are important numerical input parameters and must be determined.

For the HSC tests have been carried out according to appendix A.5 on an axially loaded cylinder with strain gauges perpendicular to each other with an intern angle of 60 degrees, see figure 2-5.
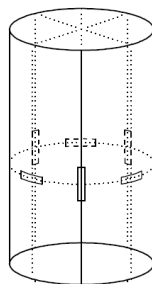

Figure 2-5: The setup for determination of E_c, and ν_c.

	E_c [GPa]	ν_c [-]
Mean value	51.7	0.17
Standard variation	0.14	1.7×10^{-3}

Table 2-3: mean values and standard deviations of modulus of elasticity and Poisson ratio for HSC.

The modulus of elasticity and Poisson's ratio were examined in [2.3] to 50.9 GPa and 0.199, respectively. The standard deviation in the present report is determined to 0.14 GPa and validates the test result, and Ec = 51.7 GPa will be used as input in the numerical material model.

The standard deviation is 1 % of the mean value and the mean value will in spite of a deviation of 15 % from the value in [2.3] be used as input parameter.

The standard deviations are very small, and the values are in the expected area and therefore considered to be valid.

The modulus of elasticity for the low strength concrete is according to [2.4] estimated as

$$E = 22 \cdot \left(\frac{f_{cm}}{10}\right)^{0.3} = 22 \cdot \left(\frac{0.9}{10}\right)^{0.3} = 10{,}7 \text{ GPa}$$ **Eq. 2-5**

The Poisson's ratio is set to 0.17.

2.2.4. Hardening temperature
Concrete is tested after 28th day of curing at 20 °C at a humidity of 100%. In order to speed up the hardening process the temperature can be increased. If the temperature is increased to 65 °C, the curing can be reduced with a factor 6.2, see figure 2-6.
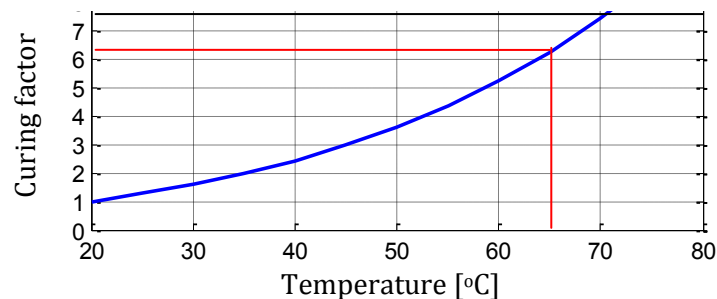

Figure 2-6: Curing factor for T >20 °C [2.2].

This process has not been studied for Masterflow® 9500. A simple test of three test sets of each 5 grout cylinders cured with different temperatures was made in order to detect differences in the compressive strength (f_c). The test sets were hardened at 20 °C, 42 °C and 65 °C respectively and the corresponding compressive strengths are shown in table 2-4.

Hardening temperature for the test set	$f_{c\text{-mean}}$ [MPa]	SD [MPa]
20 °C	115.8	7.2
42 °C	115.9	7.8
65 °C	114.4	8.6

Table 2-4: The compressive strength of three test sets of 5 cylinders hardened at different temperatures. SD=standard deviation.

The divergence in mean compressive strength is minor compared to the standard deviation and therefore the hardening temperature of the grout is assumed not to influence the results.

2.3. Steel test

A dog bone is milled from a tube and tested for axial tension. Due to the curvature of the dog bone, the test was carried out by Force Technology [2.7].

The steel for the tubes is S235 with a characteristic strength, f_{yk} of 235 MPa.

The result of the tensile test of the steel is shown in table 2-5.

f_y [MPa]	E_y [‰]	f_u [MPa]	E_u [‰]
328	1.45	420	435

Table 2-5: Steel properties.

The yield strength is determined to 328 MPa at a force of 15.07 kN. The threshold is 1 kN, see appendix C. An increase in the load of 14.07 kN is equivalent to 306 MPa results in a strain of 1.46 ‰. This leads to a modulus of elasticity, E, of

$$E = \frac{f_y}{\varepsilon_y} = \frac{306\ \text{MPa}}{0.00146} = 209\ \text{GPa}$$

<div align="right">**Eq. 2-6**</div>

The value of E is within the common used range from 205-210 GPa.

The yield strength is 103 MPa (43 %) above the characteristic value, f_{yk}. It is expected to find a value higher than the f_{yk}, which expresses the 5% fractile of the steel strengths.

The ultimate strength of 420 MPa is found at a strain of 435 ‰, and the strain hardening starts at a strain of 270 ‰. These strains are assumed to be very high even for structural steel, where the ultimate strain is about 20-35 % [2.8]. This indicates, that the steel behaves as ideal plastic with no hardening until a strain of 27%.

2.4. Push-Out test

A main purpose of this project is to examine the influence of the contact properties of steel on grout in the PCFT. Therefore it is important to identify a way to remove the contact between the steel tube and the grout core.
An experimental push-out test is carried out in order to examine the way to eliminate the friction and adhesion in the contact surface. Next to this the aim is to calibrate the numerical contact model based on Coulomb friction for the modelling of the PCFT.

2.4.1. Test Setup

The steel tube used is Ø139.7/4.0 mm. The lengths of the test specimens are 150 mm and 250 mm, where the length of the grout is 100 mm and 200 mm respectively. Two tests of each length are prepared, one with full contact and one with no contact, see table 2-6 and figure 2-7.

L$_{tube}$/ L$_{grout}$	Full contact	No contact
150 mm/100 mm	1	2
250 mm/200 mm	3	4

Table 2-6: Name of test specimens.

Figure 2-7: Test specimen 2. Length of steel tube is 250 mm; length of grout is 200 mm. The steel tube is greased before trial in order to remove contact between steel and grout.

Roeder et al. [2.9] studied the bond of axially loaded CFT and found that the concrete strength does not influence the bond strength. Only HSC is examined in the experimental push-out tests. The contact properties of the PCFT with LSC grout is set to equal the PCFT with HSC grout.

Removal of contact is done by greasing the steel tube inside before grouting. The grout is cured in hot water to reach a maturity of 28 days.

The test setup is shown in figure 2-8, and the procedure is explained in appendix B.

Displacement transducers

Test specimen

Slice of a cylinder in steel
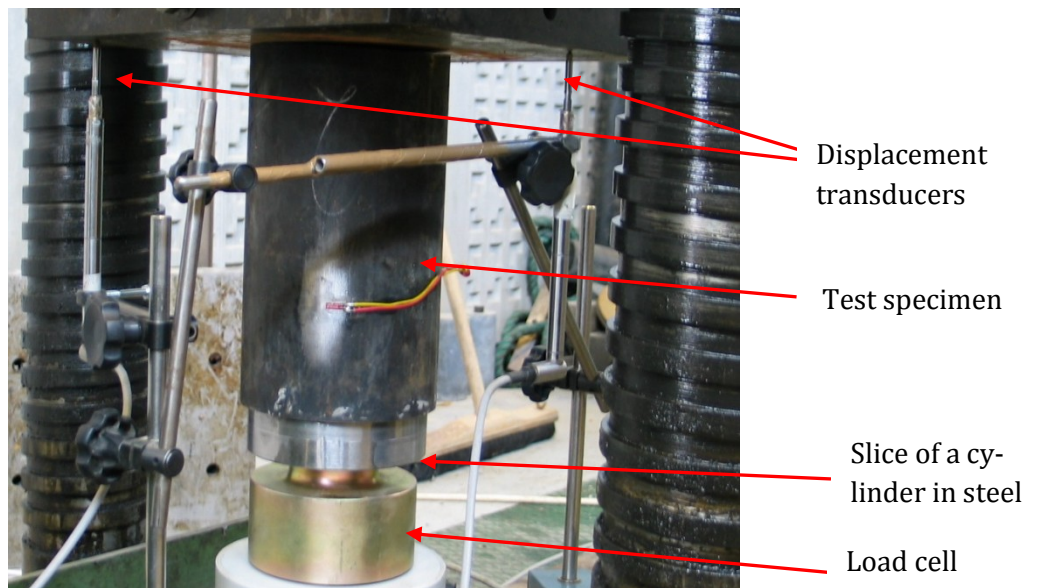
Load cell

Figure 2-8: Test setup. Load cell, steel slice and test specimen in the test machine. The displacement is measured in the diagonal corners of the press plate.

2.4.2. Test Results

Slip is defined as a displacement of 2 mm or an abrupt increase in displacement. When slip occurs the load is reduced to the threshold of 15 kN before restarting the load case. In figure 2-9 it is seen, that only the first slip happens as a slow drift of the grout core. The grout core in the

greased test specimens start sliding at 1.5 – 2.5 kN. The test results are shown in figure 2-9 and the maximal slip load, F_{slip}, is seen in table 2-7.
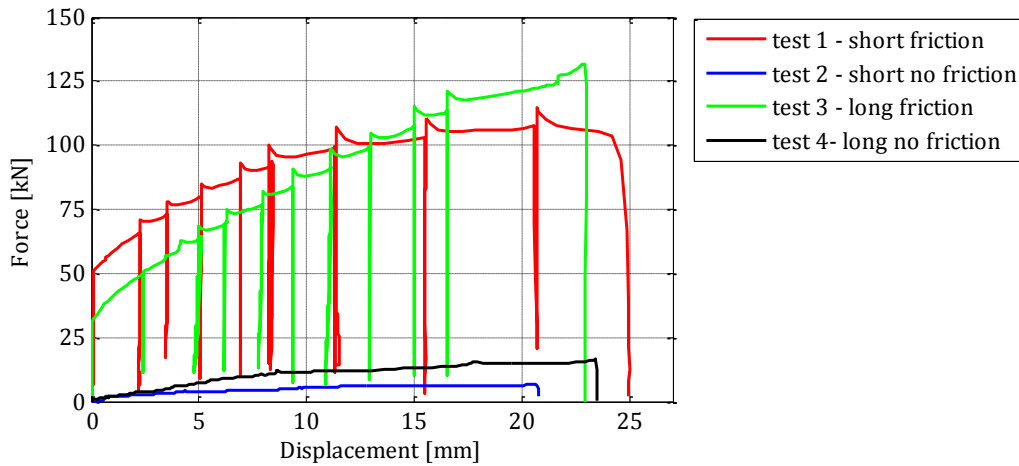

Figure 2-9: Force-displacement for the four test specimens.

Test specimen	1	2	3	4
First slip load [kN]	66.8	2.2	49.8	1.8
Ultimate slip load [kN]	115	6,7	132*	15

Table 2-7: The slip load in the push-out tests. *= slip load is not reached.

The area of contact is doubled in the long test specimen compared to the short one. Slip load is increased with about 15 %, which indicates that the friction is not the only important parameter in the contact properties between steel and grout. The displacement transducers working area are 20 mm and results at larger displacement cannot be considered valid. The ultimate slip load has not reached a fixed level for test 3 and the slip load is expected to be higher than 132 kN.

The ratio between the ultimate slip loads of the greased (no friction) specimens is 2.2. Describing the contact relations using a Coulomb friction model, the value should be 2.0 due to the ratio of the contact areas see section 0. A minor ungreased area in the greased tubes is expected to cause an increase in the slip load and can explain the divergence of 0.2 in the ratios.

The grout in the greased test specimen has been exposed to the same conditions as the non-greased, and the ratio in slip load of the greased specimens to the non-greased specimens is assumed to be transferred to the coefficient of friction, μ, see eq. 2-7.

$$\frac{F_{slip,greased}}{F_{slip,nongreased}} = \frac{\mu_{greased}}{\mu_{nongreased}} = \frac{6,7 \text{ kN}}{115 \text{ kN}} = 0,06 \qquad \textbf{Eq. 2-7}$$

The coefficient of friction in the greased PCFT is 6 % of the non-greased and it is assumed, that the friction can be ignored when the tube is greased.

References Chapter 2.

2.1 "Masterflow® 9500 – Ultra high strength, high modulus, cement based grout with applied nanotechnology for grouting offshore wind turbine installations" Technical data 11/2010.

2.2 "Betonbogen" 2nd edition. Aalborg Portland - Cementfabrikkernes teknisk oplysnings-kontor (1985). ISBN 87-980916-0-8

2.3 "Mechanical Properties of High Performance Cementious Grout II" DCE Contract Report No. 66 by Eigil V. Sørensen 6/2009

2.4 Eurocode 2 (2004) "Design of concrete structures –Part 1-1: General rules and rules for buildings".

2.5 Comite Euro-international du Beton (1991) "CEB-FIP Model Code 1990 – Design Code"

2.6 Rocco, C. et al. (2000) " Review of the splitting-test standards from a fracture mechanics point of view", Cement and Concrete Research #31   9/2000 73-82

2.7 "Prøvningrapport – trækprøvning", Tensile test of a dog bone in steel, Force Technology.

2.8 Kuhlmann, U. et al. (2009) "Steel Structures", Joint workshop of COST Actions TU0601 and E55, Ljubljana, Slovakia 9/2009

2.9 Roeder, C.W. et al. (1999) "Composite Action in Concrete Filled Tubes", Journal of Structural Engineering 5/1999   477-484

3. Experimental Study of PCFT

The experimental setup for the tests of PCFT must reflect the real problem. Due to weight of test specimens, laboratory equipment and amount of grout, it is necessary to downscale the test specimens.

3.1. Test Setup

Static system

The legs of the platform are built into a caisson at the seabed. The load is primarily distributed through the topside as axially load, transverse loads, torsion and bending moments. This thesis focus on the transverse load case and the reduced static system is set as a transverse loaded cantilever beam. The reduced static system is due to symmetry considerations transformed to a simple supported beam loaded with a concentrated force, which is easier to handle in the lab, see figure 3-1.
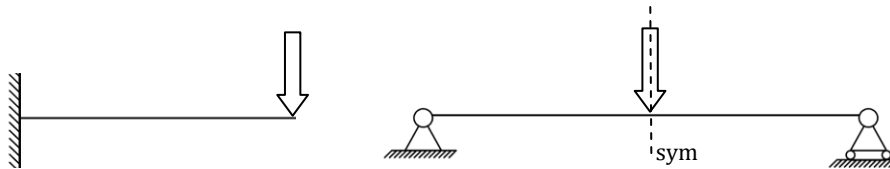
Figure 3-1: The reduced static system for the legs of the platform.

Geometry of test Specimens

The geometry of the leg of the platform is Ø3500/100 mm.

The ratio of the D/t (=35) is the decisive parameter for the geometry of the test specimen.

The dimension for the steel tube is set as Ø139.7/4.0 mm. This leads to a D/t of 34.95. The length of the test specimens, L, is chosen to 1000 mm. The length of the grout, L_{grout}, is to stop at least 1xD from the supports in order to avoid boundary effects. L_{grout} is chosen as 600 mm.

The supports in the compression testing machine are cylindrical perpendicular to the steel tube and will result in a stress concentration at the support. The steel tube is reinforced in both ends. A steel tube section Ø152.6/6.3 mm is used for reinforcing. The length of the reinforcement is 50 mm from the supports, see figure 3-2.
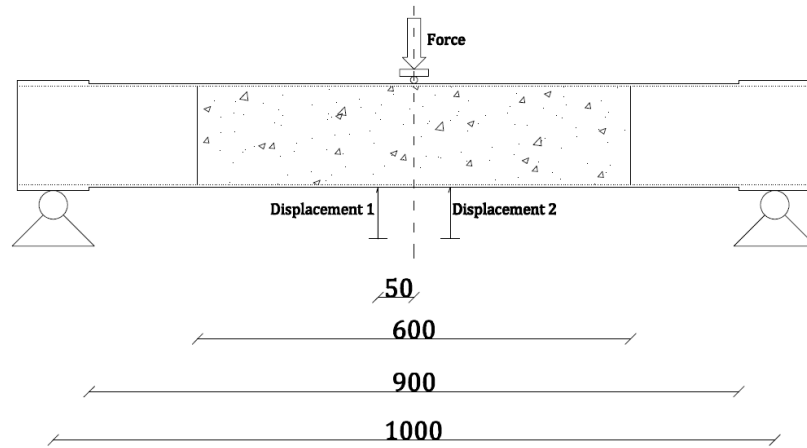
Figure 3-2: The geometry of the test specimens. Displacements are measured 50 mm on each side of the axial line of symmetry.

The empty reference tube in the setup ready to the first testing is seen in figure 3-3

Figure 3-3: Test setup for the empty tube. The local Cartesian coordinate system is defined with origo according to the figure. "1" and "2" identifies the tube halves, which describes the measuring points.

In order to prevent the steel tube from rolling when load is applied, two pieces of plywood are placed next to the reinforcement cuffs after the test specimens have been mounted on the support rolls, see figure 3-4.

Figure 3-4: Strips of plywood placed on each side of the reinforcement cuff to prevent the tube form rolling during the test.

Further details can be seen in appendix D.

3.2. Test Program

In total the test program consist of 13 test specimens: 1 empty reference tube and 12 PCFT. The purpose of the reference tube is:

1) to calibrate the numeric model and
2) to evaluate the results of the PCFTs

The PCFT are divided into 4 sets depending on the grout strength and the contact properties between grout and steel tube, see figure 3-1. For details see appendix D.

	Greased	Non-greased
HSC grouting	CFT 1-3	CFT 4-6
LSC grouting	CFT 10-12	CFT 7-9

Table 3-1: The PCFT categorized in 4 different sets depending on grout quality and contact properties. Friction is assumed to be small in greased tubes

The legs of the platform are exposed to 3 dimensional cyclic load cases which causes a cracked grout section. Therefore it is interesting to examine the mechanical behaviour of the PCFT with a cracked (cyclic) and un-cracked (static) grout section.

A load case is created as three individual load steps (LS). The amplitude is seen in figure 3-5. The negative amplitude in LS 2 symbolises that the PCFT is turned 180 degrees about the beam axis (x-axis according to figure 3-3) and reloaded. The purpose of this load step is to make sure that the grout section is fully cracked. Thus the empty steel tube is not exposed to LS 2.
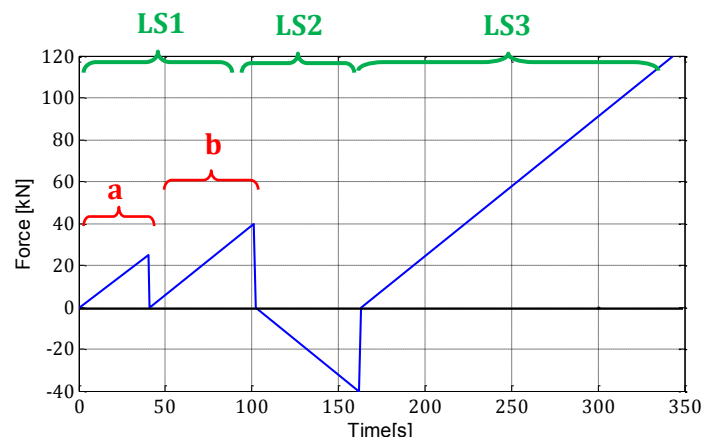
Figure 3-5: The force amplitude in the load case used for the main test program. Negative amplitude means that the test specimen has been rolled 180 degrees about the axial axis.

3.3. Test Results

3.3.1. Force-Displacement Relation

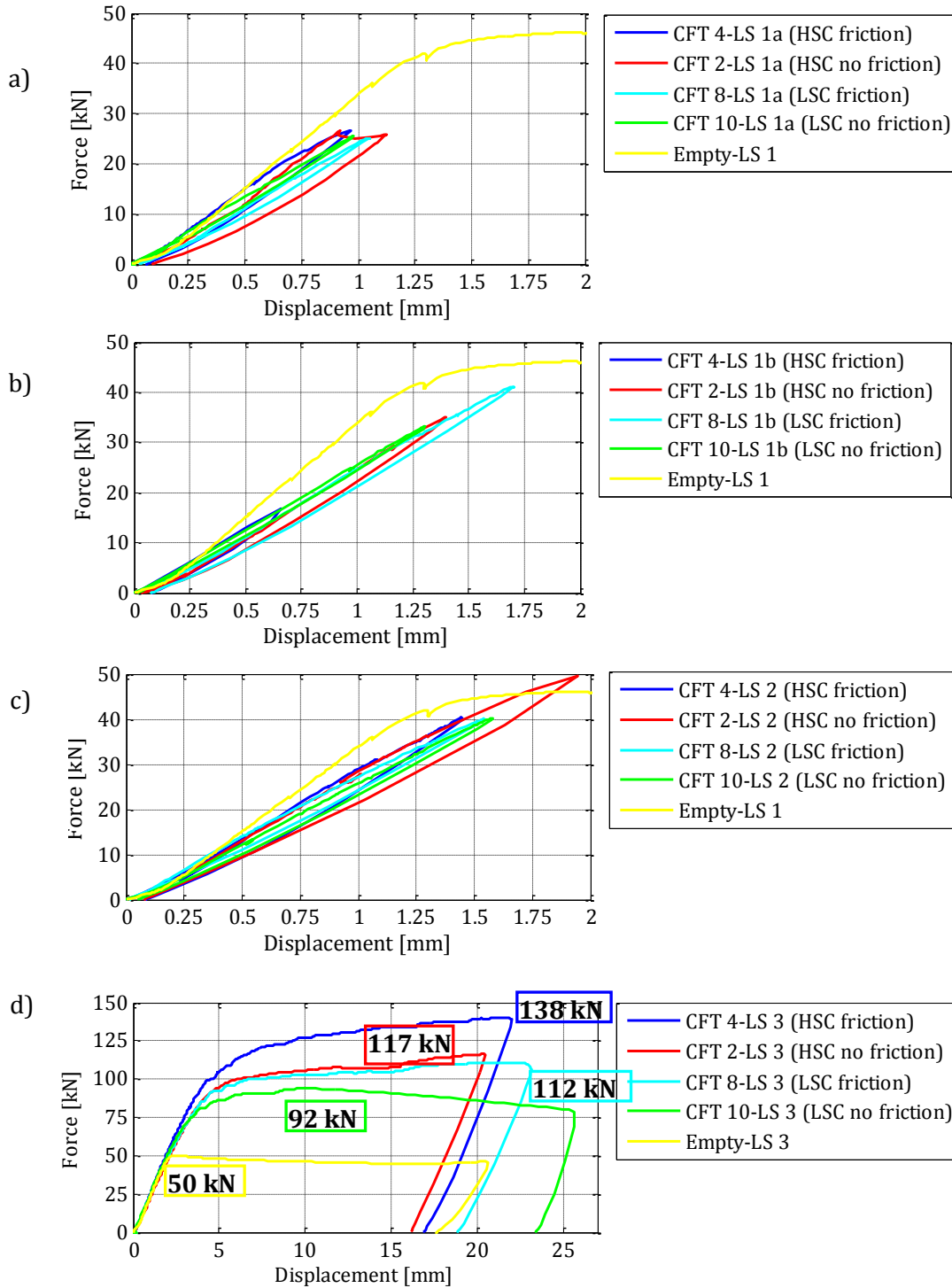The test results for all tests appear from appendix D-3. Representative tests will be shown in figure 3-6.

Figure 3-6: The force-displacement for CFT 2, 4, 8 and 10 in load step 1a, 1b, 2 and 3 (counted from the top). The peak loads is seen in d).

Below, the zoom of figure 3-6 a) shows that the PCFT with HSC grout changes stiffness. This is because the grout cracks. Particularly in the case where contact has been reduced, the change is significant. PCFT's with LSC does not show the same change in stiffness. This is because of the very low tensile strength of the concrete. The cracking starts at lower stresses and is therefore spread over a larger part in the beam axis.
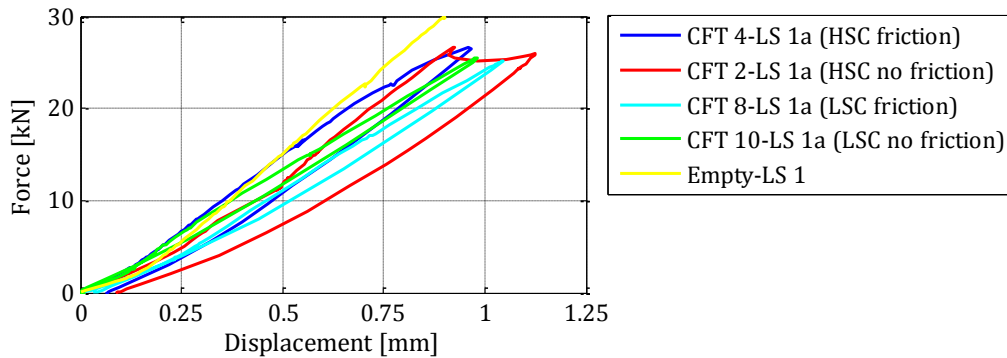
Figure 3-7: Zoom of figure 3-6 a).

Initial errors such as imperfections, pre-stresses and the fitting of the reinforcement cuffs are believed to cause the initial curvature of the force-displacement curves.

No significant tendencies in stiffness caused by the grout strength or contact relations can be concluded from figure 3-6 a)-c), but the stiffness of the empty tube seems higher than the stiffness of the PCFT's. The measuring points for the displacements are at the underside of the steel tube. The distribution of the transversal force through the cross section in the empty steel tube and the PCFT's differs. In the PCFT's the load can be lead through the grout core to the lower part of the steel section, while in case of the empty steel tube the shear force will influence the stress distribution.
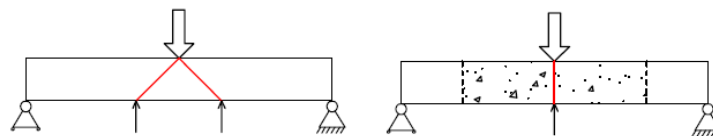
Figure 3-8: Principal distribution of the transversal force in the empty steel tube (left= and the PCFT (right).

Steel section in the PCFT.

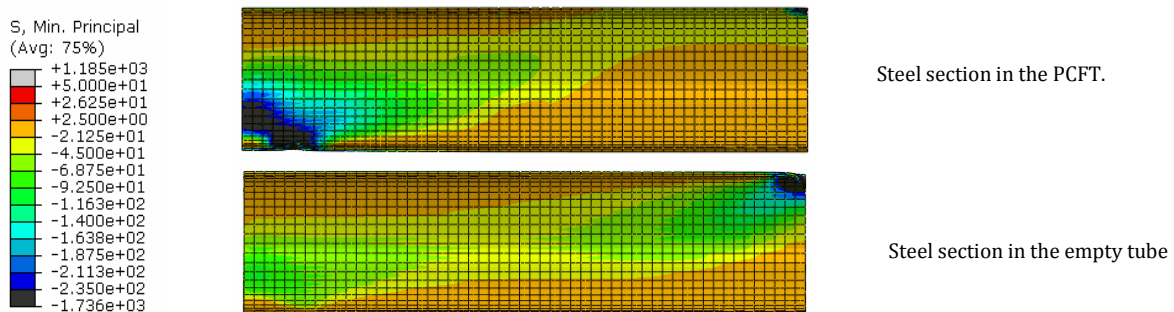Steel section in the empty tube

Figure 3-9: The min. principal stress distribution in the steel section of the empty tube (lower) and the PCFT (upper). The load is applied at the stress concentration in upper right corner.
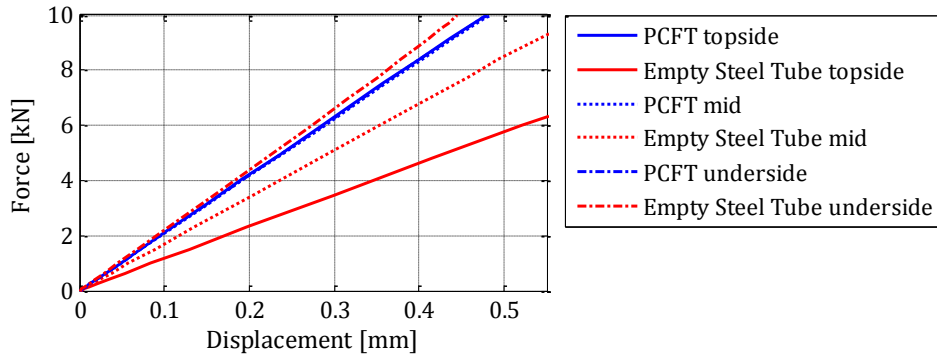
Figure 3-10: The difference in the transversal displacement of the PCFT and the empty steel tube (numeric test). The stiffness of the empty steel tube seem higher when the displacement is measured at the underside of the beam as in the experimental tests.

The stress distributions in the PCFT in figure 3-9 equals the case of pure bending due to a shear span ratio of $D/a = \frac{500 \text{ mm}}{139.7 \text{ mm}} = 3,7$

The linear force-displacement-relations are extended in all PCFT. The load which ends the elastic range of the PCFTs is about 57 - 112 % higher than the load for the empty steel tube, see table 3-2. The most significant increase is found in the non-greased PCFT with HSC grout.
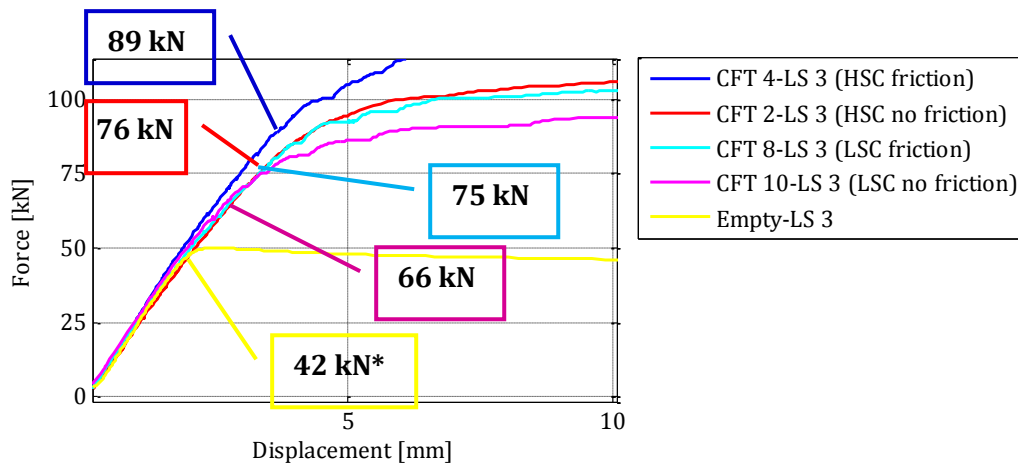
Figure 3-11: Zoom of figure 4 15 d), and the load where the linear force-displacement relations (elastic range) ends. *= in load step 1 yielding in the empty steel tube was reached at 42 kN according to figure 3-6 d), and by reloading the yielding force is 49 kN.

	HSC friction	HSC no friction	LSC friction	LSC no friction
P$_{max, elastic}$ [kN]	89	76	75	66
Increase	112 %	81 %	79 %	57 %
Peak load [kN]	138	117	112	92
Increase	176 %	134 %	124 %	84 %

Table 3-2: The increase of the linear range of the load-deflection anfd the peak load for the PCFTs compared to the empty steel tube , P$_{max, elastic}$ =42 kN; P$_{peak}$=50 kN .

Force-Strain Relation

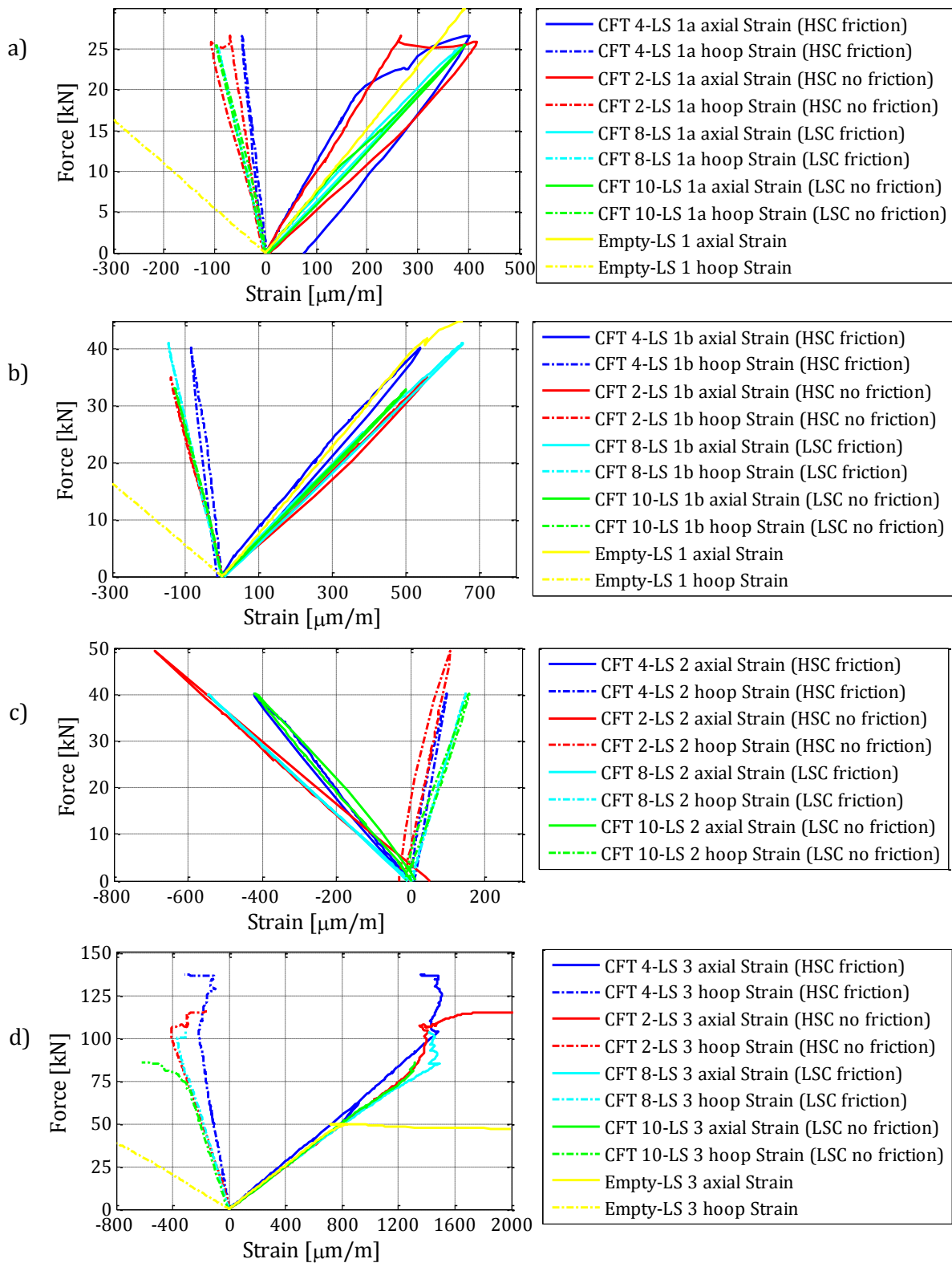The test results for all tests appear from appendix D-3. Representative tests will be shown in figure 3-12.

Figure 3-12: The force-strain relation for CFT 2, 4, 8 and 10 in load step 1a, 1b, 2 and 3 counted from the top.

The axial strain in load step 1b, 2 and 3 corresponds for all test specimens, see figure 3-12 b)-d). In load step 1a the axial strains in PCFT with HSC grout shows that the initial stiffness is higher than the stiffness of the following load steps, see figure 3-13.
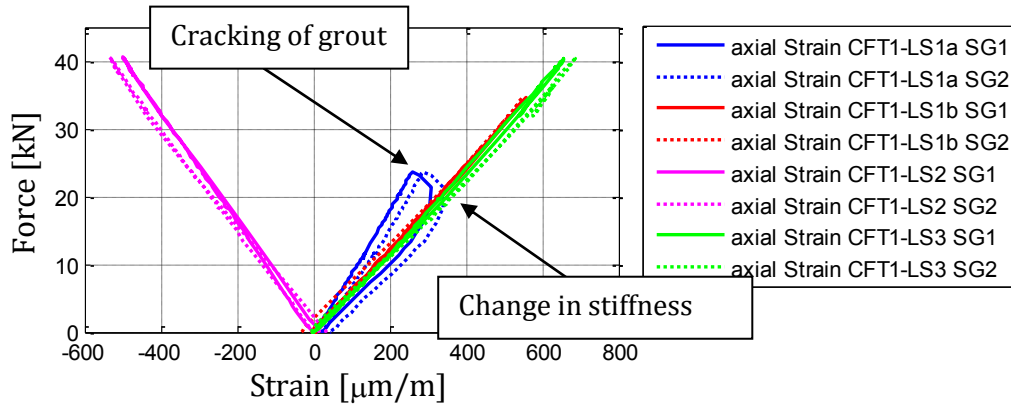

Figure 3-13: Force as function of axial strain in all load steps measured at strain gauge (SG) 1 and 2 for CFT 1. CFT1 was the initial test specimen and in LS 3 only loaded to 40 kN in order to inspect the grout core for cracks.

In the figure it is also seen, that the stiffness in load step 2, where the tube is rolled over, differs from load step 1a (unloading), 1b and 3. This is due to the fact that the strains are measured on the top of the tube instead of underneath the tube.

The cracking of the grout core happens faster in the greased PCFT than in the non-greased PCFT, see figure 3-14. The average slopes of the force-strain relations for CFT 1 and CFT 5 shows that the crack in the greased PCFT results in a loss of stiffness, while the stiffness slowly decreases for the non-greased PCFT.
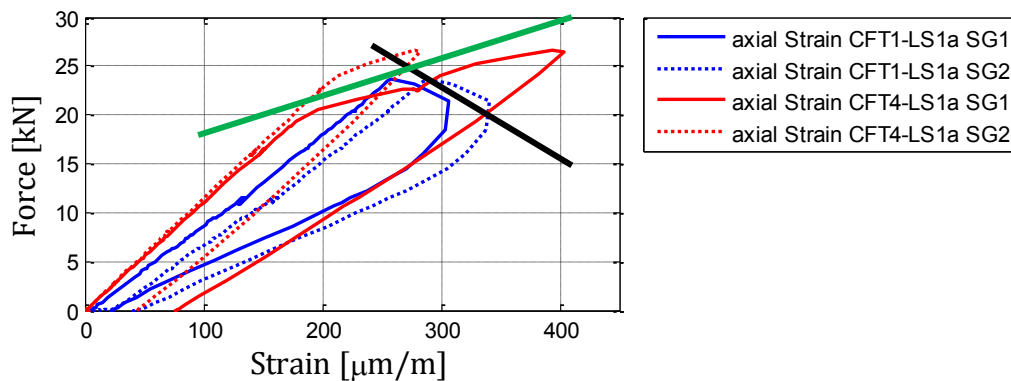

Figure 3-14: Force vs. Strain for CFT 1 and CFT 4 in load step 1a. The black and green lines (average of strain gauge 1 and 2) indicate the development of the stiffness after the grout is cracked. In CFT 1 =blue (greased tubes) the slope is descending while the slope in CFT4 (non-greased) increases.

The hoop strain in the empty tube is significant higher than the hoop strains in the PCFT at all load levels. This is due to the fact that the concrete core assists in the stress distribution through the section

3.4. Failure Mechanisms

Depending on the contact properties and the concrete strength the failure mechanism differs. The PCFT are after the bending cut open in order to inspect the grout core for failures. The opened PCFT is seen in Figure 3-15.

Figure 3-15: The PCFT prepared for inspection of the grout core. Left: CFT 2-6. Right: CFT 8-12.

3.4.1. Failure in the steel tube

No outward buckling is observed in the steel of the PCFT with LSC grout. The compressive strength of the grout is so low, that the grout crushes where the load is applied. The deformation of the steel tubes of CFT 7-12 is similar to the empty steel tube, see Figure 3-16.

Figure 3-16: The plastic deformation where the load is applied. Left: Empty. Right: CFT 9 (LSC).

For PCFT with HSC the steel tube is restrained in inward deformation, and an outward buckling happens when the deformation of the PCFT is very large (more than 40 mm vertical displacement in the middle of the PCFT), see figure 3-17.

Figure 3-17: The outward buckling of CFT 2.

3.4.2. Failure in the grout core

The bond between steel and grout seems only to influence the cracking of the grout. During load step (1a) a significant sound was observed in CFT 1 – 6 (PCFT with HSC grout), in particular in

CFT 1-3 (the greased PCFT), because of the cracking of the grout. For CFT 7-12 no significant sound was heard in the initial load step.

The crack development in the grout differs due to the contact properties and the tensile strength of the grout. There are no visible cracks in the LSC grout in the non-greased tubes, see figure 3-18. On the contrary significant cracks are found in the HSC grout, see figure 3-19.
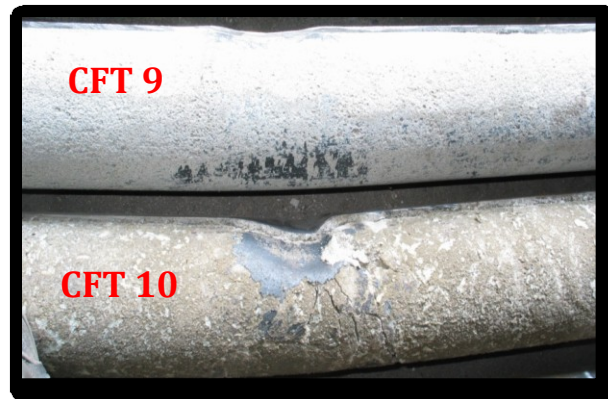

Figure 3-18: The grout core in CFT 9 (LSC non-greased) and CFT10 (greased). No visible cracks.

Also the contact properties influence the crack pattern. No contact between steel and grout leads to fewer but wider cracks see figure 3-19. In the LSC PCFT it is possible to see a few narrow cracks.

Figure 3-19: The crack in the grout for CFT 2 and CFT 5. A part of the steel tubes has been cut off in order to inspect the grout core.

4. Numerical Modelling of Concrete

4.1. General

Concrete is an inhomogeneous material and a number of factors influence the material properties of concrete e.g. the water-cement ratio, w/c, the size and type of the aggregates and the maturity of the concrete. The compressive strength and fracture energy are two important properties and other properties such as modulus of elasticity and the tensile strength are related to the parameters. The compressive strength of concrete is approximately 10-20 times larger than the tensile strength, see figure 4-1, where the stress-strain relation is shown. The stress-strain relation is characterized by different shaped non-linear curves.
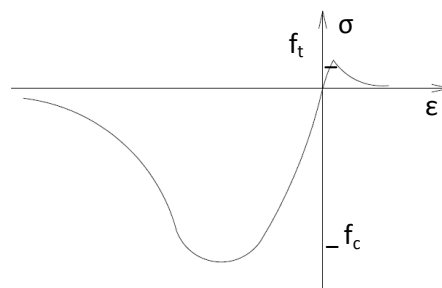
Figure 4-1: Principal stress – strain relation in concrete

When stresses in the concrete reach a certain level micro cracks are developed. If further load is applied the micro cracks join in macro cracks and causes complete failure. The transformation into macro cracks evolves fast in the tensile stress state. The cracks are related to the stress-strain relation in figure 4-1.
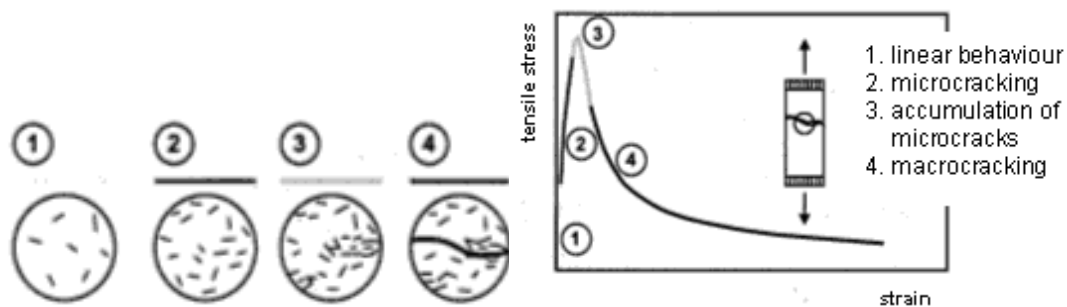

Figure 4-2: The crack evolution in relation to the tensile stress-strain relations. [4.1]

In pure tension the crack direction is to perpendicular to the load direction, which is known form the tensile axial loading or pure bending. An example of tensile cracks in the grout section of a PCFT is seen in figure 4-3. The picture is from the experiments explained in chapter 3.

Figure 4-3: The cracking of concrete in the tensile zone of a PCFT. The PCFT is tested in 3-point bending with a shear span close to 4 resulting in a failure mechanism as in pure bending.

If the concrete is exposed to compression the failure mechanism will be shear cracking or crushing depending on the tri-axial stress state. If $\sigma_1 = \sigma_2 = \sigma_3 < 0$ (hydrostatic pressure) the concrete will crush and if $\sigma_1 < \sigma_2 = \sigma_3$ the shear failure will be dominant, see figure 4-4.

Figure 4-4: The shear failure in a concrete cylinder in uniaxial compression. [4.2]

Brittle materials as concrete are rate-dependent materials. Sukontasukkul et al. [4.3] studied the loading rate in plain concrete and found that the strength of the concrete increases with the speed the load is applied, see figure 4-5.
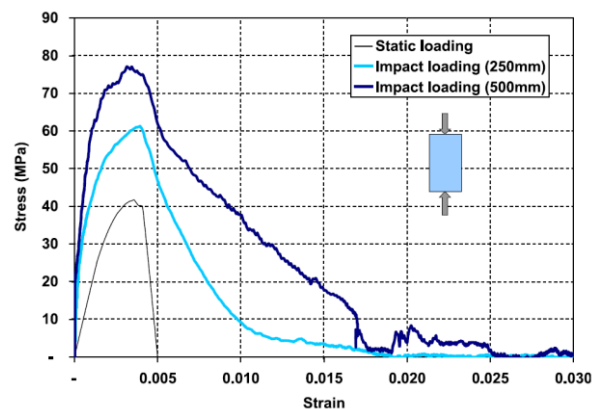
Figure 4-5: The influence of loading rate on the stress-strain relation in plain concrete. The impact loading is caused by a load hammer dropped at 250 mm (light blue curve) or 500 mm (dark blue curve).The static load was applied as a displacement controlled loading (12.7 mm pr. minute) [4.3].

When modelling concrete or other cement based materials these properties and correct failure mechanisms should be reflected in the numerical model.

4.2. Numerical Modelling of Concrete

The stress-strain relation is non-linear and the numerical model must cope with hardening and softening in the material as well as failure. Today most numerical concrete models are based on crack models or damage models.

Abaqus has more material models suitable for concrete. The Concrete Damaged Plasticity is recommended for both plain and reinforced concrete and therefore chosen for the numerical analysis in this research. The model is a combined plasticity and damage model

In general the damage theory is based on how much the material is damaged due to a load case and the cracks will close perfectly when unloading, contrary to the plasticity theory, where plastic deformation has occurred. The principles are shown in figure 4-6.
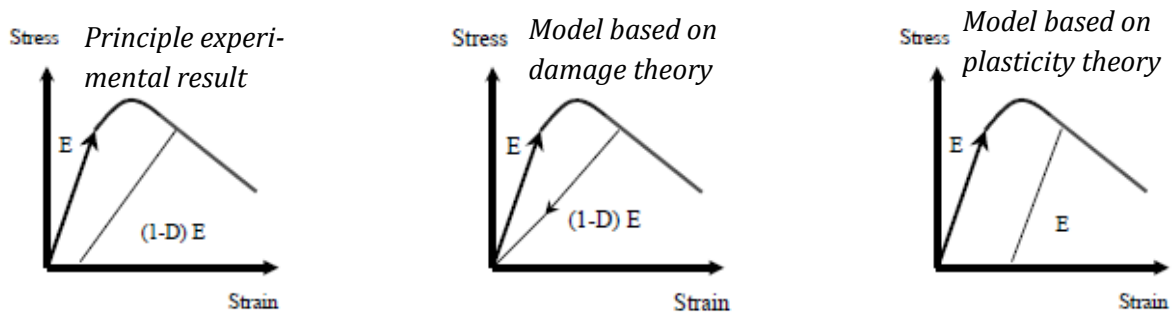
Figure 4-6: Basic differences of the damage theory and the plasticity theory. Experimental test results are found as a combination of the two models. [4.4]

4.2.1. The Plasticity Model

A numeric elasto-plastic model builds on three elements, the yield criterion the flow rule and the hardening rule.

Yield Criterion
The yield criterion, f, is a numerical expression that defines the yield limit in the principle stress space. The mathematic expression of the yield surface depends on the material properties, and the yield surface is mostly expressed in the equivalent stress, which is expressed by the stress invariants and the material strength as

$$f = \tilde{\sigma} - \sigma_0 \leq 0$$

Eq. 4-1

where

$\tilde{\sigma}$ is the equivalent stress
σ_0 is a material strength e.g. the yield stress.

The yield criterion for the plastic-damage model in Abaqus is based on the Lubliner yield function modified to take the different strength evolution in tension and compression into account, see eq. 4-2.

$$f = \frac{1}{1-\alpha}\left\{\tilde{q} - 3\alpha\tilde{p} + \beta\left(\tilde{\varepsilon}^{pl}\right)\langle\widehat{\tilde{\sigma}}_{max}\rangle - \gamma\langle-\widehat{\tilde{\sigma}}_{max}\rangle\right\} - \tilde{\sigma}_c\left(\tilde{\varepsilon}_c^{pl}\right) = 0$$

Eq. 4-2

α is defined by a relation of the compressive uniaxial strength, σ_{co}, and biaxial strength, σ_{bo} as:

$$\alpha = \frac{\sigma_{b0} - \sigma_{c0}}{2\sigma_{b0} - \sigma_{c0}} \in [0 ; 0.5] \text{ for } \frac{\sigma_{b0}}{\sigma_{c0}} \in [1.10 ; 1.16]$$

$\tilde{q}$ and $\tilde{p}$ are the equivalent effective stress and the hydrostatic compressive stress respectively. $B(\tilde{\varepsilon}^{pl})$ is a function depending on the effective compressive, $\tilde{\sigma}_c\left(\tilde{\varepsilon}_c^{pl}\right)$, and tensile stress, $\tilde{\sigma}_t\left(\tilde{\varepsilon}_t^{pl}\right)$, where $\tilde{\varepsilon}_c^{pl}$ and $\tilde{\varepsilon}_t^{pl}$ are the compressive and tensile hardening varibles. $\beta(\tilde{\varepsilon}^{pl})$ is defined as:

$$\beta(\tilde{\varepsilon}^{pl}) = \frac{\tilde{\sigma}_c\left(\tilde{\varepsilon}_c^{pl}\right)}{\tilde{\sigma}_t\left(\tilde{\varepsilon}_t^{pl}\right)}(1 - \alpha) - (1 + \alpha)$$

$\widehat{\tilde{\sigma}}_{max}$ is the maximal effective principal stress. γ is expressed in terms of the ration of the tensile meridian to the compressive meridian, K_c. γ is defined as:

$$\gamma = \frac{3(1 - K_c)}{2K_c - 1}$$

K_c is expressing the form of the yield surface in the deviatory plane is in the range of 0.5 to 1.0, where 1.0 results in a circular and 0.5 leads to a triangular shaped yield surface, see figure 4-7 . For concrete the value of K_c is close to 0.67.
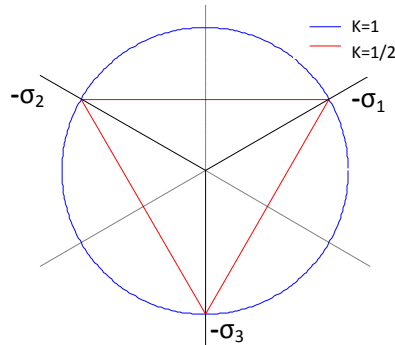

Figure 4-7: The shape of the yield surface in the deviatory plane for K=1.0 and 0.5.

$\beta(\tilde{\varepsilon}^{pl})$ and γ depend on $\langle\widehat{\tilde{\sigma}}_{max}\rangle$ and $\langle-\widehat{\tilde{\sigma}}_{max}\rangle$ respectively and cannot be active at the same time. γ only appear when the maximal effective principal stress is negative equal to a triaxial compressive stress state.
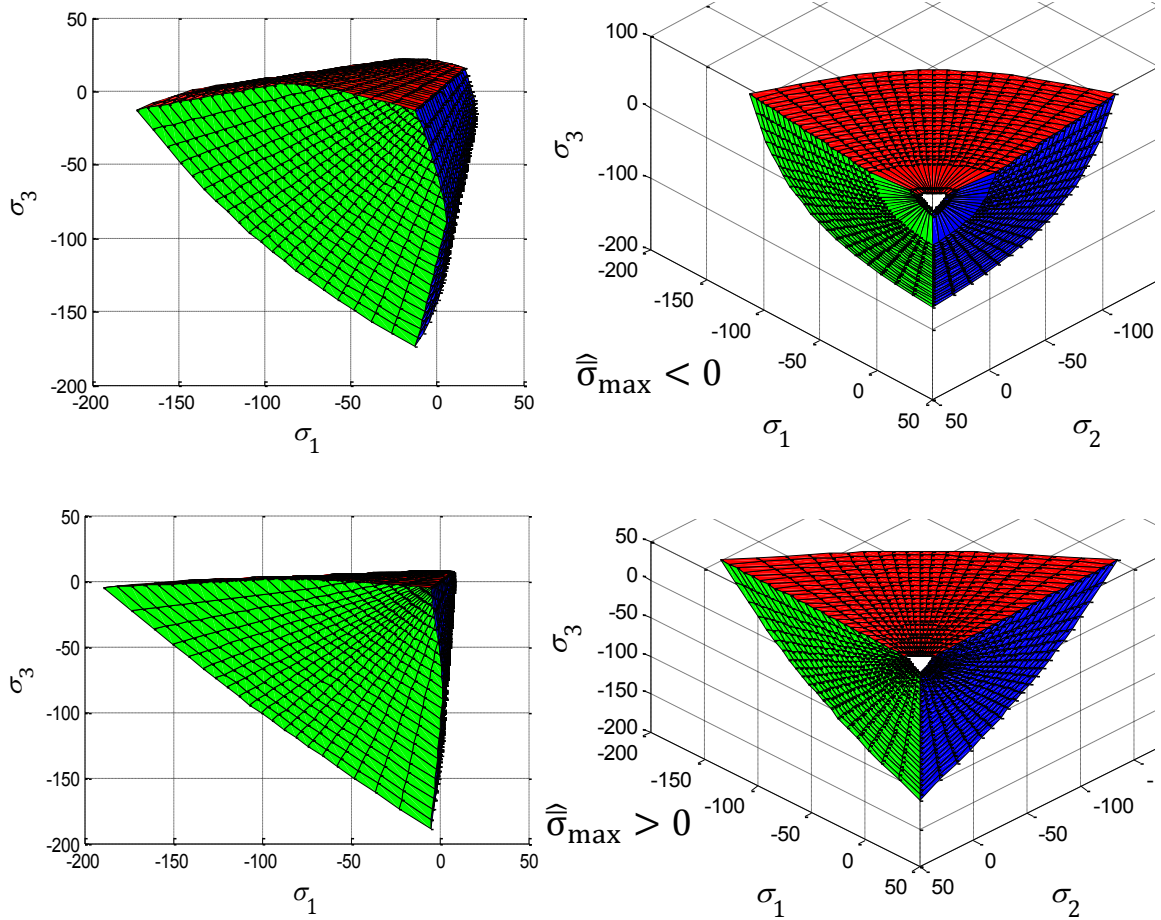
Figure 4-8: The yield surface of the modified Lubliner in the 2D view (left) and in the deviatory plane (right) for K=2/3. A triaxial compressive stress state (γ is active) is shown in the upper plots, and $\widehat{\widehat{\sigma}}_{max} > 0$ in the lower plots.

The stress state must at all times be at the yield surface. When the stress state is changed the new stress state must full fill this condition expressed as eq. 4-3

$$f(\boldsymbol{\sigma} + d\boldsymbol{\sigma}) = f(\boldsymbol{\sigma}) + \frac{\partial f}{\partial \boldsymbol{\sigma}} d\boldsymbol{\sigma} \leq 0$$

Eq. 4-3

where

$d\boldsymbol{\sigma}$ is the incremental increase in the stresses

In case of increased loading beyond the yield limit the change in stress state must be zero according to eq. 4-4. This is visualized in

Eq. 4-4

$$f(\boldsymbol{\sigma}) + \frac{\partial f}{\partial \boldsymbol{\sigma}} d\boldsymbol{\sigma} = 0 \quad \Rightarrow \quad \frac{\partial f}{\partial \boldsymbol{\sigma}} d\boldsymbol{\sigma} = 0$$
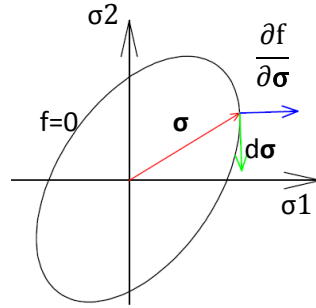
Figure 4-9: The principle plastic flow in 2D. The stress state must maintain on the yield surface. The green vector is the stress increment and the blue vector is normal to the stress increment.

Flow Rule

The total strain, $\boldsymbol{\varepsilon}$, is found as the sum of the elastic strain, $\boldsymbol{\varepsilon}_{el}$, and the plastic strain, $\boldsymbol{\varepsilon}_{pl}$. This is also valid for the strain increments

$$d\boldsymbol{\varepsilon} = d\boldsymbol{\varepsilon}_{el} + d\boldsymbol{\varepsilon}_{pl}$$

Eq. 4-5

In the numeric iteration process, the flow rule determines the plastic strain increment and the new stress state. The flow rule defines $d\boldsymbol{\varepsilon}_{pl}$ by the means of the plastic multiplier, λ, and the plastic potential, g, according to eq. 4-6.

$$d\boldsymbol{\varepsilon}_{pl} = d\lambda \cdot \frac{\partial g}{\partial \boldsymbol{\sigma}}$$

Eq. 4-6

The plastic potential is defined as a surface to which $d\boldsymbol{\varepsilon}_{pl}$ is normal, see figure 4-10.
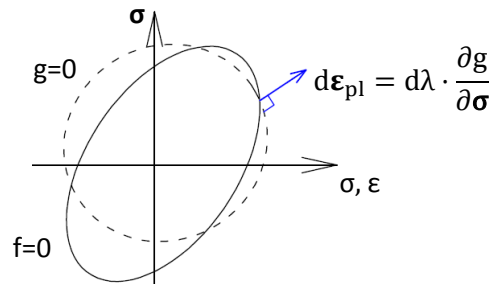
Figure 4-10: The plastic strain increment normal to the plastic potential, g=0, and the yield surface, f=0.

The present numerical material model uses non-associated plasticity, and the plastic potential is defined as Eq. 4-7

$$g = \sqrt{(\epsilon \cdot \sigma_{t0} \cdot \tan\psi)^2 + \tilde{q}^2} - \tilde{p} \cdot \tan\psi$$

Eq. 4-7

where

ψ is the angle of dilatation

σ_{t0} is the tensile uniaxial strength of the concrete

ϵ is the eccentricity, defines the rate the hyperbolic function approaches the asymptote. If ϵ=0 the plastic potential is a straight line.

The plastic potential is plotted in figure 4-11, where the influence form ψ is seen in the upper part of the figure and dg/d$\boldsymbol{\sigma}$ is visualized as the vectors in the lower plot.
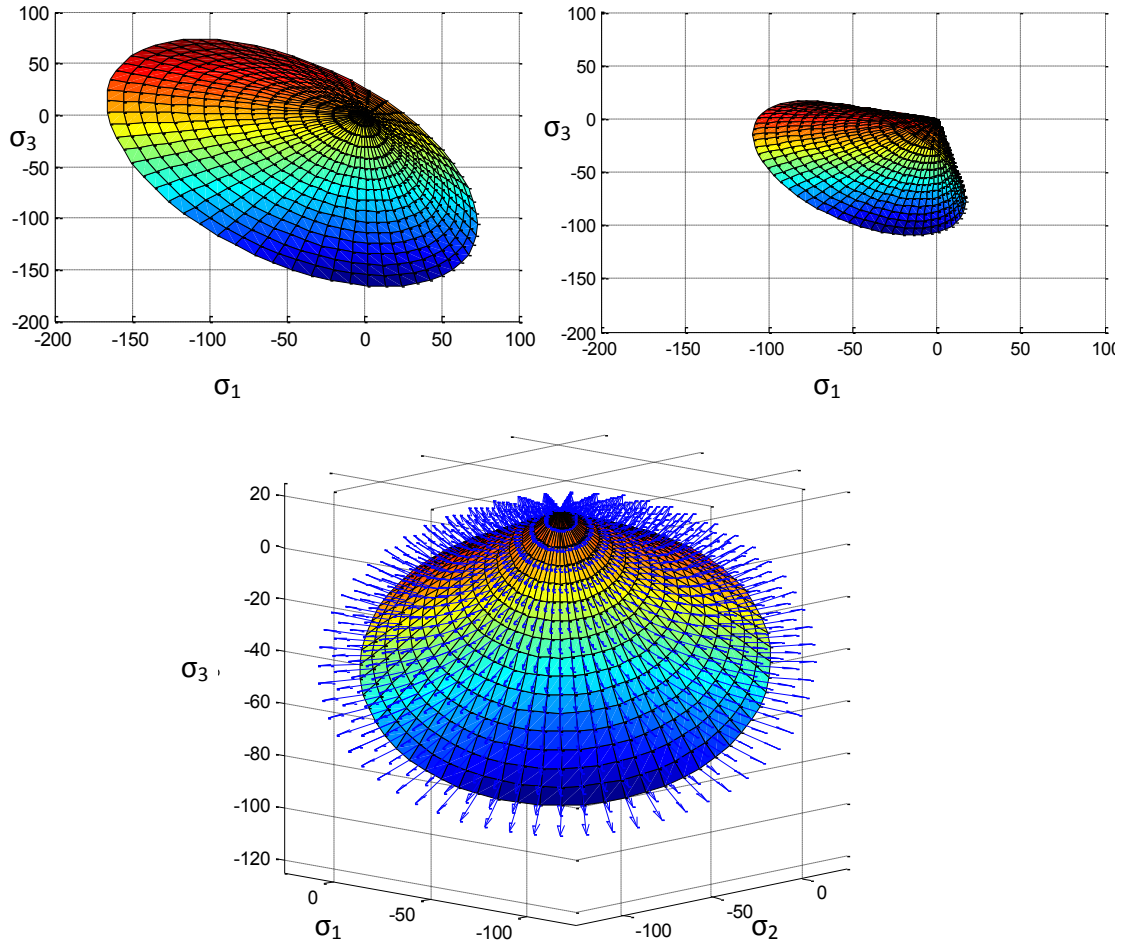
Figure 4-11: The plastic potential plotted in the principal stress space. The influence of the angle of dilatation is shown for the plastic potential in the σ₁- σ₂ plane for ψ=15° (top, left) and ψ=45° (top right and bottom). The vectors in the lower plot indicate dg/dσ.

Hardening Rule

In order to handle the change in the material strength a hardening rule is implemented in the model where the material strength in eq. 4-1, σ_0, depends on the equivalent plastic strain, $\tilde{\varepsilon}_{pl}$, in tension and compression. The yield criterion is then defined as

$$f = \tilde{\sigma} - \sigma_0(\tilde{\varepsilon}_{pl}) = 0 \qquad \text{Eq. 4-8}$$

At the incremental level this becomes

$$df = \left(\frac{\partial f}{\partial \boldsymbol{\sigma}}\right)^T \cdot d\boldsymbol{\sigma} - \left(\frac{\partial f}{\partial \sigma_0}\frac{\partial \sigma_0}{\partial \tilde{\varepsilon}_{pl}}\right)d\tilde{\varepsilon}_{pl} = \left(\frac{\partial f}{\partial \boldsymbol{\sigma}}\right)^T \cdot d\boldsymbol{\sigma} - H d\tilde{\varepsilon}_{pl} = 0 \qquad \text{Eq. 4-9}$$

The hardening parameter, H, is described by $\frac{\partial f}{\partial \sigma_0}$, which controls the changes in the size and shape of the yield surface in the deviatory plane and $\frac{\partial \sigma_0}{\partial \tilde{\varepsilon}_{pl}}$, describing the hardening evolution [4.5].

In the present material model the hardening rule is isotropic, which means that the center of the yield surface remains at origo in the stress space.

Test example: Visualization of hardening models
In order to illustrate the influence of the hardening rule, a cantilever beam 100x10x10 mm, see figure 4-12 is modelled with a:

- Plastic model
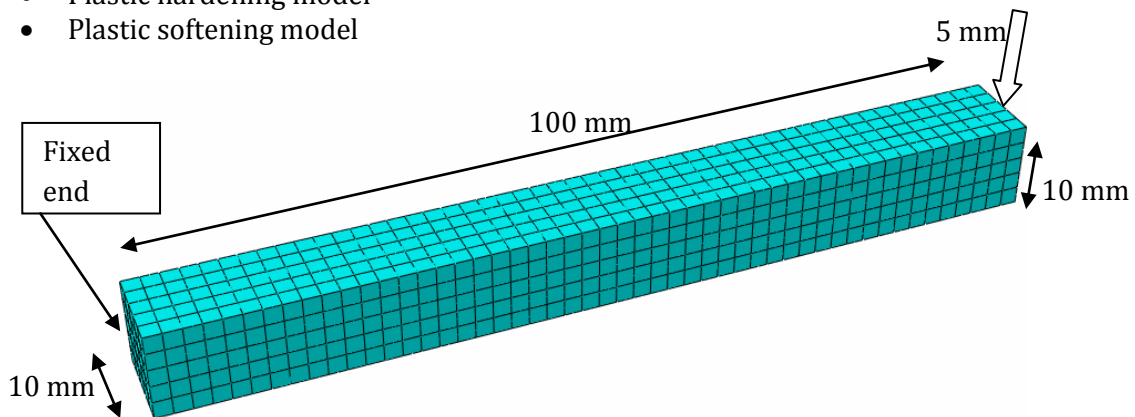- Plastic hardening model
- Plastic softening model

Figure 4-12: A cantilever beam 100x10x10 mm exposed to a transverse loading is tested. Three material models are used: a plastic model, a plastic hardening and a plastic softening model.

The stress-strain relations for the material models and the global force-displacement relation are seen in figure 4-13.
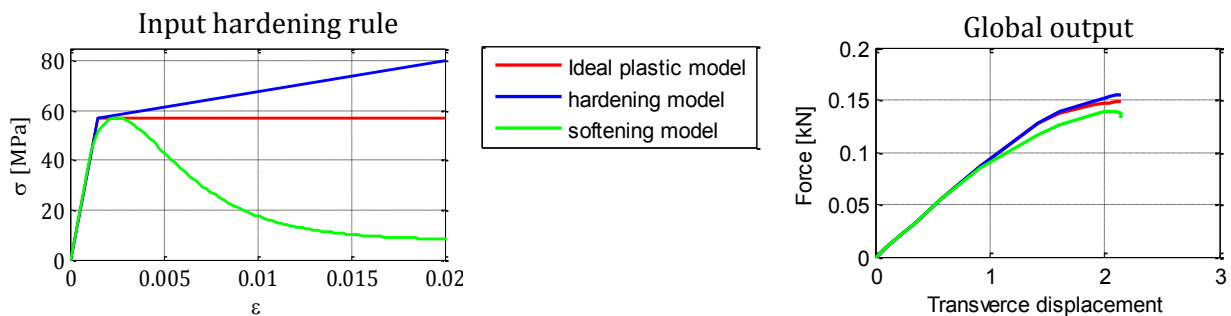
Figure 4-13: Three different hardening models, an linear elastic-ideal plastic model, a bi-linear plastic hardening model and a softening model (left) . The influence on the global load-displacement relation at the tip of the beam is seen to the right.

4.2.2. The Damage model

The damage theory expresses the damage state in the material. The theory is like the plasticity theory based on the equivalent strain. The damage models operate with a damage loading function, f_d, regulating the evolution of the damage and a set of conditions telling when the damage increases. The theory is further described in the 9th semester report.

The damage model integrated in the Plastic Damage model in Abaqus degrades the material stiffness due to the local damage by using a scalar stiffness degradation variable, ω. The elastic stiffness is reduced by multiplying the undamaged part of the material, $(1-\omega)$, to the initial undamaged elastic stiffness matrix, $\mathbf{D}_0^{el}$,

$$\mathbf{D}^{el} = (1 - \omega) \cdot \mathbf{D}_0^{el}$$

<div align="right">Eq. 4-10</div>

The stress-strain relation is then determined as eq. 4-11

$$\boldsymbol{\sigma} = \mathbf{D}^{el}{:}\left(\boldsymbol{\varepsilon} - \boldsymbol{\varepsilon}^{pl}\right) = (1 - \omega) \cdot \mathbf{D}_0^{el}{:}\left(\boldsymbol{\varepsilon} - \boldsymbol{\varepsilon}^{pl}\right)$$

<div align="right">Eq. 4-11</div>

The definition of the effective stress, $\overline{\boldsymbol{\sigma}}$, leads to the correlation between the nominal stress, the effective stress and the damage, see eq. 4-12.

$$\overline{\boldsymbol{\sigma}} \equiv \mathbf{D}_0^{el}{:}\left(\boldsymbol{\varepsilon} - \boldsymbol{\varepsilon}^{pl}\right) \Longleftrightarrow \boldsymbol{\sigma} = (1 - \omega)\overline{\boldsymbol{\sigma}}$$

<div align="right">Eq. 4-12</div>

The damage in the material is influenced by the damage caused by both the tensile and the compressive strains. In the Plastic-Damage model in Abaqus, the damage is isotrop, and ω is defined in terms of the compressive damage parameter, ω_c, and the tensile damage parameter, ω_c, as in eq. 4-13

$$(1 - \omega) = (1 - s_t\omega_c) \cdot (1 - s_c\omega_t)$$

<div align="right">Eq. 4-13</div>

Where

    s_c and s_t are functions depending on the stress state and are related to the compressive and tensile stiffness recovery. They are defined as

$$s_t = 1 - w_t \cdot r(\boldsymbol{\sigma})$$
$$s_c = 1 - w_c \cdot (1 - r(\boldsymbol{\sigma}))$$

<div align="right">Eq. 4-14</div>

w_t and w_c are weights in the range of 0 to 1 defining how much stiffness can be regained when the stress direction is changed, see figure 4-14 for this behaviour in the uniaxial stress state and $r(\boldsymbol{\sigma})$ is a direction weight in the range of 0 to 1 defined by the principal stresses.
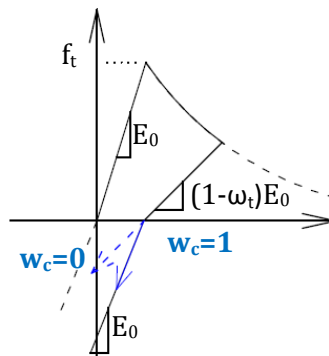

Figure 4-14: The influence of the weights in the uniaxial load directions (blue vectors). The unbroken vector is the default directions meaning that a crack does not influence the ability to transfer compressive stresses.

Test example: Visualization of the localization and relaxation in the model

The material in various parts of the construction element does not have to be in the same stress-strain state. This is illustrated in figure 4-15, where the stress-strain relation extracted in an integration point of three elements in a concrete beam with a notch exposed to 3 point bending is plotted. The localization of the damage in the crack causes a relaxation in the elements next to the most stressed element.

The model used for this illustration is a concrete beam with a notch in 3-point bending. The model is described in details in section 4.4. A zoom of the notch and the damage evolution in the crack is shown in figure 4-15. The stress-strain relation in a integration point in the three elements pointed out in figure 4-15 and the damage evolution is seen in figure 4-16
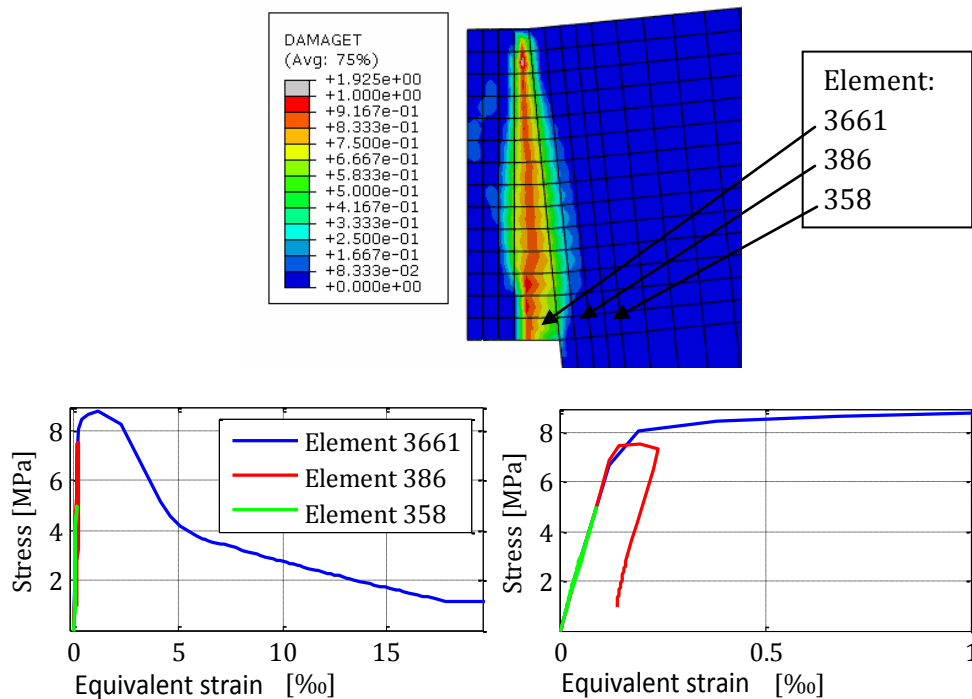
Figure 4-15: The stress-strain relation in a integration point of three elements in or near the crack. Element 3661 is located in the notch, 386 just outside the notch. Element 358 is neigbouring 386. A zoom (rigth) shows how element 358 relaxes when the damage is gathered in 3661. f_t in the model is 7.9 MPa.
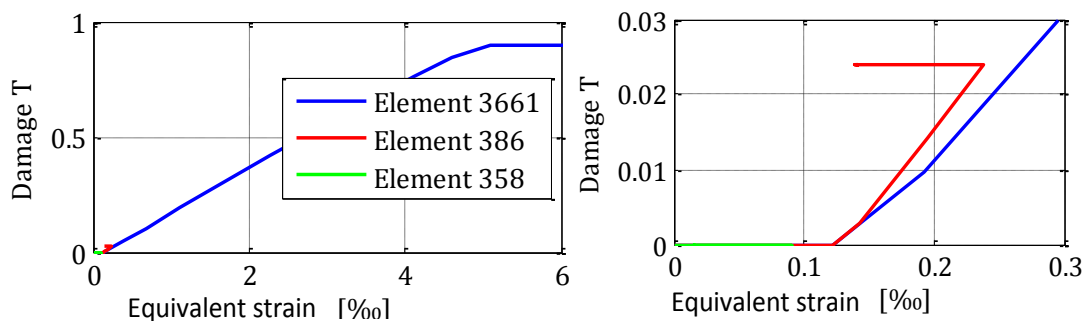
Figure 4-16: The corresponding tensile damage in the integration points of figure 4-15. In the zoom of the plot (right) it is seen, that the damage level is kept when the relaxation occours.

The stress state in element 386 reaches the tensile strength, and plastic deformation causes, that the degradation does not point to origo. The stiffness in the relaxation is very close to the initial stiffness, because the damage in this element is small. Element 358 never reaches tensile strength and the unloading stress-strain relation follows the initial stiffness.

4.2.3. Viscoplastic regularization

The softening in particular can cause numerically convergence problems and mesh-dependent solutions. Especially when the rate of the change in the slope of the stress-strain relation is high like at the peak of the curve. A way to overcome these problems is the use of viscoplastic regularization in the constitutive equations. This technique is available in the Plastic-Damage model in Abaqus, where the viscoplastic strain rate, $d\varepsilon_{pl,\ v}$, is defined as the difference in the plastic and the viscoplastic strain, $\varepsilon_{pl,\ v}$, divided by the viscosity parameter, μ, as in eq. 4-15

$$d\boldsymbol{\varepsilon}_{pl,\ v} = \frac{1}{\mu}\left(\boldsymbol{\varepsilon}_{pl} - \boldsymbol{\varepsilon}_{pl,\ v}\right)$$

Eq. 4-15

Equal to this, the viscoplastic damage increment, $d\omega_{\ v}$, is defined as the difference between the damage variable and the visco-stiffness degradation variable, ω_v, divided by the viscosity parameter, μ, as in Eq. 4-16

$$d\omega_{\ v} = \frac{1}{\mu}\left(\omega - \omega_{\ v}\right)$$

Eq. 4-16

The stress-strain relation can then be expressed as

$$\boldsymbol{\sigma} = (1 - \omega_{\ v}) \cdot \mathbf{D} \cdot \left(\boldsymbol{\varepsilon} - \boldsymbol{\varepsilon}_{pl,\ v}\right)$$

Eq. 4-17

If μ, is small compared to the iteration time increment the solution is improved without compromising the result. If $\mu \to 0$ the solution becomes the plastic solution and if μ is large compared to the incremental time step, the solution approaches the elastic solution.

The damage should be smeared over a part of the model corresponding to the development of the micro cracking. The micro cracking spreads from the most stressed part of the model and when the macro cracking initiates, the less stressed areas experience a relaxation. The viscoplasticity helps distributing the stresses to more elements in the mesh so the crack does not develops in one element row, see figure 4-17, a plot of the beam with a notch in 3 point bending described in section 4.4.
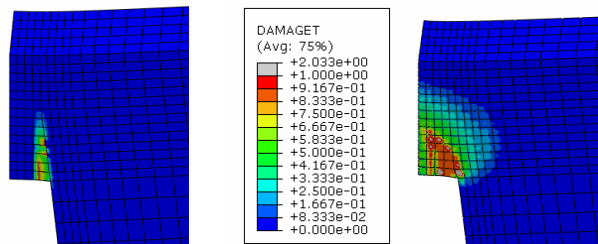

Figure 4-17: The influence of μ on the damage distribution in a notched beam in 3-point bending.

4.3. Input Parameters

The Plastic-Damage model must be setup to the concrete used in the construction element.

4.3.1. Hardening

The hardening input in the numerical model in Abaqus can be based on a:

- Stress- plastic strain relation
- Stress-displacement or
- Fracture energy (only for the tensile softening)

There is no experimental basis for the hardening of any of the grouts used in the experimental test so the experience of other researchers must be used to find acceptable parameters.

Compressive Hardening

Lubliner et al. [4.6] has approximated the hardening of concrete in a stress-strain relation according to eq. 4-18.

$$\sigma = f_0\big[(1 + a)\exp(-b \cdot \varepsilon_{pl}) - a \cdot \exp(-2b \cdot \varepsilon_{pl})\big] \qquad \textbf{Eq. 4-18}$$

where
f_0 is the compressive (or tensile) strength of the concrete and
a and b is dimensionless constants

For a>1 the curve exhibits initially hardening replaced by softening. The value b controls the softening, see figure 4-18.
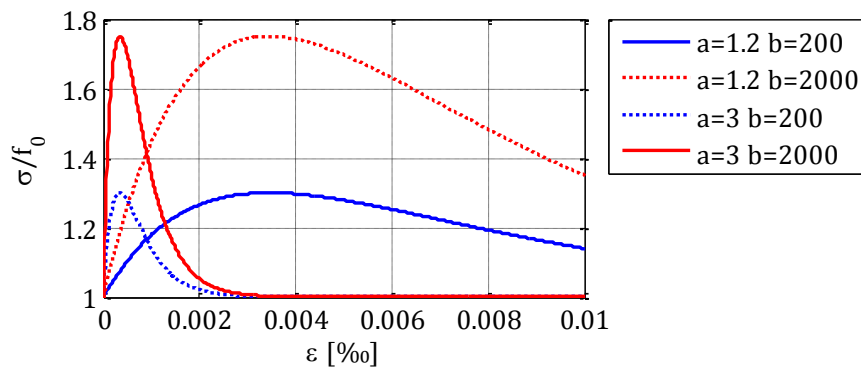
Figure 4-18: The influence of a and b on the normalized hardening expression in eq. 4-18.

For the compressive hardening of the HSC grout, a=1.2 and b=2000 has been used due to the rather brittle failure curve for high strength concrete. For the LSC grout a=3.0 and b=200 are describing the hardening.

Tensile Stiffening

Wittmann et al. [4.7] studied the fracture energy and the softening in concrete. They found, that the tensile softening can be approximated by the tensile strength of the concrete and the fracture energy. The HSC grout will be expressed in a bi-linear relation of the tensile stress and the displacement due to the cracking of the concrete due to the brittle nature of the HSC grout. The

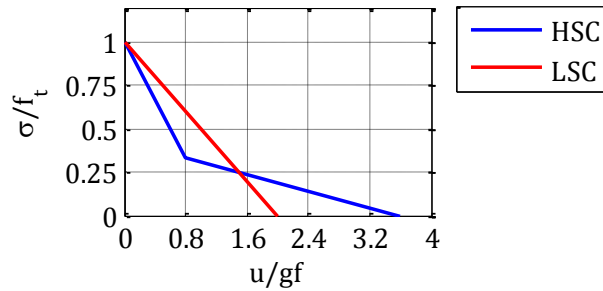softening of the LSC grout will be modelled with a linear stress-displacement relation, see figure 4-19.

Figure 4-19: The softening expressed in a linear and a bi-linear stess-displacement relation – normalized with f_t and G_f respectively.

A value of the fracture energy is to be determined in section 4.3.3.

4.3.2. Damage variables

In Abaqus the damage variables, ω_c, and ω_t, can be defined in several ways similar to the hardening. The tensile damage variable is in the present model defined by the fracture energy and the compressive damage variable by the stress-strain relation.

Compressive Damage Variable

Jirásek [4.8] has suggested a function to express the development of the damage variable. This expression, see eq. 4-19, will be used for the compressive damage variables, ω_c,

$$\omega_c = \begin{cases} 0 & \text{for } \kappa < \varepsilon_0 \\ 1 - (1 - A_c)\dfrac{\varepsilon_0}{\kappa} - A_c \cdot \exp[-B_c(\kappa - \varepsilon_0)] & \text{for } \kappa > \varepsilon_0 \end{cases} \qquad \textbf{Eq. 4-19}$$

where

κ is the maximum reached plastic strain reached in the load case
ε_0 is the yield strain and
A_c and B_c are material parameters determined by experimental testing.

The influence of A and B on the damage development is seen in figure 4-20
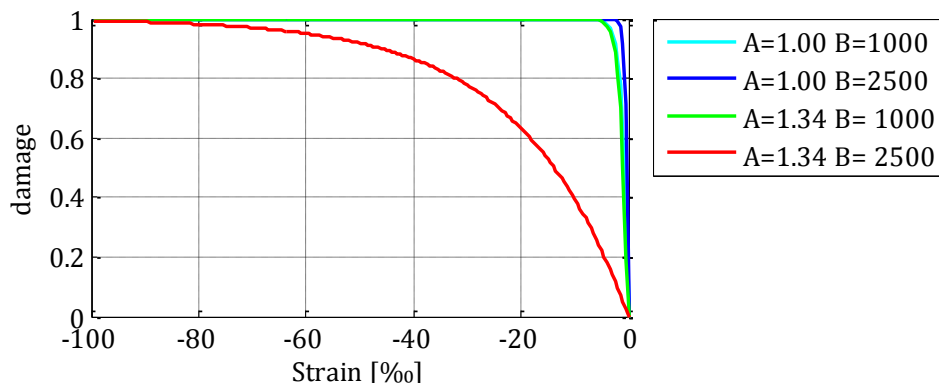
Figure 4-20: The influence of A and B on the damage development.

No experimental test has been carried out, and the material parameters has been chosen as A=1.0 and B=2500.

Tensile Damage Variable

The tensile damage variable, ω_t, is determined by the fracture energy. The development of the damage variable is approximated to be linear compared to the crack displacement, u_{ck}, see
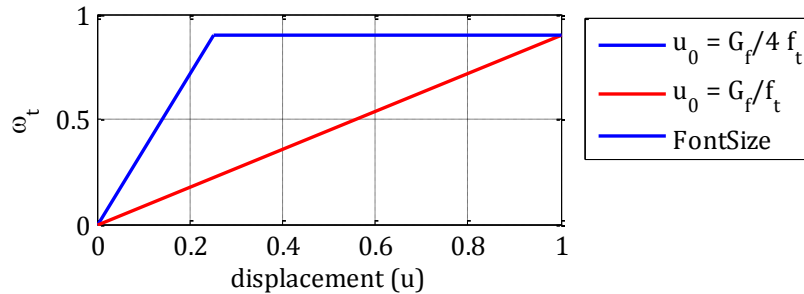

Figure 4-21: The development of the tensile damage variable.

The maximal value of ω_t, is 0.95 due to the numeric process. The value of G_f/f_t is used for the LSC grout and a value of $G_f/4f_t$ is used for the HSC grout due to the more brittle nature.

4.3.3. The Grout Properties

The values of the input parameters for the numerical material models determined in chapter 2 are according to table 4-1.

Grout	f_c [MPa]	f_t [MPa]	E_c [GPa]	ν_c [-]
LSC	7.7	0.9	10.7	0.17
HSC	115	7.9	51.7	0.17

Table 4-1: The input parameter for the numerical material model for the grout.

The plastic-damage model used to model the grout is also based on the angle of dilatation and the fracture energy.

Fracture Energy

The fracture energy, G_f, is defined as the energy required propagating a crack pr. unit area in a tension. Among others the fracture energy is influenced by the concrete compressive strength, f_c, the size of the aggregates, d_{max}, the material of aggregates, the porosity of the concrete and the loading rate [4.9]. The fracture energy is to be determined by material testing, but according to [4.10] a value can be estimated as:

$$G_f = G_{f0} \cdot \left(\frac{f_{cm}}{10 \text{ MPa}}\right)^{0.7}$$

Where:

G_{f0} is the base value of the fracture energy and depends of d_{max}. A mathematical expression for the development of Gf0 is shown in

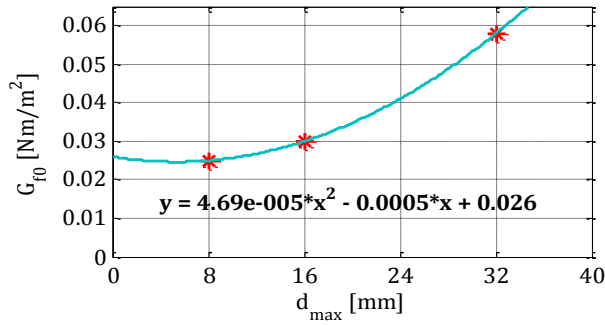f_{cm} is the mean compressive strength of the concrete and

Figure 4-22: The relation between G_{f0} and d_{max} is found with a quadratic polynomial expression. Data (red marks) is according to [4.10].

G_f for the two grout materials with d_{max} = 4 mm used in the test specimens is approximated to:

$$G_f = 24.8 \, {}^{Nm}\!/_{m^2} \cdot \begin{cases} \left(\dfrac{115.4 \text{ MPa}}{10 \text{ Mpa}}\right)^{0.7} = 137 \text{ Nm/m}^2 \text{ for HSC} \\ \left(\dfrac{7.2 \text{ MPa}}{10 \text{ Mpa}}\right)^{0.7} = 19.7 \text{ Nm/m}^2 \text{ for LSC} \end{cases}$$

Angle of Dilatation

A unique value for the angle of dilatation for concrete has not been found. Onate et al. [4.11] prescribes values between 8°-15° and others have been using 25°-30°. Nielsen and Hoang [4.12] correlate the angle of friction, θ, and the angle of dilatation, ψ, as:

$$\sin(\theta) = \tan(\psi)$$

<div align="right">Eq. 4-20</div>

θ is according to [4.13] about 37°, which leads to $\psi = 31°$.

Eccentricity

The eccentricity is in the range of 0 to 1. The default value is 0.1 and a parametric study in the 9th semester report finds the model insensitive to the parameter. The default value is chosen for the numerical model.

The ratio of the biaxial to the uniaxial compressive strength

The ratio is in the range between 1.1 and 1.2 with a typical value of 1.16 [4.14], [4.15] and this value is chosen for the analyses

4.4. Parametric study

In the 9th semester report the model has been verified to some benchmark tests. A parametric study found that the model is insensitive to the eccentricity, the ratio between the tensile and compressive meridian and the angel of dilatation.

In order to check for meds-dependency an analysis of a concrete beam is carried out in the following. The test setup is the benchmark test in the Abaqus Benchmark Manual [4.16].

4.4.1. Geometry

The concrete beam is 2000x200x100 mm and has a notch 100x40 mm at the mid span, see figure 4-23. Symmetry consideration allows a quarter of the beam to be modelled.
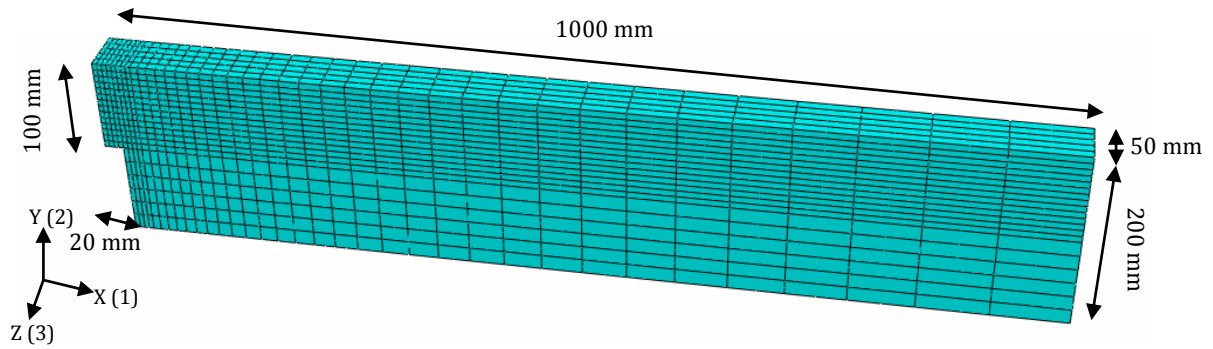
Figure 4-23: The geometry of the concrete beam. Symmetry consideration has been made. The depth=50 mm.

The material model for the beam as described before. The HSC grout is used.

4.4.2. Mesh

The beam is analysed with meshes of 2x4, 4x16 and 8x32, where the smallest number refers to the number of elements in the notch and a control zone of equal width next to the notch (the red lines in figure 4-24). The large number refers to the number of elements in the height of the beam above the notch.
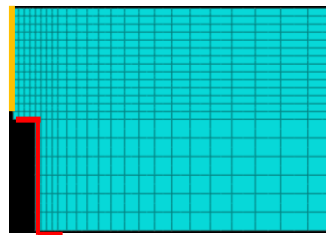

Figure 4-24: The mesh is controlled by the marked lines.

The length of the elements in the depth is 10 mm (5 elements) and kept constant in the analysis of the mesh. The element sizes in the various mesh is according to table 4-2.

Mesh	Length [mm]	Height [mm]	Depth [mm]
2x4	10	25	10
4x16	5	6.25	10
8x32	2.5	3.125	10

Table 4-2: The element sizes for the various meshes.

The element type used for the beam is the C3D20 – a solid element with 20 nodes.

4.4.3. Boundary Conditions

The cut faces are modelled as planes of symmetry are shown as the red surfaces in figure 4-25 beam is restrained in displacement out of the plane and rotations in the plane.

The lower line of the beam end is restricted in displacements in the Y-direction.

The load is applied as a displacement in the Y-direction. The load is applied to the top line of the cut face in the X-direction. The force is then determined as the reaction at the beam end.

The measuring point for the displacement in the Y-direction is shown in figure 4-25 as dU2.
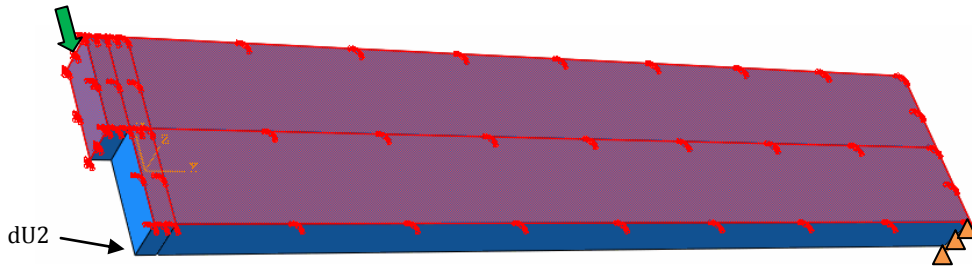
Figure 4-25: The boundary conditions. The red surfaces indicates plane of symmetry. The beam end is restricted in displacements in the Y-direction visualized by the triangles. The load is applied as a displacement of the mid beam on the line in the top of the cut face.

4.4.4. Results

Mesh

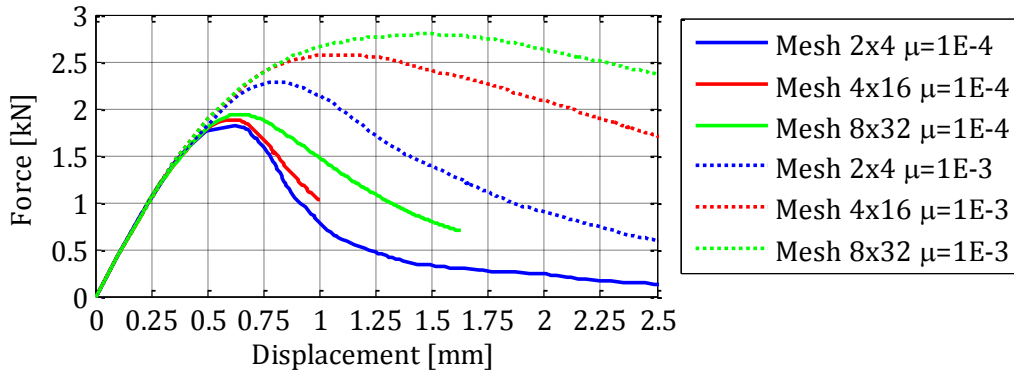The force-displacement relation for the three meshes for two viscosities is seen in figure 4-26.

Figure 4-26: The force-displacement relation for the three meshes to μ=1E-3 and μ=1E-4.

The difference in the peak loads is sensitive to the viscosity parameter. The difference in the peak load for μ=1E-4 is 6.2 % and increases to 22 % when μ=1E-3. This indicates that the model is mesh independent in the inviscid model but becomes mesh dependent when the viscoplasticity is introduced in the model.

μ	2x4 [kN]	4x16 [kN]	8x32 [kN]	Difference max/min [%]
1E-3	1.826	1.886	1.941	6.2
1E-4	2.287	2.573	2.789	22.0

Table 4-3: The peak loads from figure 4-26.

In the post peak area there is a slightly difference in the force-displacement relation, the coarser mesh the steeper slope.

Viscosity Parameter

The model sensitivity on the viscosity parameter is analysed by the 4x16 mesh. The result appears from figure 4-27. The model is highly sensitive to the value of the viscosity parameter.
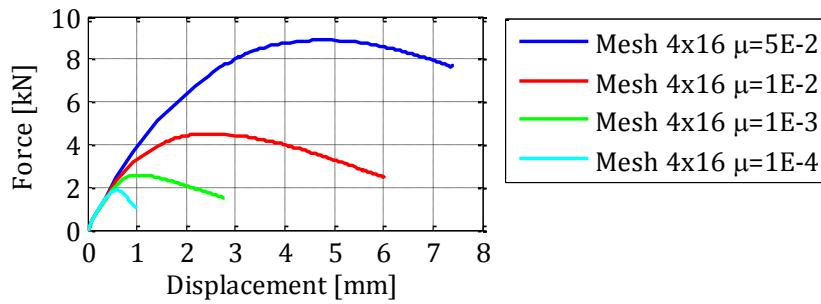
Figure 4-27: The force displacement relation for different values of the viscosity parameter

In the damage plots in figure 4-28 it is clear how the damage is smeared over a larger part of the mesh. For the μ=1E-4 the damage evolution only happens in one element. The crack band width in concrete is 3 times the size of maximal aggregate, d_{max} [4.9], for the grout used in the test, the crack band width should be about 12-20 mm equivalent to 2-3 elements.
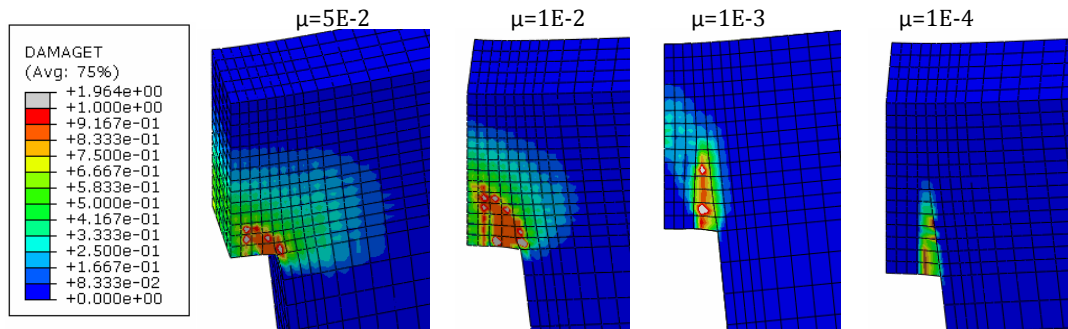

Figure 4-28: The tensile damage in the notch for mesh 4x16 for μ=5E-2 to μ=1E-4 counted from left.

Softening relation

The bilinear softening based on the fracture energy compared to the linear softening is shown in figure 4-29. The curve for the bilinear softening is as expected a little lower the curve for the linear due to the fact that the initial softening develops faster. The damage distribution is seen in figure 4-30.
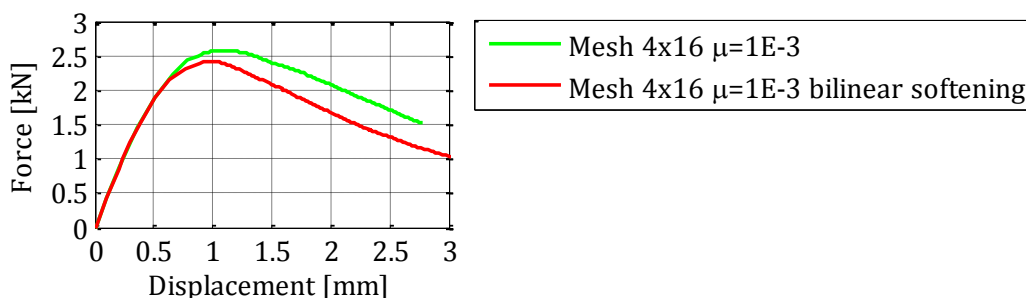
Figure 4-29: The force-displacement relation for mesh 4x16 with the linear and the bi-linear softening
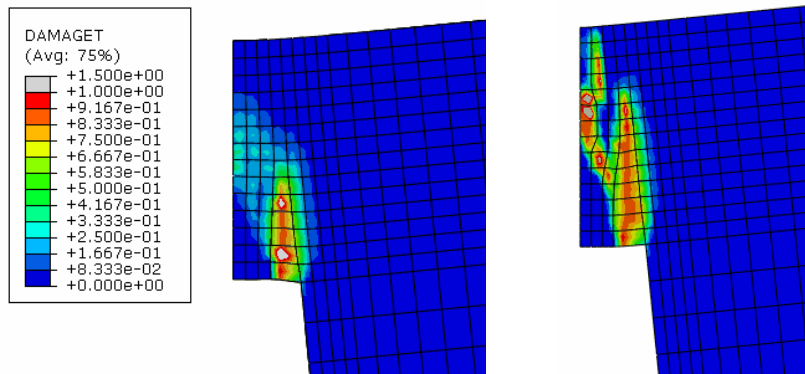
Figure 4-30: The damage distribution for the linear softening (left) and the bilinear softening (right). μ=1E-3.

The model in Abaqus allows the crack to be developed in one element row. The model operates with a characteristic crack length defined by the element type and geometry. For quadratic solid elements this length is half the length of the element. It seems as the Plastic-damage model uses this length to evaluate the fracture energy in the individual elements.

4.5. The Input Parameters

A sum up on the input parameters for the two grouts used in the PCFT's

Parameter	HSC grout	LSC grout
fc	115.4 MPa	7.7 MPa
ft	7.9 MPa	0.9 MPa
Ec	51700 MPa	10700 MPa
ν	0.17	0.17
Ψ	31°	31°
Gf	0.137 N/mm	19.7 N/mm
Softening	Bilinear σ,u): (7.9 MPa ; 0 mm) (2.63 MPa ; 0.14 mm) (0 MPa ; 0.06 mm)	Linear (σ,u): (0.9 MPa ; 0 mm) (0 MPa ; 0.022 mm)
Damage tension	Linear (ω_t,u): (0 ; 0 mm) (0.95 ; 0.011 mm)	Linear (ω_t,u): (0; 0 mm) (0.95 ; 0.011 mm)
Hardening parameters	a= 3 b=2000	a=1.2 b=200
Damage compression	A= 1 B=2500	A=1.34 B=2500

References Chapter 4

4.1 Hegger, J. et al. (2003) "The use of laser-interferometry (ESPI) in analysis of rein-forced concrete structures.
http://www.ndt.net/article/ndtce03/papers/v008/v008.htm

4.2 **Fejl! Hyperlinkreferencen er ugyl-dig.**http://civilx.unm.edu/laboratories_ss/pcc/shearfailure2.jpg

4.3 Sukontasukkul et al. (2004) " Effect of loading rate on damage of concrete", Cement and Concrete Research 34 (2004) 2127–2134

4.4 Jason, L. et al. (2004) "Damage and Plasticity for Concrete Behaviour", Jyväskylä ECCOMAS 24th -28th 7/2004

4.5 Crisfield, M.A. (1991) "Nonlinear Finite element Analysis of Solids and Structures (vol.1)" John Wiley & Son ISBN 0-471-92956-5

4.6 Lubliner, J. et al, (1989); " A Plastic-Damage Model for Concrete", int. journal Solids Structures Vol. 25 # 3/1989

4.7 Wittmann, F.H. et al.; (1988)" Fracture Energy and Strain Softening of Concrete as Determined by Means of Compact Tension Specimensmeans"; Materials and Struc-tures/Matdriaux et Constructions, #21/1988, 21-32

4.8 Jirásek, M. (2004), "Modeling of Localized Inelastic Deformation (lecture notes)"

4.9 Van Mier, J.G.M.; "Fracture Processes of Concrete". Florida, CRC-Press (1997)

4.10 Comite Euro-international du Beton (1991) "CEB-FIP Model Code 1990 – Design Code"

4.11 Oñate, E. et al. (1998); "A Constitutive Model for Cracking of Concrete Based on the Incremental Theory of Plasticity" , Eng. Computing, Vol. 5, #12/1988

4.12 Nielsen, M.P. & Hoang, L.C. (1998); "Limit Analysis and Concrete Plasticity", 1998 ISBN-13 978-0-8493-9126-2

4.13 "Betonbogen" 2nd edition. Aalborg Portland - Cementfabrikkernes teknisk oplys-ningskontor (1985). ISBN 87-980916-0-8

4.14 Feenstra, P-H. (1993), "Computational aspect of Biaxial Stress I Plain and Reinforced Concrete" Delft University Press ISBN 90-6275-935-1

4.15 Cicekli , U. et al. (2007); "A plasticity and anisotropic damage model for plain con-crete"; International Journal of Plasticity #23 /2007

4.16 Abaqus Benchmarks Manual, "Notched unreinforced concrete beam under 3-point bending". Test no. 3.2.11 in the Abaqus 6.9 Release Notes

5. The Numerical Model of the PCFT

In order to create a numerical model which can describe the behaviour of the PCFT each part of the model must be reliable. Initially the steel tube is modelled and tuned to fit the experimental test results of the empty tube.

The numerical model of the steel tube is then expanded to include the grout core. The material model from chapter 4 is used, and the interaction between steel and grout is modelled.

5.1. Modelling the Empty Steel Tube

The empty steel tube used in the experimental tests is shown in figure 5-1 and the numeric model must reflect this setup.

Figure 5-1: The empty steel tube in the test setup

5.1.1. Geometry of the Model

The empty steel tube is 1100 mm long and has a Ø139.7/4.0 mm section. The span between the supports is 1000 mm, and the load is applied at the mid span. The reinforcement cuffs are 100 mm long and made from a Ø152.4/6.2 mm tube. They are aligned with the ends of the tube.

The load is applied through a steel plate cut from the Ø152.4/6.2 mm tube. This plate has an arc length of 80 mm and a width of 50 mm.

The numeric model is made with consideration to the planes of symmetry. The models geometry is shown in figure 5-2.
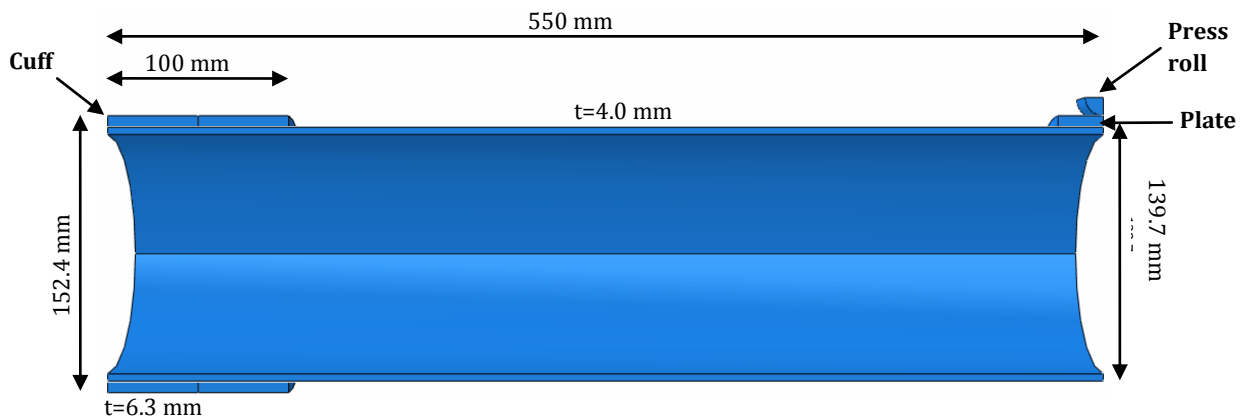
Figure 5-2: The geometry of the numeric model of the empty steel tube and the naming of setup parts.

Material model for steel

The yield criterion in the model is based on Von Mises equivalent stress formulation. The steel is modelled as linear elastic ideal plastic, see figure 5-3 with a modulus of elasticity, E_s, of 210 GPa and a yield stress of 328 MPa. This approximation is assessed to be reasonably because the ration of the yield strain, ε_y, (1.5 ‰) and the strain where the strain hardening starts (27 %) determined by testing is $\varepsilon_y / \varepsilon_{start\ strain\ hardening} = 180$ according to appendix C
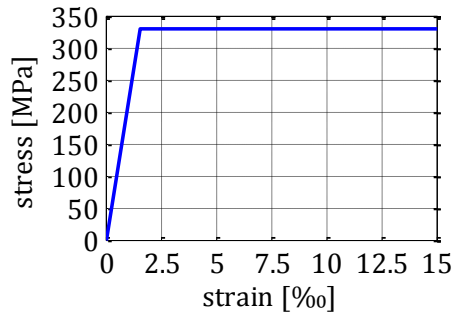
Figure 5-3: The stress-strain relation. The modulus of elasticity is 210 GPa, and f_y = 328 MPa.

All parts in the model but the press roll are modelled with this material model. The material of press roll is modelled as linear elastic with E=10000x E_s.

Poissons ratio for the steel is set to 0.3.

Elements and mesh

The tube, the cuff and the plate are modelled with solid elements, the C3D20 mentioned in section 4.4.2. The element length of the steel tube is 10 mm in square, and the thickness is modelled with three elements.

The cuff and the plate are given one elements in the thickness and a length of the cuff is 8.5 mm in square and the plate 5 mm in square.

The press roll is meshed with C3D15 in the center and C3D20 for the rest of the elements. The element length is 3 mm.

The mesh for the entire model is shown in figure 5-4.
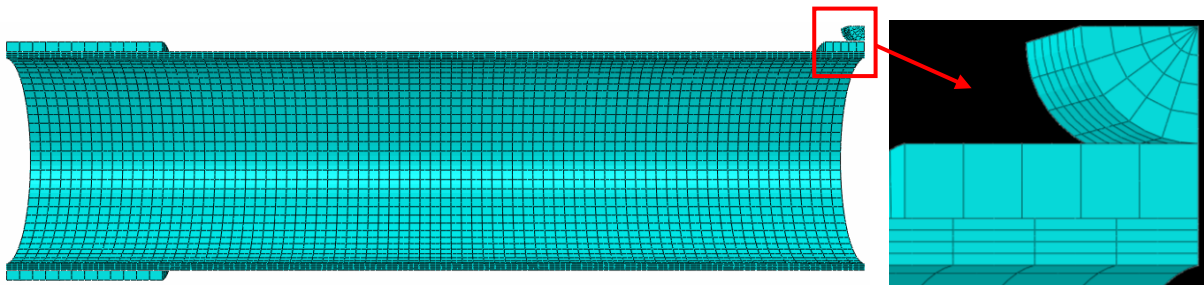
Figure 5-4: The mesh of the model (left) and a zoom of the press roll and plate (right).

Boundary conditions

Geometric restrictions

All cut faces but the top of the press roll are modelled as symmetry planes, see figure 5-5 and restricted in out-of plane displacement and in plane rotations.
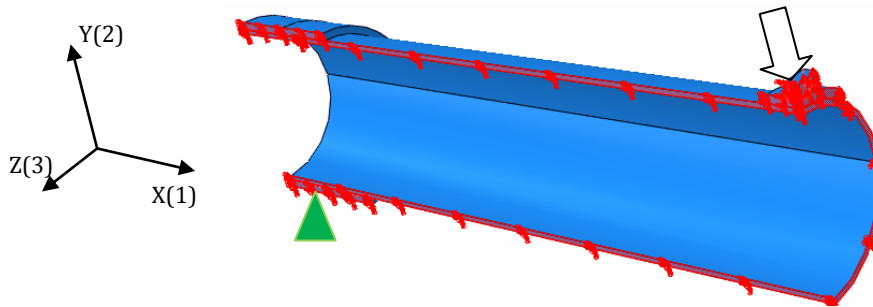

Figure 5-5: The boundary conditions. The symmetry planes are marked with red. The green triangle visualizes the support - the node is restricted in displacements in the Y-direction. The load is applied the top cut face of the press roll as a displacement in Y.

Loading

The load is applied to the top cut face of the press roll. The area is given a displacement in the Y-direction. In the case of the empty tube there is just one load direction and one load step is sufficient.

Interaction of parts

The individual parts are connected by a friction model defining the contact properties normal and tangential to the contact surface. The model is based on a master-slave relation. The master surface is allowed to penetrate the slave surface, but not vice versa, see figure 5-6.
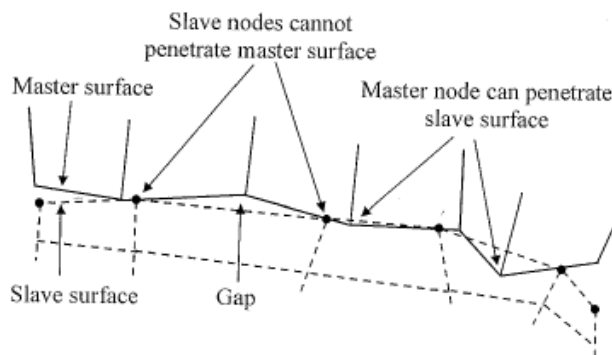
Figure 5-6: The master - slave surface relation [5.1].

The choice of master – slave surface is made by three general rules [5.2]:

1. The mesh of the slave surface should be the denser one
2. The stiffer material should be the master surface
3. The inner tube should be the slave surface

The master surfaces are then: the inner surface of the cuff, the inner surface of the plate, and the surface of the press roll.

The contact surfaces are allowed to slip in the normal direction after the first contact.

Tangential friction is defined as Coulomb friction. The critical shear stress, τ_{crit}, at which sliding between the surfaces starts, is defined by the contact pressure, p, and the coefficient of friction, μ_k, as $\tau_{crit} = p \cdot \mu_k$. The equivalent shear stress, τ_{eq}, at the contact surface is determines by the shear stresses acting perpendicular to each other (principal directions), τ_1 and τ_2, as $\tau_{eq} = \sqrt{\tau_1{}^2 + \tau_2{}^2}$ and when $\tau_{eq} < \tau_{crit}$ the surfaces stick together. The contact pressure can be transmitted when the surfaces are in contact.

The coefficient of friction steel on steel is assessed to 0.8 [5.3].

Model sensitivity
A parametric study is made in order to calibrate and optimize the model of the steel tube. The parameters to be examined are:

1. The element size, h,
2. The number of elements in the thickness, n,
3. The contact relations between cuff and steel tube.
4. An elastic of plastic material model for the cuff
5. The non linear geometry, NLGEOM
6. The yield stress

<u>Element size</u>
Decreasing the element size from 10 mm in square to 5 mm in square increases the total element number by a factor 4. The force displacement relation is seen in figure 5-7. The difference in the peak force is insignificant, but the yielding starts at a lower force for h=5 mm. Very little to gain in return for a relative large increase in the total number of elements.
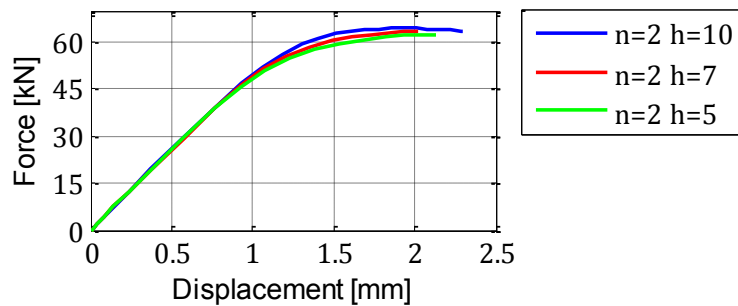
Figure 5-7: Force-displacement relation for 2 elements in the thickness and element length of 5, 7 and 10 mm in square.

Element number in thickness

The number of elements in the thickness, n, of the steel tube is important to the stress distribution. The force-displacement relation for n=2 and n=4 is shown in figure 5-8. The number of elements in the thickness influences the stiffness of the global system. The yielding spreads faster for n=2, but the effect seems insignificant in a global view.
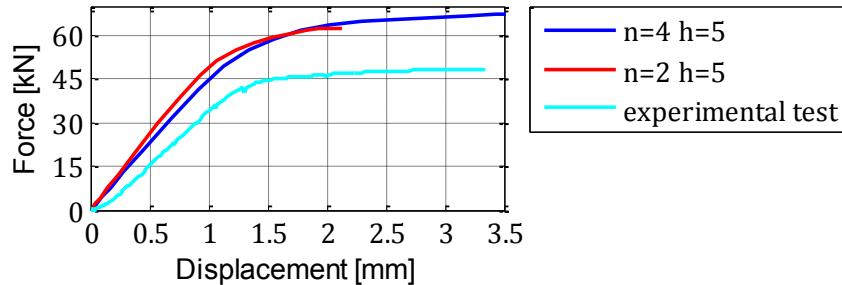

Figure 5-8: Force-displacement relation for 2 and 4 elements in the thickness and element length of 5 mm in square.

Contact Relations in the Cuff

The interaction between the cuff and the steel tube is tested for a tied connection and the contact modelled with Coulomb friction. A significant decrease in stiffness of the system occurs when the interaction is modelled with friction is seen in figure 5-9.
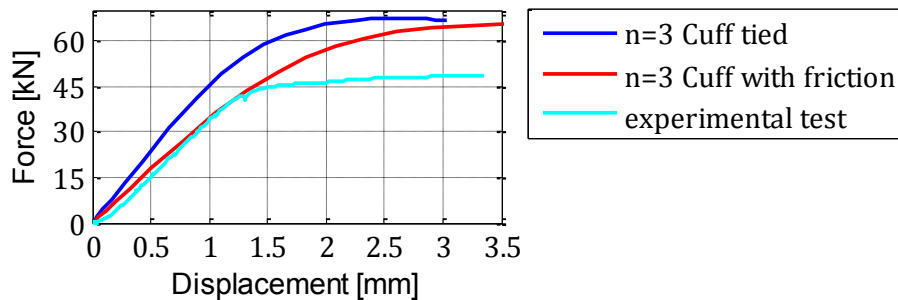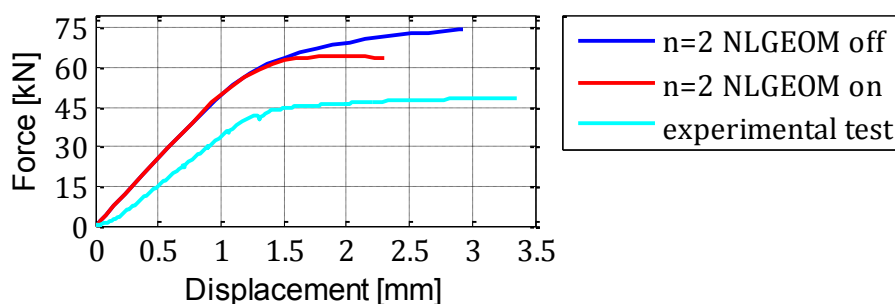

Figure 5-9: Force-displacement relation for 3 elements in the thickness and element length of 10 mm in square with the cuff tied or modelled by friction.

Material Model for the Cuff

The influence of the cuff modelled with or without the plastic material model is shown in figure 5-10. There is a significant increase in the peak load when the cuff is modelled linear elastic.
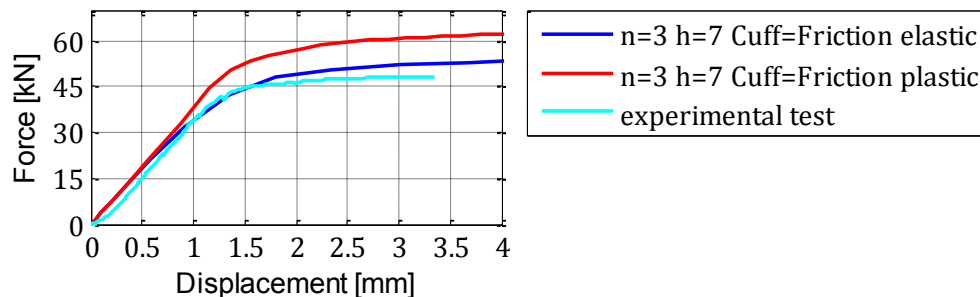
Figure 5-10: Force-displacement relation for 3 elements in the thickness and element length of 7 mm in square. The cuffs are modelled by friction with an elastic or plastic material model.

Non Linear Geometry

The steel section is a class I section, and allows yielding before buckling. According to section 3.3, the displacement for the start of the non-linearity is about 1 ‰ of the total length for the empty steel tube and 5-6 ‰ for the PCFTs. In order to check the influence of the non-linear-geometry, NLGEOM, a brief study is made with n=2 and h=10 mm in square, the result appears in figure 5-11, where range for the development of the non-linear behaviour increases when NLGEOM is deactivated.

Figure 5-11: Force-displacement relation for 2 elements in the thickness and element length of 10 mm in square with and without nonlinear geometry activated. The analysis is carried out with tied cuffs.

Yield stress

The peak load determined by the use of the yield stress found by experimental test is 20% higher than the test result, see figure 5-12. Fitting the numeric tests by tuning the yield stress, f_y is found to be 235 MPa.
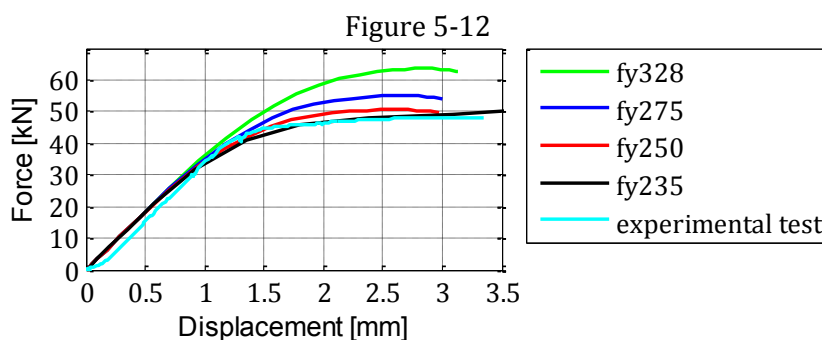
Figure 5-12: Force-displacement relation for 3 elements in the thickness and element length of 10 mm in square for different yield stresses. In the analysis for fy= 235 MPa is NLGEOM deactivated, and the cuff is modelled with friction.

In the analyses of f_y>235 MPa NLGEOM war activated. A decrease in the load after the peak occurs and the ductile behaviour of the experimental tube according to section 3.3 cannot be modelled with NLGEOM.

Simplifying the model

In order to reduce the CPU-time when solving the model of the PCFT, the model of the empty steel tube is simplified. The reinforcement cuff is removed and to maintain the flexural stiffness in the area covered by the cuff, the modulus of elasticity is increased by a factor:

$$E = \frac{I_{\text{cuff+tube}}}{I_{\text{tube}}} \cdot E_{steel} = \frac{\frac{\pi}{64} \cdot (152.4^4 - 131.7^4)\text{mm}^4}{\frac{\pi}{64} \cdot (139.7^4 - 131.7^4)\text{mm}^4} = 3$$

The load is applied in one node resulting in a numeric stress concentration in this point. In order reduce this effect an area around the loading point is modelled with a linear elastic material model. The areas are pointed out in figure 5-13.
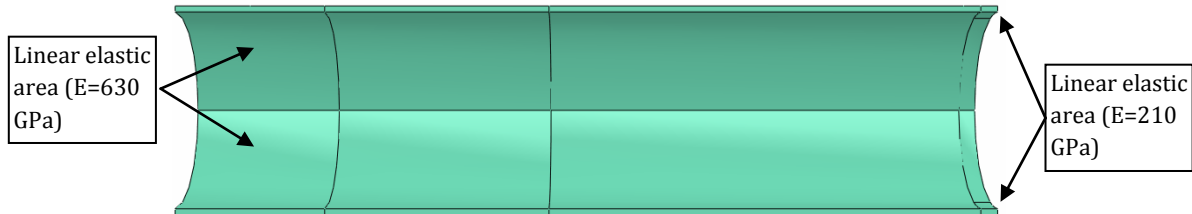

Figure 5-13: The simplified model with areas modelled linear elastic materials.

The simplification is an approximation of the conditions and will not take the non-linear behaviour of the frictional connection between the cuff and the steel tube in account. In the elastic area the difference in displacement is seen in figure 5-14. This approximation is assessed to be a fair and is assumed not to influence the results significantly
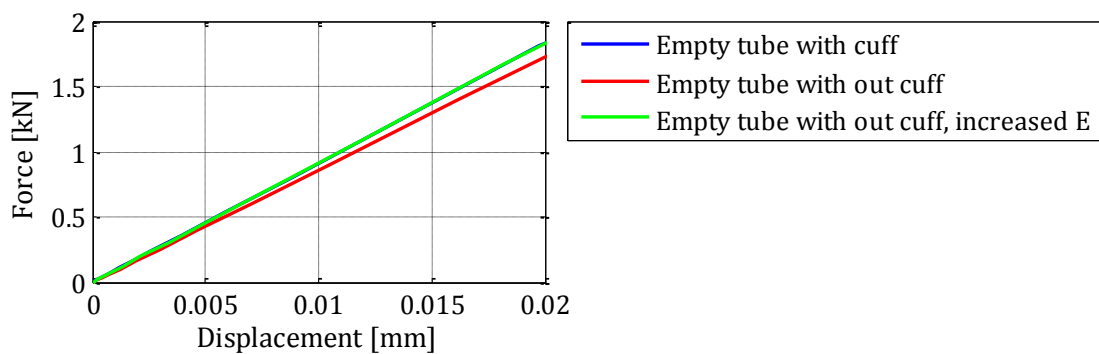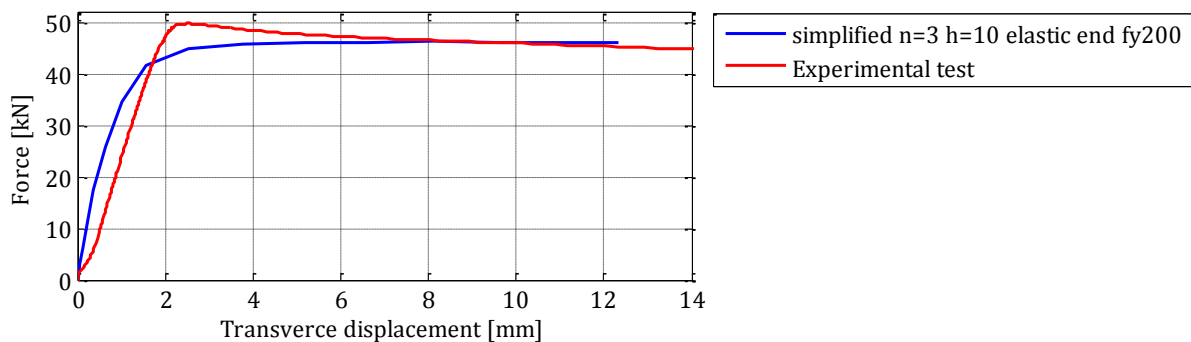

Figure 5-14: The force as function of the difference in the displacement at mid-height of the steel tube.

In the non-linear range, the peak load of the model is about 10 % lower than peak load for the steel tube tested experimental and load does not decrease in the post peak range, but the ductile behaviour is fairly the same.

The element size in the simplified model is 10 mm in square, and the thickness is modelled with 3 elements, see figure 5-15. The boundary conditions equal the one in figure 5-5, but the load is applied as a concentrated force to the top center node and the tube is restrained in displacement in the Y-direction in one node 50 mm from the end.
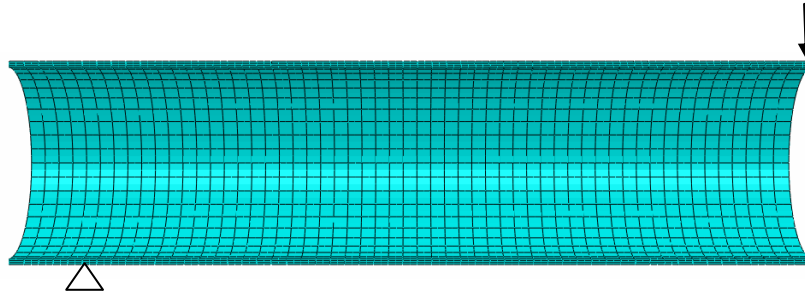

Figure 5-15: The mesh and boundary conditions. Planes of symmetry according to

5.2. Modelling the Partially Concrete Filled Tube

The model of the PCFT is based on the simplified model of the steel tube and the material model for the grout as described in section 4.

Geometry and mesh

The grout core is modelled to fit tight in the steel tube. The geometry of the grout core is shown in figure 5-16.
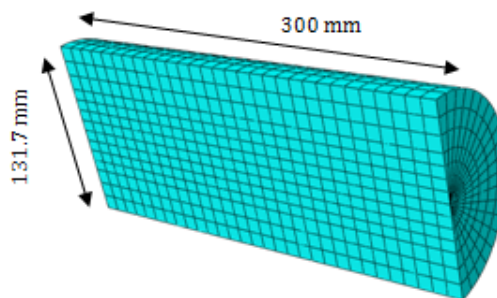

Figure 5-16: The geometry and the mesh of the grout core.

The grout core is meshed in solid elements C3D20 and the center of the core in C3D15 a wedge shaped element. The maximum element length is 10 mm. the mesh is illustrated in figure 5-16.

Boundary conditions

As for the steel tube, the cut faces of the grout core are modelled as symmetry planes.

The load is applied in 4 load steps. In the initial load step, LS 0, the contact pressure between grout and steel is established. The grout is given a temperature expansion coefficient of 1.2E-5 K^{-1} and the temperature in the grout core is raised 3 degrees. The load is applied diagonal to the support in load step1-3, LS 1-3. The load-support pair is turned up-side-down in LS 2 illustrated with the orange support-load pair in figure 5-17, while the red pair is active in LS1 and LS 3.

The load is applied as a concentrated force to a single node, and the support is modelled by restricting a node in displacements in the load direction.
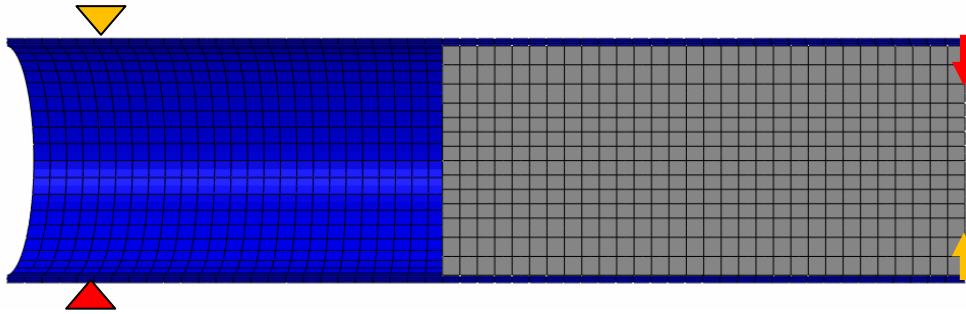
Figure 5-17: The load and support location in LS 1-3. The red pair is for LS 1 and LS 3, the orange pair is for LS 2.

The load is applied as a displacement and the load distribution to the time steps is shown in figure 5-18.
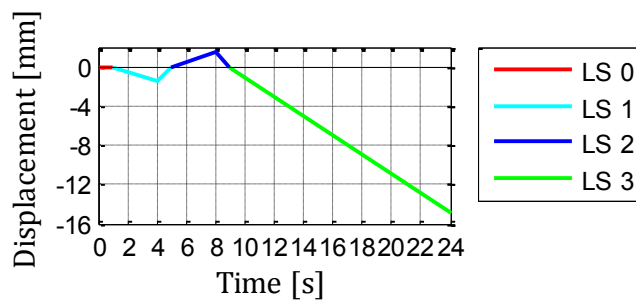

Figure 5-18: The load distribution as a function of the time.

Interaction of steel and grout

The interaction between steel and grout is modelled with the contact model based on Coulomb friction combined with the "hard contact" model in the normal direction. In order to activate the friction the contact pressure must be established. The approximation for the size of this pressure is based on the push-out test. The Coulomb friction defines slip when the equivalent shear exceeds the critical shear stress. The first slip in the push-out test is determined at 50 kN, see figure 5-19.
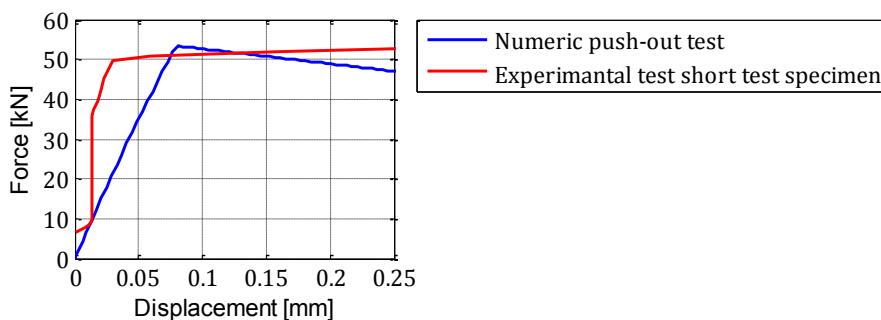

Figure 5-19: The results of the push-out tests. The experimental test is a part of the force-displacement relation for the short test specimen described in section 2.4

A numeric test is conducted in appendix E-5 is tuned on the temperature to fit the slip force. A temperature increase of 3 degrees leads to a slip force of 51 kN, when the coefficient of friction for steel on concrete is 0.6 and the temperature expansion coefficient is 1.2×10^{-5} degrees. The greased PCFT is modelled with $\mu_k = 0.036$ and is referred to as "without friction". The non-greased PCFT is modelled with $\mu_k = 0.6$.

5.3. Numerical Test Results

5.3.1. PCFT with HSC grout with friction

The results for the PCFT modelled with HSC grout and friction are shown in figure 5-20. There is degradation in the stiffness of the PCFT during the load steps caused by the damage in the grout core. Convergence problems caused the abortion of the analysis before completion of LS 3.
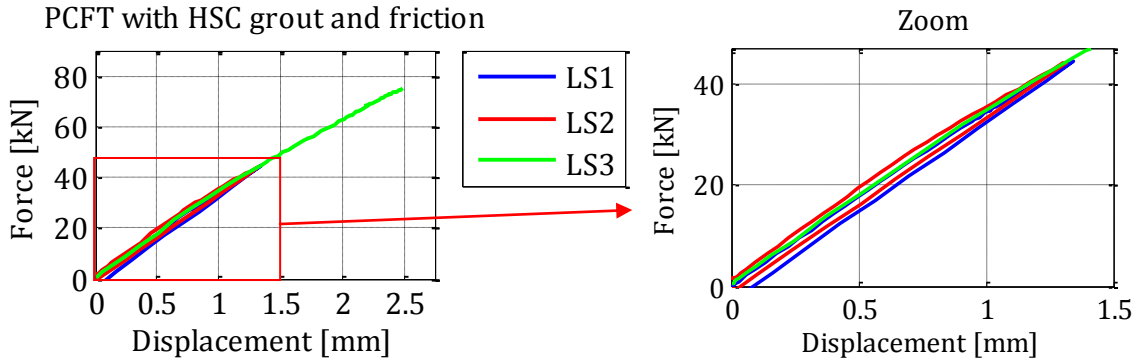

Figure 5-20: The force displacement relation for load step 1-3 for the PCFT with HSC grout and friction (left) and a zoom in the range of LS1 and LS2 (right),

The damage in the grout at the different load steps is shown in figure 5-21. The tensile damage at the end of LS 1 causes the degradation in the flexural stiffness of the global system. In LS2 the damage is smeared over the entire section, and further decrease of the flexural stiffness is seen, but the value is less than about 0.7 in most of the section. This causes a further degradation of the flexural stiffness in the third load step. The analysis is aborted due to convergence problems before the tensile damage reaches 1 in the entire section.
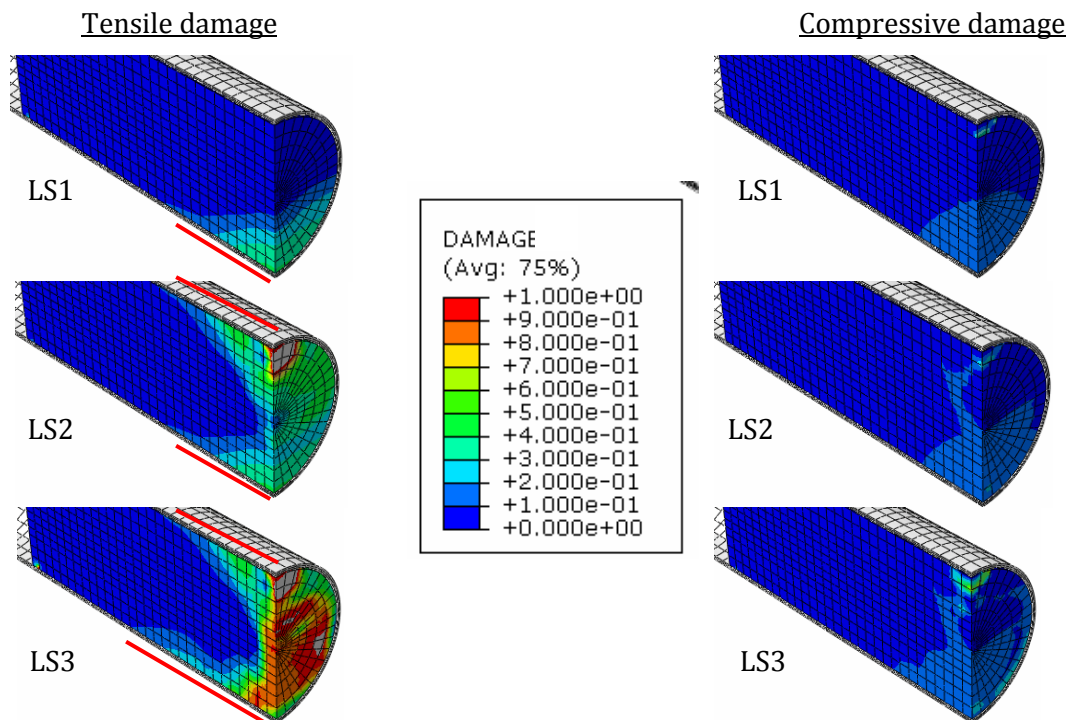

Figure 5-21: The tensile (left) and compressive (right) damage in the grout of the PCFT with HSC grout with friction at the end of load step 1 (top) to 3 (bottom). The red lines indicate the area the damage is smeared to.

The tensile damage is smeared to about ¼ the length of the grout core, L_{grout}, in LS 1. This length is increased to ½ of L_{grout} in LS 3. It is assessed to be a realistic distribution compared to the

The compressive damage in the PCFT has a limited extend and value is insignificant

5.3.2.   PCFT with HSC grout without friction

The results for the PCFT modelled with HSC grout and without friction are shown in figure 5-22 and the damage in the material at the end of the load steps are plotted in figure 5-23.
Like for the PCFT with friction, there is degradation in the stiffness of the PCFT during the load steps caused by the damage in the grout core. The peak load of the PCFT in LS3 is 78 kN and the analysis was terminated after 24 hours by the author due to very small iteration steps.
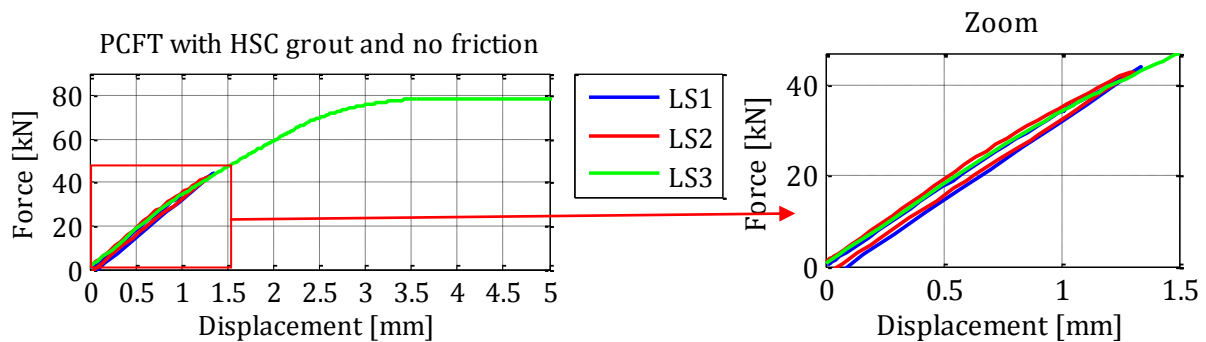

Figure 5-22: The force displacement relation for load step 1-3 for the PCFT with HSC grout and without friction (left) and a zoom in the range of LS1 and LS2 (right).

The tensile damage is smeared over about ⅕ of the grout length in LS 1 increasing to ¼ in LS3, where a new crack is initiated at about ¼ of the total grout length. The compressive damage develops where the load is applied and the value indicates that the grout is crushed.
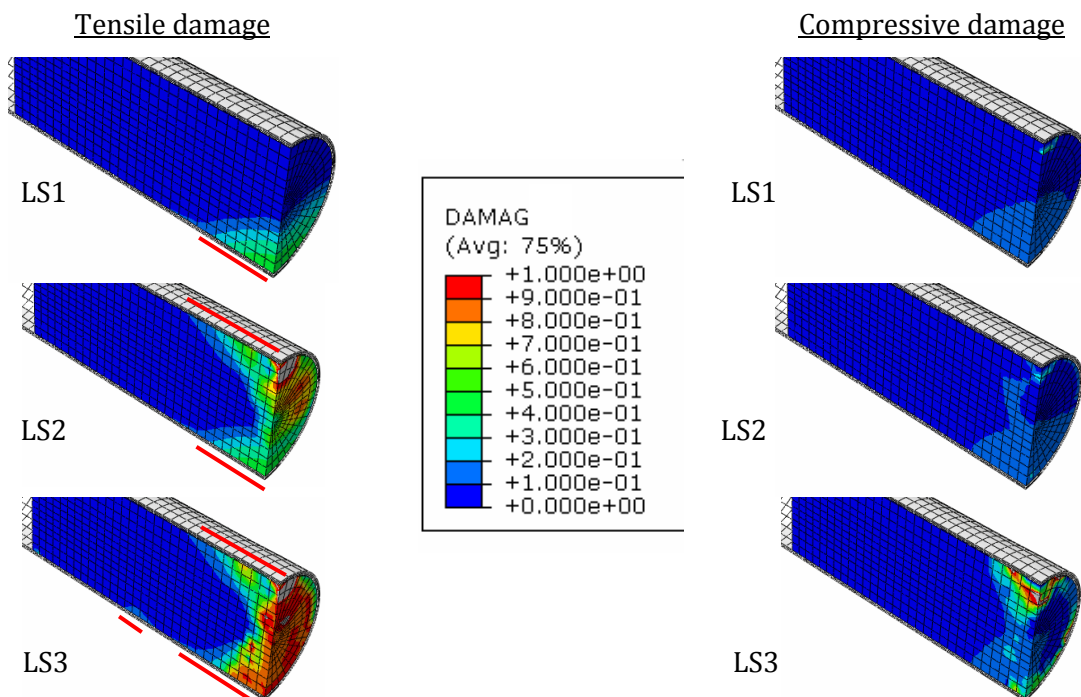

Figure 5-23: The tensile (left) and compressive (right) damage in the grout of the PCFT with HSC grout and no friction at the end of load step 1 (top) to 3 (bottom). The red lines indicate the area the damage is smeared to.

5.3.3.   PCFT with LSC grout with friction

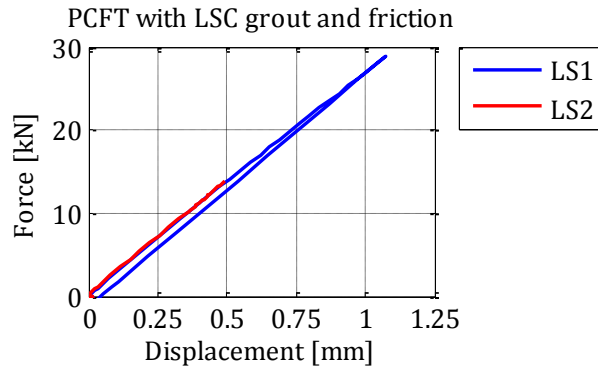There are no

PCFT with LSC grout and friction

Figure 5-24: The force displacement of LS1 and 2 for the PCFT with LSC grout and friction.

The tensile zone covers the entire grout section where the load is applied. The most damaged part is in the top of the section. The compressive damage develops in a zone

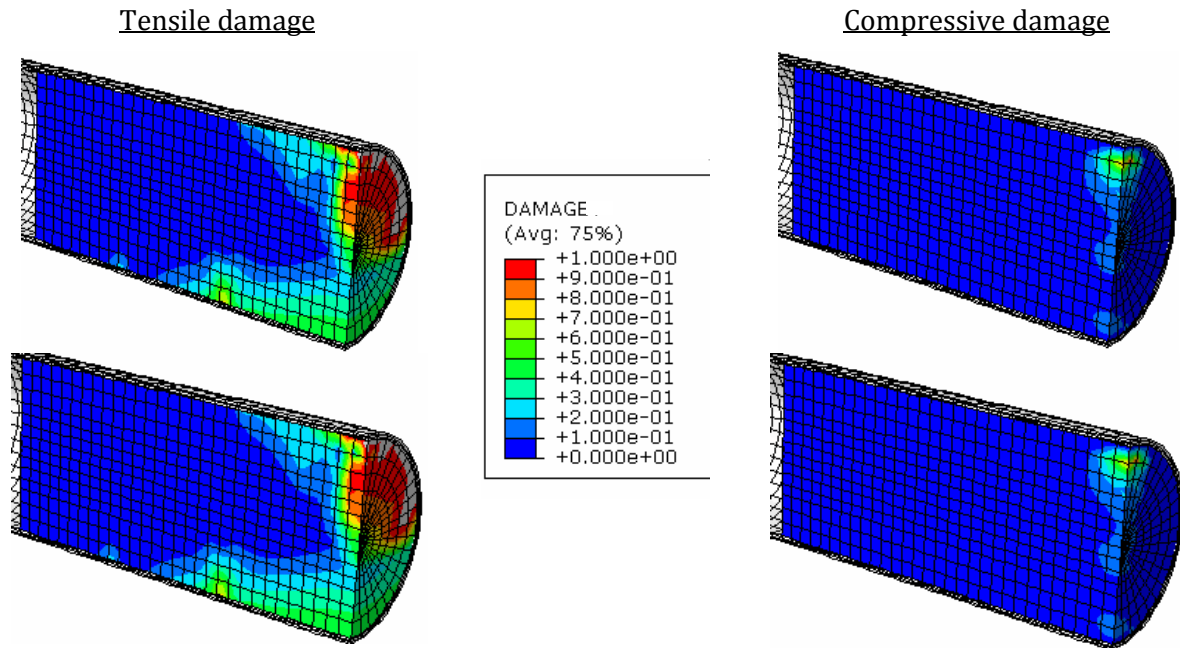Tensile damage   Compressive damage

Figure 5-25: The tensile (left) and compressive (right) damage distribution in the grout core of PCFT with LSC grout without friction at the end of load step 1 (top) and when the analysis is aborted in LS 2 (bottom).

5.3.4.   PCFT with LSC grout without friction

The analysis is aborted in load step 2 and LS3 is conducted without launching LS1 and LS2 first. There is almost no degradation in the flexural stiffness of the PCFT, see figure 5-26.
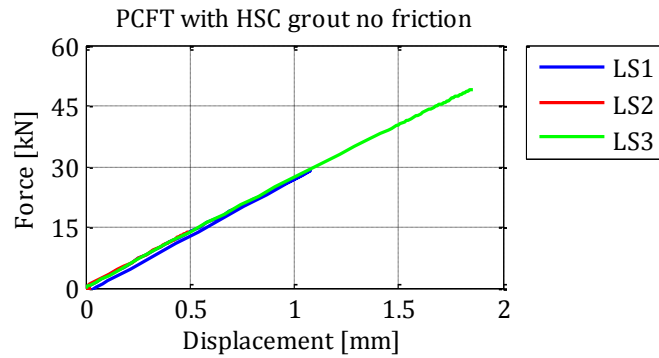
Figure 5-26: The load displacement for the PCFT with LSC grout and no friction in LS 1 and 2. The result in LS 3 has not been preloaded in LS 1 and 2.

The tensile damage is smeared over the entire grout section at the symmetry plane of the PCFT at the end of load step 1 as shown in figure 5-27. The compressive damage is developed in LS1.
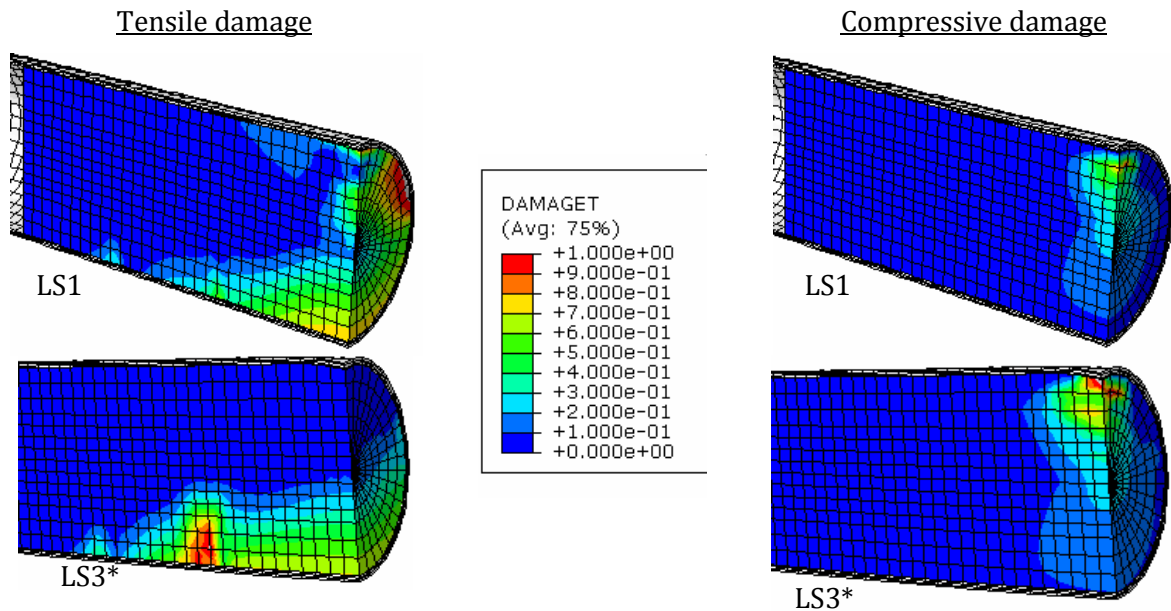

Figure 5-27: The tensile (left) and compressive (right) damage distribution in the grout core of PCFT with LSC grout without friction. The upper plots are at the end of load step 1, the lower plots are for LS3* equal to the extended LS1.

The load-Strain relations for the 4 numeric tests are plotted in appendix F.

References Chapter 5

5.1   Abaqus release notes (6-9.3), "Abaqus Analysis User's Manual" chapter 31.

5.2   Abaqus release notes (6.9-3), "Abaqus Theory manual" chapter 5.

5.3   Rabbat B.G. et al. (1985) "Friction Coefficient of Steel on Concrete or Grout" Journal of Structural Engineering, Vol. Ill, No. 3, March, 1985.   505-515.

6.   Comparison of Results of the PCFT

In this chapter the numeric and experimental test results of the PCFT's are compared on load-deflection relations, load-strain relations and the failure mechanisms.

6.1.   Load-Deflection
The results of the load-displacement relations in the numeric tests are compared to experimental tests.

6.1.1.   Influence of the Grout Strength and Contact Relations on the Flexural Stiffness
The grout strength influences the flexural stiffness of the PCFT as shown in figure 6-1, where the load-deflection of the numeric tests is plotted for each load step. The stiffness in the PCFT with HSC grout is increased 28 % at a deflection of 0.5 mm.

Initially the contact relations do not influence the flexural stiffness of the PCFT, but the non linear behaviour is introduced at a lower loading. This relation is only observed in PCFT with HSC grout due to the fact that the PCFT with LSC grout was aborted before reaching this load level.
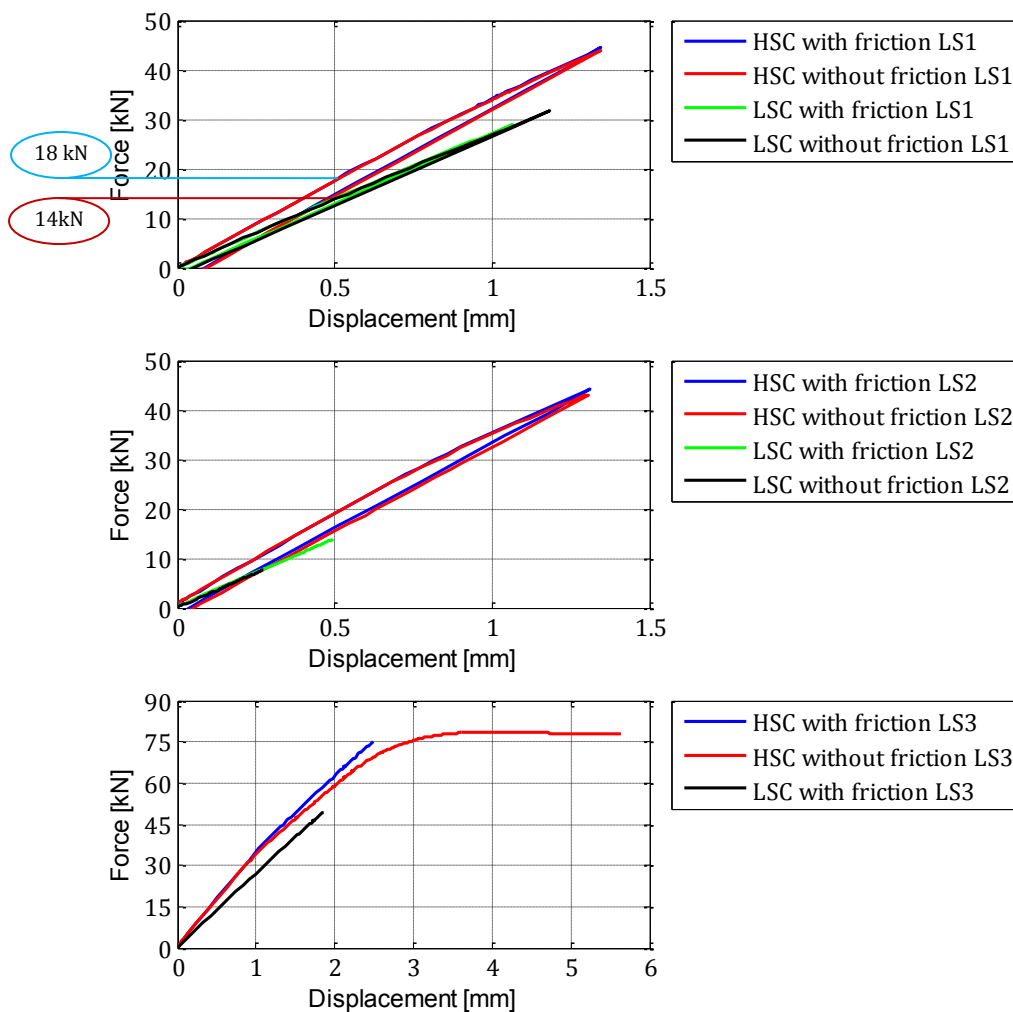

Figure 6-1: The load displacement relation of the numeric tests in LS 1-3 counted from the top.

Chapter 6

6.1.2. The Numeric Tests Compared to the Experimental Tests

The numeric tests are compared with the experimental tests load step for load step.

PCFT with HSC grout with friction

The analysis of the PCFT with HSC grout modelled with friction was aborted due to too small time increment in the iteration. The initial stiffness in the model in LS 1 equals the test result from LS 1a, see figure 6-2. The degradation in flexural stiffness in the experimental tests occurs more abruptly, which is due to the development of the cracks.
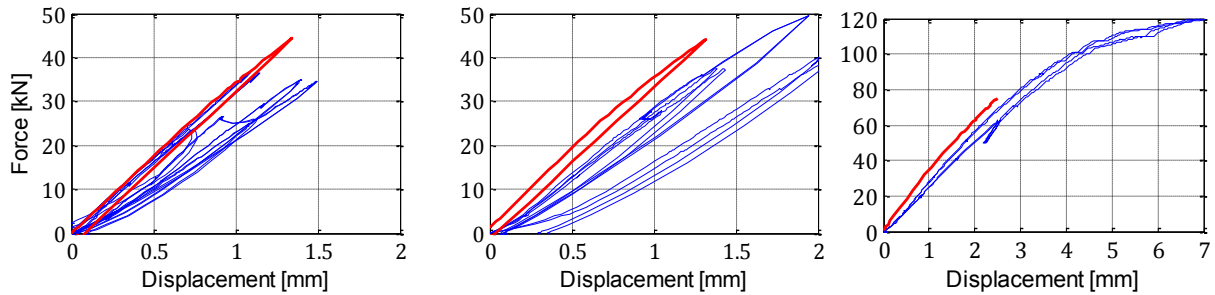

Figure 6-2: The numeric (red) and the experimental (blue) results for PCFT with HSC grout and friction in LS 1-3 counted from left. The blue curves are the force-displacement of CFT 1-3.

PCFT with HSC grout without friction

The result of the numeric model of the PCFT with HSC grout and without friction equals the comments of the one with friction. In load step 3 the numeric test approaches the experimental tests, see figure 6-3. The peak load of the numeric result is about 20 % lower than the experimental test. This indicates that errors introduced by the simplification of the numerical model of the steel tube are significant.
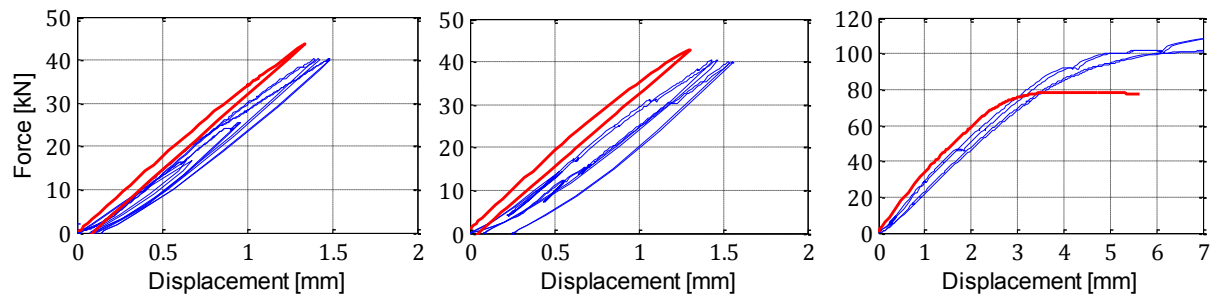

Figure 6-3: LS 1-3 for PCFT with LSC grout friction. The blue curves are the force-displacement of CFT 7-9.

PCFT with LSC grout with friction

The analysis of the PCFT with LSC grout modelled with friction was aborted due to too small time increment in the iteration. The stiffness in the model in LS 1 and LS 2 equals the test result, see figure 6-4.
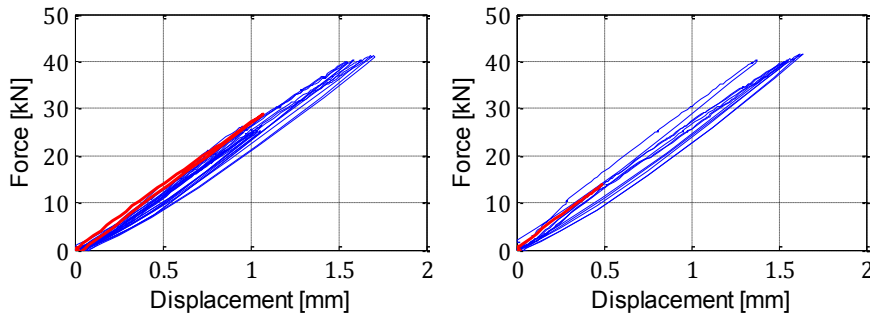
Figure 6-4: LS 1-2 for PCFT with LSC grout friction. The blue curves are the force-displacement of CFT 7-9.

PCFT with LSC grout friction without friction

The results for the PCFT with LSC grout without friction matches the experimental test results in LS 1, see figure 6-5. The flexural stiffness seems higher in LS 2, but the numeric test was aborted at a too low load level to draw a final conclusion. In LS 3 the numeric test was not exposed to LS 1 and 2 before activation LS3. This does not seem to influence the result significantly.
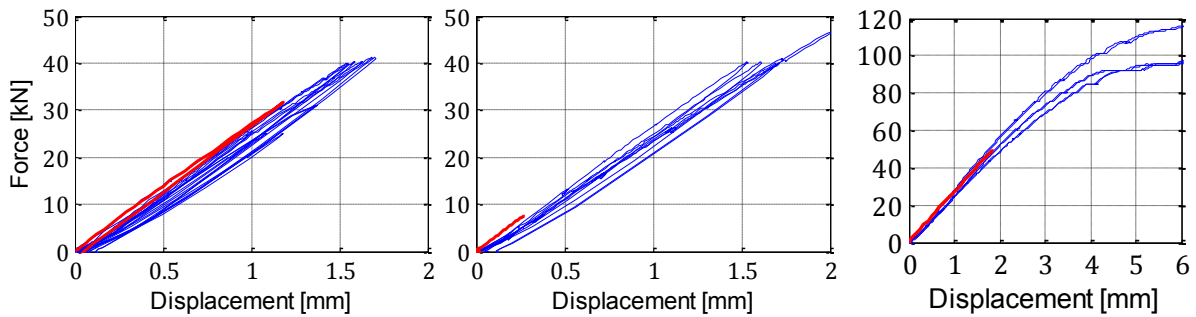

Figure 6-5: LS1-2 for PCFT with LSC grout without friction. The analysis in the lower plot was conducted without changing the load direction. The blue curves are the force-displacement of CFT 10-12.

6.2. Load -Strain Relations

In order to compare the strains in the steel tube in the numerical model to the strains found by experiments, the strains are measured in the same spots as in the experimental tests: 100 mm from where the load is applied at the outer surface of the steel tube. Data for the axial and hoop strains are gathered. The grout strength influences the strain level in the steel tube. More stress can be transferred to the HSC grout and therefore reduces the stress and strain level in the steel tube. The strains for the numerical tests are shown in figure 6-6.

The contact relations influence on the strain in the steel tube is initially insignificant. The strains in the steel tube are slightly increased in the PCFT with no friction compared to the PCFT with friction at a load level about 40-45 kN in LS 3. When the .
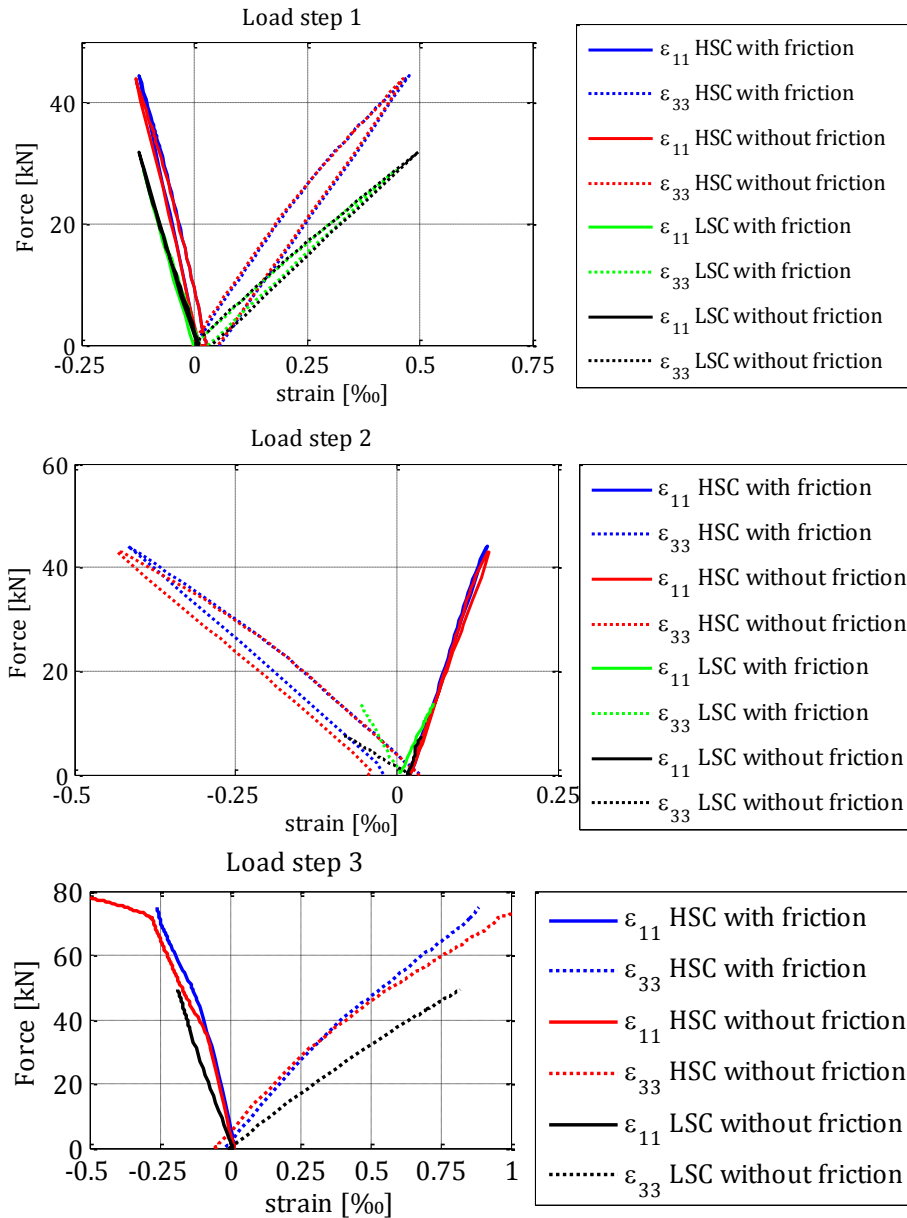
Figure 6-6: The load-strain relations for LS 1-3 counted from the top.

The numeric load-strain relations for the grouted PCFT shown in figure 6-7 fit well to the ones found by experimental tests. The abrupt increase in the hoop strain in load step 1 is delayed and smoothed in the numerical result of the HSC grout. The non linear increase
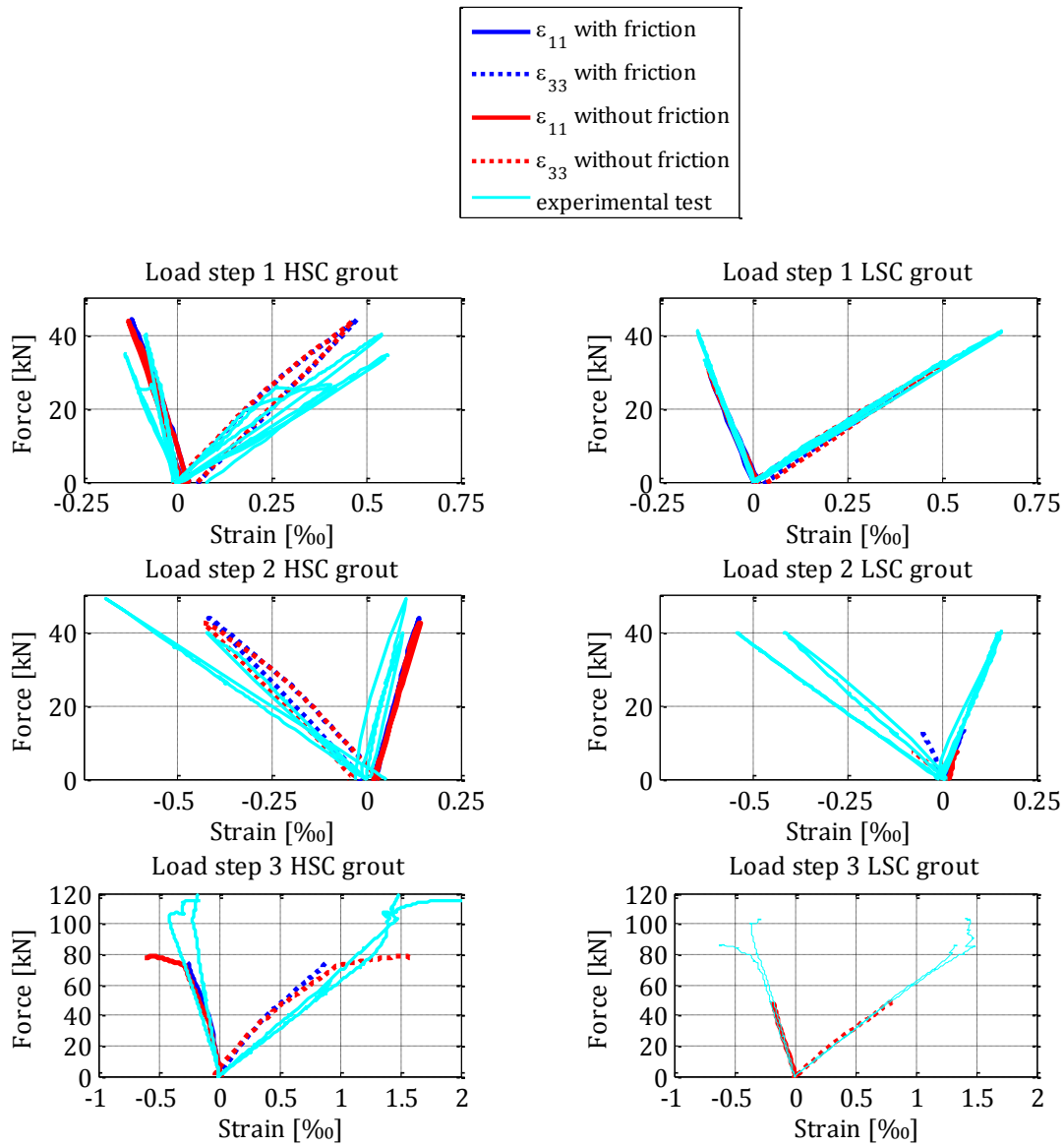
Figure 6-7: The force-strain relations for the numeric and experimantal tests for PCFT with HSC grout (left) and LSC grout (right) at LS 1-3 conuted from the top. The blue lines are for test specimens with friction, and the red lines for test specimens without friction. Dotted lines are hoop strains and unbroken lines are axial strains. The cyan curves are representative sampels of the experimental test results.

6.3. Failure Mechanism

Failure in the grout

The crack pattern is influenced by the contact relation between steel and grout. When the friction is removed, the crack width increases and the number is reduced, see figure 6-9. This matter is also found in the numeric tests, where the tensile damage is smeared over a larger area in the PCFT with friction. In the PCFT without friction, another crack is initiated half way between the grout end and the middle of the grout core (the symmetry plane) when the deflection becomes large, and the global system acts non-linear, see figure 6-8. This crack has not been developed in the numeric result of the PCFT with friction, probably because of the smaller deflection.

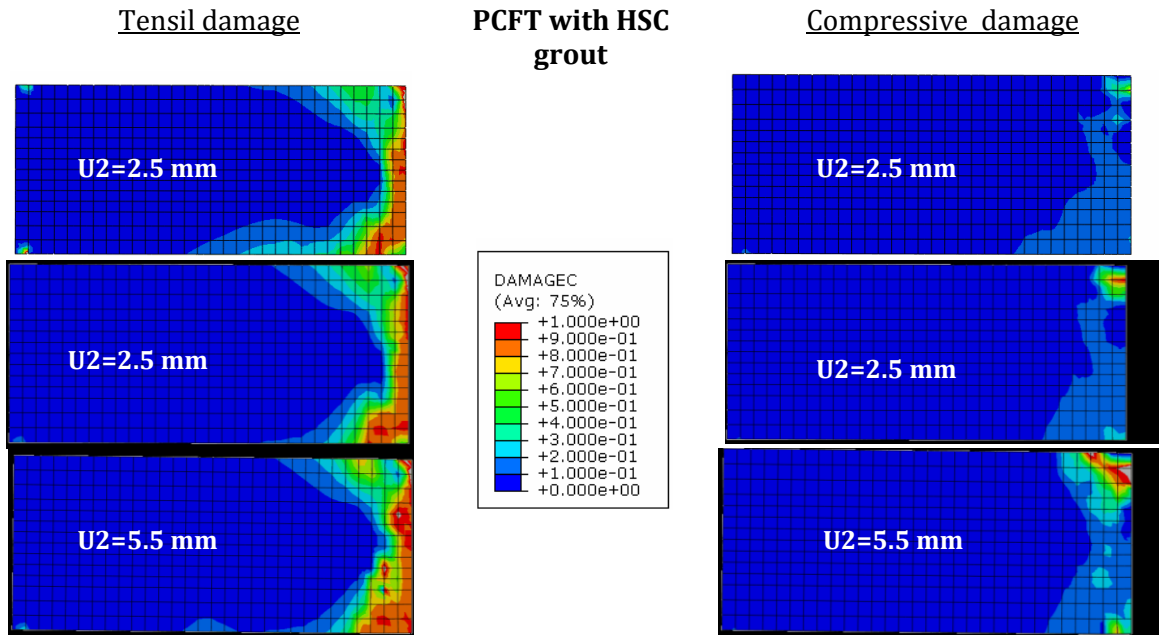| Tensil damage | PCFT with HSC grout | Compressive damage |

Figure 6-8: Comparison of the damage pattern in the grout for PCFT with HSC grout and with friction (top) and without friction (mid and bottom). The displacement in the PCFT is 2.5 mm in the plot in the top and middel and 5.5 mm in the plots at the bottom.

Figure 6-9: The crack pattern in the PCFT with HSC grout with (bottom) and without (top) friction determined by experiments.

The compressive damage does not differ significantly in the numeric test results for the PCFT's with HSC grout.

In the PCFT with LSC grout the compressive damage is significant, see figure 6-10. At the end of LS 1, the compressive damage zone is larger than the zone in the PCFT with HSC grout. The tensile damage, shown in figure 6-11 is smeared over a larger part of the grout length than for the HSC grout, because of the significant lower tensile strength. Furthermore the definition of the damage evolution differs.
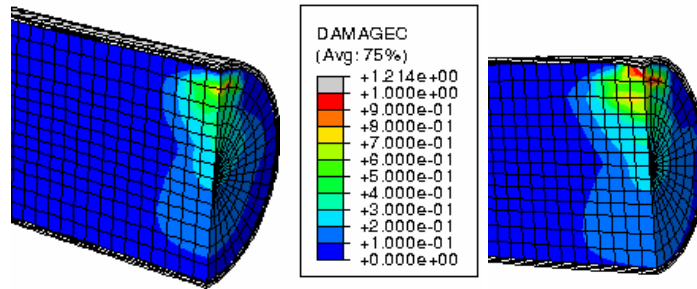
Figure 6-10: The compressive damage in the PCFT with LSC grout at the end of LS1 equal to a load level of 30 kN (left) and for a loading of 50 kN (right).
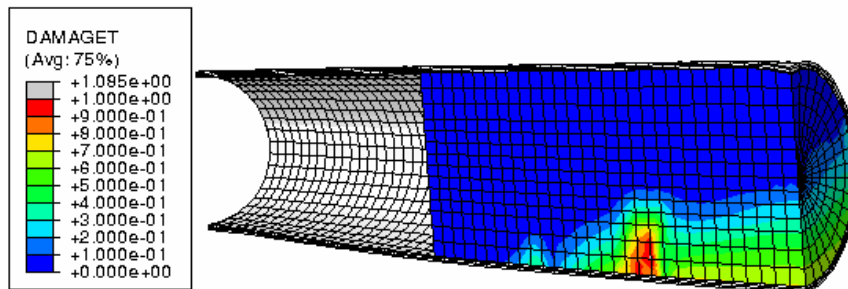
Figure 6-11: The tensile damage in the PCFT with LSC grout and no friction.

The failure mode in the experimental tests shows an inward buckling in the steel tube where the load has been applied, see figure 6-12. This failure in the steel tube is combined with the grout crushing as found in the numeric model.

Figure 6-12: The failure in one of the PCFTs with LSC grout. The red marking illustrates the area with crushing in the grout.

The crack width of the LSC grout is very small. There are few or no visible cracks in the grout core, see figure 6-13. Visible cracks are in the zone with crushing.

Figure 6-13: the grout cores of two PCFT's with LSC grout one non-greased (top) and one greased (bottom).

Failure in the steel

The steel tube of the PCFT without friction starts buckling nearby where the load is applied. The buckling is outward buckling and is initiated in after the entire steel section is yielding, see figure 6-14.
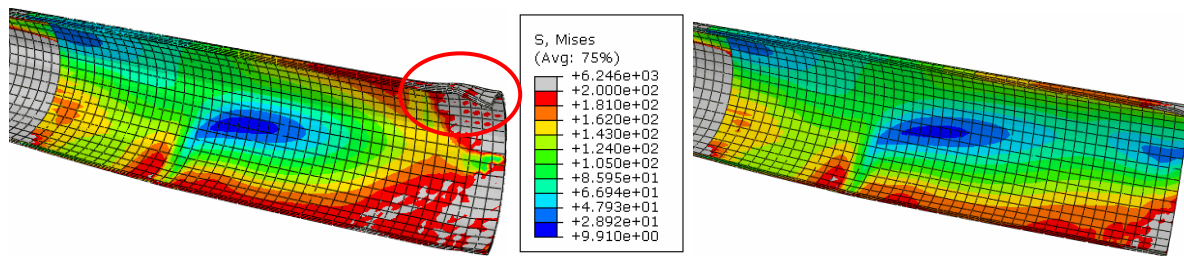
Figure 6-14: The steel tube of the PCFT with HSC grout without friction. The deformation is scaled by a factor 10. The red marking indicated the area with buckling. The deflection is 5.5 mm to the left and 2.5 mm to the right. The grey areas indicate yielding in the steel.7

This behaviour is also observed in the experimental tests, when the deflection is very high. The outward buckling only appears in the PCFT with HSC grout, because of the crushing in the LSC grout.

Figure 6-15: The outward buckling in steel tube with HSC grout (left) and the inward buckling in the steel tube with LSC grout. The inward buckling is located where the load is applied.

7. Discussion

7.1. Experimental Setup

The Grout

The grout mixing procedure and curing conditions may have reduced the material strength compared to the material data from the manufacturer based on impartial tests. This has no influence on this research, because the numeric model is based on own material test results. The HSC grout was mixed in 5 portions and in 4 of the 6 tubes the grout comes from two mixtures. Differences in the grout strength for the individual mixtures will occur, but it is assessed not to influence the tests result significant. The LSC grout was mixed in two times for three tubes each.

The differences in the grout length of up to 25 mm affect the results. The influence is difficult to determine because the grout strength will vary.

Contact Relations

The greasing of the steel tubes was done by hand. This results an uneven distribution of the grease layer and there may occur areas with no grease. Such areas will affect the bonding significantly depending on the size of the areas. The visual inspection of the inside of the greased steel tube

Equipment

Data was logged with 1 Hz due to the amount of data and the load rate. It is assessed that no important data has been lost due to the logging frequency.

The accuracy of the displacement transducers is 1/100 mm in the range from 1-20 mm, and the result beyond 20 mm are not accurate. The load cell was calibrated with two other load cells. The accuracy of the load cell in 1 N is sufficient. Both is assessed not to have influence of the of the test results.

The load procedure

The unloading at 25 kN in load step 1 was unnecessary. The cracking was observed at this load, but the loading could as well have been continuously to 40 kN. The turning of the PCFT in order the make sure that the entire grout section was cracked complicated the mounting of measuring equipment.

The test setup

The original problem of a leg on a platform is converted to a 3-point bending is an approximation, because of the loading. The leg on a platform has a fixed end where the load is applied in the experimental tests. The area through which the fixed end will transfer the load to the foundation is larger than the area where the load is applied. The stress concentration in the fixed end will be lesser than the one in the experimental tests. Nevertheless the test setup is assessed to be a fair way to study the problem and the use of the load plate reduces this matter in some degree.

Discussion

7.2. Numeric Setup

The numeric model for the PCFT is setup taking the elements number in account. Two nonlinear material models combined with a friction model complicates the model and the CPU time is easily increased. In order to reduce the node numbers, the grout core is modelled with a rather coarse mesh and there has not been carried out a study of sensitivity on this matter.

7.2.1. The Material Model for the Grout

To overcome convergence problems when the grout cracks the viscosity is needed. The sensitivity study showed that this parameter influence the global result because more energy can be obtain in the elements. The damage development is allowed to run in one element row no matter of the size of this element and the only way to control the crack band width is by the use of the viscosity parameter. The plastic damage model used for modelling the grout is mesh-dependant.

The tensile damage and softening model are based on the fracture energy and the tensile strength. The numeric damage development matches the cracking in the PCFT roughly and it is assessed that the accuracy of the models are sufficient. The compressive hardening is modelled with different variables. The numeric damage picture results in a larger compressive damage zone in the LSC grouted PCFTs, which reflect the crushing zone in the experimental tests adequately.

7.2.2. The Friction Model

The friction model is chosen as Coulomb friction. The calibration of the model to the push out test does not fit very well. The modelled slip occurs more abrupt than in the push out test. When the grout core is loaded axially in the push out test, it is assessed that the adhesion will contribute to the shear transfer and the mechanism should be modelled e.g. by the use of cohesion elements. In the case of the PCFT the effect from the adhesion is expected to be ignorable and the friction model is assumed to fit this situation better.

In order to establish the initial bond between grout and steel the grout core is given a temperature expansion which introduces some initial stresses in the system. The size of the hoop stresses at the end of the heating is 6 MPa, which is illustrated in figure 7-1
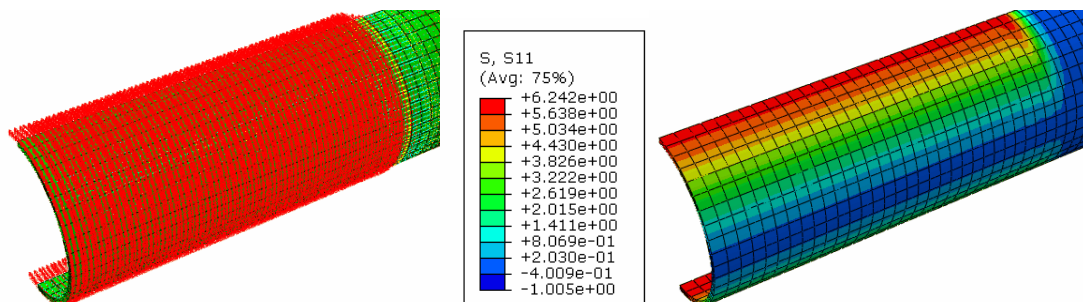

Figure 7-1: The hoop stresses in the numeric model caused by heating the grout.

7.2.3. The Simplified Model

The simplified model converts the cuff to an increased modulus of elasticity in part of the steel tube covered by the cuff. This assumption is assessed to be fair for the increased moment of inertia, but not for the contact relations between steel tube and cuff.

The simplification of the model in order to optimize the solution was assumed to be fair in the linear range of the PCFT due to the comparison of the model of the empty steel tube shown in figure 7-2.
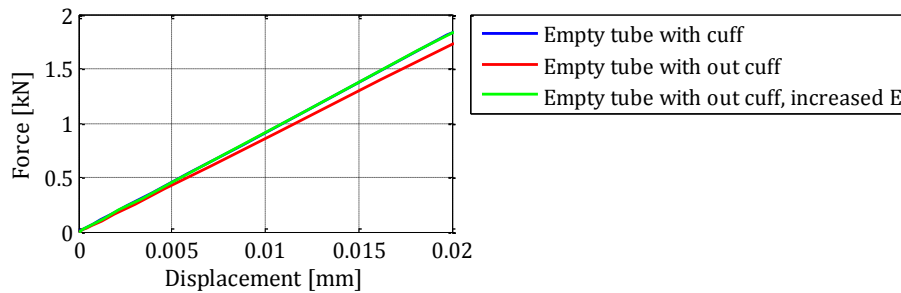

Figure 7-2: The force-displacement relations for numeric models with and without the reinforcement cuff.

This approximation is supported by the good agreement in the initial part of the numeric and experimental tests.

The simplified model is tuned on the yield stress in order to fit the experimental force displacement of the empty steel tube. The yield stress used is 200 MPa compared to the 328 MPa determined by Force Technology and the curve was fitted to the post peak range of the curve and not the peak load, see figure 7-3.
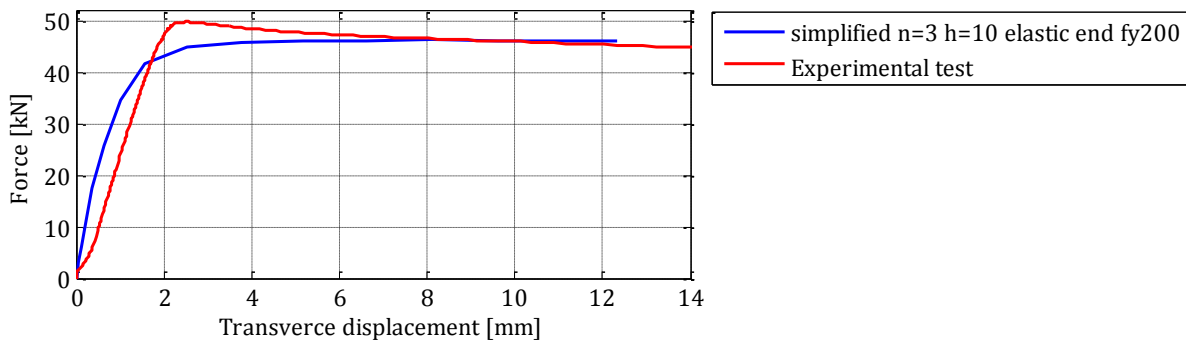

Figure 7-3: The fitting of the simplified model to the experimental result of the empty steel tube.

It is assessed, that basing the model of the PCFT on a model of the steel tube fitted to the experimental result of the empty steel tube is a reasonable approach.

The numeric model of the PCFT with the simplified does reflect the non linear behavior but underestimates the peak load about 20 %. Increasing the yield stress will make the model fit to the results, but this approach is unusable in a design matter. If the result in the nonlinear range is needed the simplified model is not sufficient.

7.3. The Behaviour of the PCFT

7.3.1. Flexural Stiffness

The flexural stiffness of the PCFTs with HSC grout in the numeric model is initially 28 % higher than for the PCFTs with LSC grout at a deflection of 0.5 mm. This is expected due to the fact that the modulus of elasticity, E_c, of the HSC grout is 4.8 times higher than E_c for the LSC grout, and the initial.
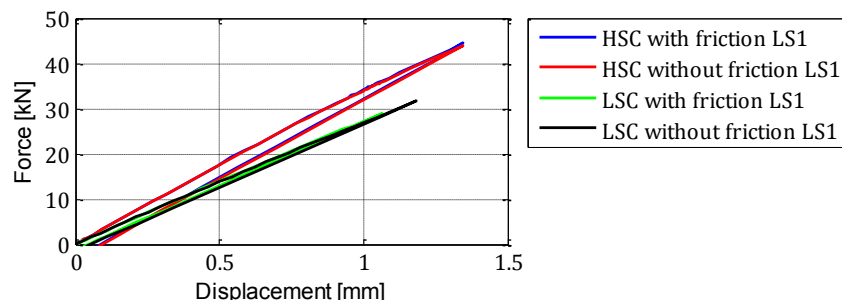

Figure 7-4: The flexural stiffness is visualized as the slope of the load deflection curves. The PCFTs with HSC grout have an increased flexural stiffness compared to the LSC grouted PCFTs.

This increase is in general also governed by the grout length with the extremes as the empty tube and the CFT. Rewriting eq. 1-1 the increase in flexural stiffness of a CFT with an un-cracked grout section is 62 % according to eq. 7-1

Eq. 7-1

$$1 - \frac{\left(E_{steel}I_{steel} + E_{grout;HSC}I_{grout}\right)}{\left(E_{steel}I_{steel} + E_{grout;LSC}I_{grout}\right)} = 1 - \frac{\left\{8,25E11\ Nmm^2 + 51700\ MPa \cdot \frac{\pi}{64} \cdot (131,7\ mm)^4\right\}}{\left\{8,25E11\ Nmm^2 + 10700\ MPa \cdot \frac{\pi}{64} \cdot (131,7\ mm)^4\right\}} = 0,62$$

For a linear development between the extremes (empty tube and CFT) the increased stiffness should be 37 % for a grout length of 3/5 of the steel tube. An increase of 28 %, is assessed to be fair for the model.

The numeric result fits to the experimental results, see figure 7-5. The increase in flexural stiffness in the experimental tests is reduced to the flexural stiffness of the LSC grouted PCFT at a load level of 25-40 kN and is abrupt.
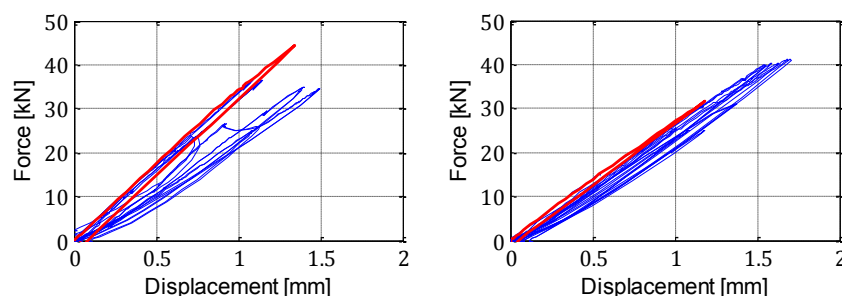

Figure 7-5: The load-deflection relations for a PCFT with HSC grout (left) and with LSC grout (right). The red curve is the numeric result; the blue curves are the experimental results.

The similar adaption in the numeric model is smoothed and is not obvious in the numeric results, see figure 7-6, where the damage in the grout develops as a stable process. This can be

explained by the formulation of the tensile damage development in the numeric model and in how the load is applied. In the experimental test, the loading is force controlled and in the numeric model it is displacement controlled.
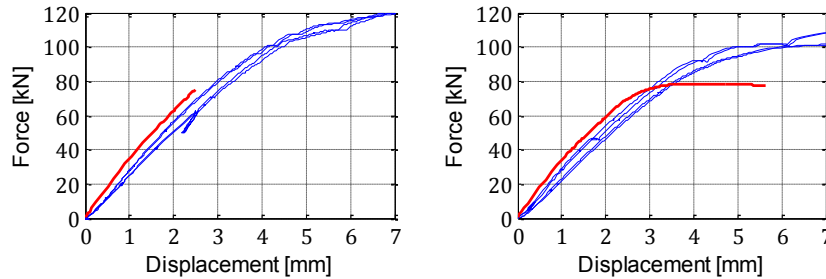

Figure 7-6: The load-deflection relations for a PCFT with HSC grout with (left) and without (right) friction. The red curve is the numeric result; the blue curves are the experimental results.

7.3.2. Peak Load

Only the peak load in the PCFT with The peak load is influenced by both the grout strength and the contact relations. The grout strength increases as expected the peak load and decreasing bond strength decreases the peak load. This is solely based on the experimental results because only the numeric analysis of the HSC grouted PCFT without friction was not aborted. The peak load of this is 21-29 % lower than the experimental test results.

The linear range of the empty steel tube is significantly extended no matter the grout strength or contact relations as shown in figure 7-7. This is assessed primarily to be caused by the change delayed buckling in the steel. Either the grout is crushed and the steel buckle inward where the load is applied or the zone where the grout is crushed is minor and a plastic hinge is developed in the steel. The outward buckling becomes visible at a deflection of more than 20 mm.

The increase in the linear range using a HSC grout is 81- 112 % and 57 -79% for the LSC grout depending on the contact relations.

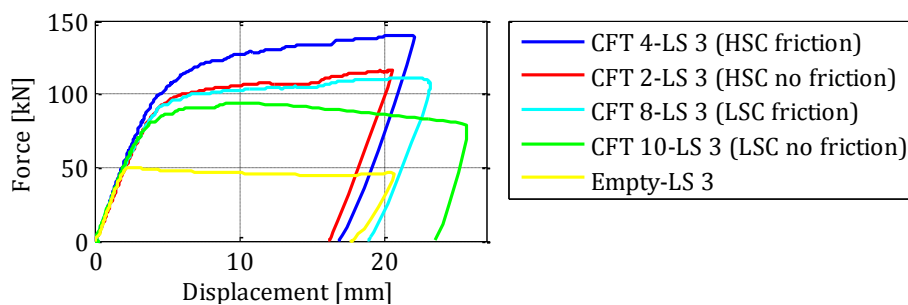**Figure 7-7: The load deflection of the PCFTs determined by experiments.**

In the case of a PCFT used as a leg on a platform the boundary conditions differs from the experimental tests. The stress concentration from the load in the experimental test will not be present and the stresses at the fixed end will be transferred through almost the entire section. The inward buckling is in this case will be delayed or disappear.

Discussion

The contact relations seem to affect the grout of high strength most. In the case of the low strength grout the difference in the peak load of the PCFT is minor than for the high strength grout. It is assessed that it is due to the different crack pattern in the grout.

The grout strength and the contact relations also affect peak load and the behavior in the post yield area. In general the HSC grout results in higher peak loads and the peak load in the PCFT with friction is increased compared to the ones without friction.

8.   Conclusion

The numeric model has been developed on the basis of experimental tests of the materials. The modulus of elasticity and Poisson's ratio for the high strength grout and the compressive strength of the high strength as well as the low strength grout are determined. The tensile strength is found indirectly through the splitting tensile strength and all parameters are used to setup the numeric material model based on the plastic damage model. The material model can visualize the areas where the grout is cracked or crushed, and the calibration of the model results in a fair pattern of the cracking and crushing in the experimental tests. The sensitivity study of the material model shows that the model is mesh-dependent when the viscoplastic regularization is activated.

The model of the partially concrete filled steel tube is based on a model of the empty steel tube. This is modelled by use of symmetry as a quarter of the test specimen. In order to make the model more efficient the numeric model is further simplified by converting the reinforcement cuff to en increased modulus of elasticity in the steel tube. The model is fitted to the experimental test results by reducing the yield stress in the numeric model to 200 MPa.

The flexural stiffness of the model of the partially concrete filled steel tube is initially equal to the test results and the flexural stiffness of the partially concrete filled steel tube with high strength grout is about 28 % higher than the one for the low strength grout. The flexural stiffness is degraded when the grout is damages, but the development in the damage in the numeric model is steadily contrary to the experimental tests, and the decrease in flexural stiffness develops slower in the numeric model.

The peak load determined by the numeric model is reduced 21-29 % compared to the experimental tests caused by the reduction in yield strength of the steel in the simplified model.

The simplified numeric model is assessed to be fair in the linear elastic range of the partially concrete filled steel tubes. The model must be re-tuned on the yield strength to predict the behaviour in the plastic ran of the partially concrete filled steel tubes.

The mechanical behaviour of the partially concrete filled steel tubes is influenced by the strength of the grout and the contact properties. Initially the flexural stiffness in increased in the partially concrete filled steel tubes with high strength grout. The cracking process of the grout is unstable and the loss in flexural stiffness develops abrupt. When the grout is cracked the flexural stiffness equals the empty steel tube.

The presence of grout extends the elastic behaviour of the empty steel tube by 57 – 112 % depending on the grout strength.   The high strength grout results in an increase of 81-112 % while the low strength grout prolongs the elastic range with 57-79 % depending on the contact relations.

Conclusion

The grout strength and the contact relations also influence the peak load and the post yield behaviour. The higher grout strength the higher peak load and the better bond the higher peak load. The peak loaf is increased with 176 % in the partially concrete filled steel tubes with high strength grout compared to the empty steel tube. The peak load in the partially concrete filled steel tubes with low strength grout and no friction is increased 84 %

The failure mechanism in the partially concrete filled steel tubes is affected by the grout strength and the contact relations. The crack width in the grout of the partially concrete filled steel tubes with a poor bonding is increased and the number of cracks reduced compared to the ones with a good contact between steel and grout.

The low strength grout cannot resist the compressive stresses from the concentrated force applied transversely to the steel tube and the crushing in the grout is combined with a inward deformation in the steel tube. In the partially concrete filled steel tubes with high strength the steel tube buckles outward next to the area where the load is applied.